

Medical University of South Carolina

MEDICA

MUSC Theses and Dissertations

2019

Glial Dysfunction in Mouse Auditory Nerve Results in Dysmyelination and Nodal Abnormalities Leading to Loss in Hearing Function

Clarisse Hipolito Panganiban
Medical University of South Carolina

Follow this and additional works at: <https://medica-musc.researchcommons.org/theses>

Recommended Citation

Panganiban, Clarisse Hipolito, "Glial Dysfunction in Mouse Auditory Nerve Results in Dysmyelination and Nodal Abnormalities Leading to Loss in Hearing Function" (2019). *MUSC Theses and Dissertations*. 592. <https://medica-musc.researchcommons.org/theses/592>

This Dissertation is brought to you for free and open access by MEDICA. It has been accepted for inclusion in MUSC Theses and Dissertations by an authorized administrator of MEDICA. For more information, please contact medica@musc.edu.

Glial dysfunction in mouse auditory nerve results in dysmyelination and nodal abnormalities leading to loss in hearing function

by

Clarisse Hipolito Panganiban

A dissertation submitted to the faculty of the Medical University of South Carolina in partial fulfillment of the requirement for the degree of Doctor of Philosophy in the College of Graduate Studies.

Department of Pathology and Laboratory Medicine

2019

Approved by:

Chairman, Advisory Committee

Dr. Hainan Lang

Dr. Edward L. Krug

Dr. Kelly C. Harris

Dr. Judy R. Dubno

Dr. Bärbel Rohrer

Dr. Bradley A. Schulte

DEDICATION

For my parents, God, and BPM.

TABLE OF CONTENTS

Dissertation Title.....	Page 1
Dedication.....	Page 2
Table of Contents.....	Page 3-6
List of Abbreviations.....	Page 7-8
List of Tables and Figures.....	Page 9-10
Clarification of commonly used terms.....	Page 11
Abstract.....	Page 12

Chapters

1. Introduction.....	Page 13
1.1. The neural aspects of the auditory nerve	
1.1.1. The spiral ganglion neurons	
1.1.2. Tonotopic arrangement and frequency- and intensity-based activity of the SGNs	
1.1.3. Auditory brainstem response and neuropathy: Making sense of stimulus-based auditory nerve activity	
1.2. Glial cells and myelination	
1.2.1 The auditory glial cells	
1.2.2 Myelination in the peripheral nervous system during development	
1.3. The nodes of Ranvier and flanking nodal domains	
1.3.1 The nodes of Ranvier of the PNS	
1.3.2 The excitable nodal domains of the auditory nerve	
1.4 The Quaking RNA binding proteins as regulators of myelination and paranodal maintenance	
1.5 Sensorineural hearing loss and dysmyelination	
1.5.1 Sensorineural hearing loss	
1.5.2 Dymyelination and hearing loss	
1.6 Purpose of this study	
2. General methods.....	Page 34
2.1. Animals	
2.1.1. Vivarium and parameters for use	
2.1.2. Normal hearing and noise studies	
2.1.3. Mutation models	
2.1.3.1. Diminuendo	

2.1.3.2.	Quaking	
2.1.3.3.	Genotyping	
2.2.	Physiological studies	
2.2.1.	Auditory brainstem response	
2.2.2.	Continuous ABR method to calculate Phase Locking Value (Intertrial Coherence) and other metrics of wave I	
2.3.	Transcriptomic analyses	
2.3.1.	Cochlear nerve tissue collection and total RNA isolation	
2.3.2.	Microarray hybridization	
2.3.3.	RNA sequencing	
2.3.4.	Quantitative PCR	
2.4.	Histological analyses	
2.4.1.	Immunostaining and confocal imaging	
2.4.2.	Node length measurements	
2.4.3.	Transmission electron microscopy	
2.5.	Statistical analyses	
3.	Myelination and nodal assembly in normal auditory nerve development.....	Page 50
3.1.	Introduction	
3.2.	Specific methods	
3.2.1.	Animals used	
3.2.2.	Developmental RNA-seq analyses of node-related genes	
3.3.	Results	
3.3.1.	Expression profiles of genes composing nodal structural domains exhibit temporal clustering and the onset of node formation in the mouse auditory nerve	
3.3.2.	Hearing onset and maturation of AN function and their relation to SGN subtype differentiation	
3.3.3.	Assembly of nodal and paranodal proteins comprising the axonal and ganglion nodes	
3.3.4.	Node lengths are associated with amplitude growth and decreasing latency	
3.3.5.	Ultrastructural assembly of axonal nodes and flanking paranodes	
3.3.6.	Ultrastructural assembly of ganglion nodes and satellite cell paranodes	
3.3.7.	Completion of heminodal clustering under inner hair cells is temporally dependent	
3.3.8.	Disorganization of the heminodes in a model of profound hearing loss	
3.4.	Discussion	
4.	Glial dysfunction after noise injury leads to dysmyelination and loss of hearing function.....	Page 84

- 4.1. Introduction
 - 4.2. Specific methods
 - 4.2.1. Animals used
 - 4.2.2. Noise exposure
 - 4.2.3. Physiological procedures
 - 4.2.4. Microarray analyses
 - 4.2.5. RT-qPCR
 - 4.2.6. G ratio measurements
 - 4.3. Results
 - 4.3.1. Noise-induced functional declines in the young-adult CBA/CaJ mouse AN
 - 4.3.2. Noise-induced demyelination, disruption of paranodal axo-glia junctions, and recruitment of macrophages
 - 4.3.3. Expression patterns of QKI variants and potential targets of QKI in response to noise injury
 - 4.3.4. Expression patterns of QKI isoforms in postnatal and adult ANs
 - 4.3.5. Reduction of QKI protein expression in AN glial cells of adult *QKI^{FL/FL};PLP^{CreERT}* mice
 - 4.3.6. Diminished QKI expression results in demyelination and disruption of paranodal structures in the adult AN
 - 4.4. Discussion
5. Glial dysfunction in auditory nerve development leads to hypomyelination or demyelination, and loss of hearing function.....Page 117
- 5.1. Introduction
 - 5.2. Specific methods
 - 5.2.1. Animals used
 - 5.2.2. RNA-seq analyses of expression of glia-related genes and putative QKI target genes in development
 - 5.3. Results
 - 5.3.1. Transcriptomic analyses of putative QKI targets pre-peak and during peak myelination: Potential glia- and downstream QKI-target related genes
 - 5.3.2. Abrogation of QKI RBPs in myelinating glial cells after knockout of quaking gene
 - 5.3.3. Developmental-stage dependent QKI-KO induces hypomyelination or demyelination of auditory nerve fibers at P14
 - 5.3.4. *qkl* KO at P5 leads to chronic hypomyelination and morphologically abnormal SCs
 - 5.3.5. Eventual dysmyelination of type I SGN fibers and somata in P21 after *qkl* KO at P7
 - 5.3.6. MBP expression is chronically depleted and Iba⁺ cells are present in great numbers adjacent to dysmyelinated somata in either *qkl* KO group

- 5.3.7. *qkl* KO caused abrogated Cntn1 expression and disruption of paranodal structures
 - 5.3.8. *qkl* KO-induced hypomyelination leads to loss of AN function
 - 5.3.9. Eventual dysmyelination due to *qkl* KO at peak myelination may lead to functional declines in later development
- 5.4. Discussion

6. Global discussion.....	Page 159
7. Appendix.....	Page 162
A-1 ABR measurements after hearing onset	
A-2 KO of <i>qkl</i> induced a chronic decrease of the Sox2 marker of plasticity in SGCs and increase of number of Iba1+ macrophages.	
8. References.....	Page 164

LIST OF ABBREVIATIONS

4',6-diamidino-2-phenylindole – DAPI
4-hydroxytamoxifen – TAM
Action potential – AP
Analysis of variance – ANOVA
Auditory brainstem response – ABR
Auditory nerve – AN
Base pair – bp
Cellular adhesion molecule – CAM
Characteristic frequency – CF
Charcot-Marie-Tooth – CMT
Compound action potential – CAP
cycle threshold – CT
Database for Annotation, Visualization, and Integrated Discovery – DAVID
Day – D
Decibel – dB
Deoxyribonucleic acid – DNA
Differentially expressed – DE
Diminuendo – Dmdo
Embryonic – E
Ethylenediamine tetraacetic acid – EDTA
False discovery rate – FDR
Flox – Fl
Fold change – fc
Guillain-Barre Syndrome – GBS
Habenula – Hab
Hair cells – HC
Heterozygous flox – Fl/-
Hidden hearing loss – HHL
Homozygous diminuendo mouse – Dmdo/Dmdo
Homozygous flox – Fl/Fl
Immediately – Im
Inner hair cell – IHC
K homology – KH
Knockout – KO
Medical University of South Carolina – MUSC
Modiolus – Mod
N-ethyl-N-nitrosourea – ENU
Noise-induced hearing loss – NIHL
Osseous spiral lamina – OSL
Outer hair cell – OHC

Outer hair cells – OHC
Paraformaldehyde – PFA
Peripheral nervous system – PNS
Permanent threshold shift – PTS
Phase Locking Value – PLV
Phosphate buffered saline – PBS
Polymerase chain reaction – PCR
Postnatal day – P
Propidium iodide – PI
Quaking control mice – QKI-Ctrl
Quaking domain – QUA
Quaking gene – qkl
Quaking knockout mice – QKI-KO
Quaking protein – QKI
Quaking recognition element – QRE
Quantitative PCR – qPCR
Reverse transcription qPCR – RT-qPCR
Ribonucleic acid – RNA
RNA binding protein – RBP
RNA integrity number – RIN
RNA-sequencing – RNA-seq
Robust Multi-array Average – RMA
Room temperature – RT
Rosenthal's canal – RC
Sample size – n
Satellite glial cell – SGC
Schwann cell – SC
Sensorineural hearing loss – SNHL
Signal transduction and activator of RNA – STAR
Sound pressure level – SPL
Spiral ganglion neuron – SGN
Spontaneous rates – SR
Transmission electron microscopy – TEM
Tucker Davis Technologies – TDT
Voltage-gated ion channels – VGIC
Voltage-gated potassium channel – VGKC
Voltage-gated sodium channel – VGSC
Wildtype – WT

LIST OF FIGURES AND TABLES

- Figure 1.1.1: Schematic of the auditory nerve
- Figure 1.1.3: Auditory brainstem response test waveforms
- Figure 1.2.1: The auditory nerve glial cells
- Table 2.1.3.3: Primer sequences used for genotyping
- Table 2.4.1: Antibodies used
- Figure 3.3.1: Expression profiles of genes composing nodal structural domains exhibit temporal clustering
- Table 3.3.1: Temporal clustering of differentially expressed node-related genes
- Figure 3.3.2: Hearing onset and maturation of AN function and their relation to SGN subtype differentiation
- Figure 3.3.3 Assembly of nodal and paranodal proteins comprising the axonal and ganglion nodes
- Figure 3.3.4: Node lengths are associated with amplitude growth and decreasing latency
- Figure 3.3.5 Ultrastructural assembly of axonal nodes and flanking paranodes
- Figure 3.3.6: Ultrastructural assembly of ganglion nodes and satellite cell paranodes
- Figure 3.3.7: Completion of heminodal clustering under inner hair cells is temporally dependent
- Figure 3.3.8: Disorganization of the heminodes in a model of profound hearing loss
- Figure 4.3.1: Noise-induced functional declines in the young-adult CBA/CAJ mouse AN
- Figure 4.3.2: Noise-induced demyelination, disruption of paranodal axo-glial junctions, and recruitment of macrophages
- Figure 4.3.3 Expression patterns of QKI variants and potential targets of QKI in response to noise injury
- Figure 4.3.4: Expression patterns of QKI variants in normal postnatal and adult AN
- Figure 4.3.5: Reduction of QKI protein expression in AN glial cells of adult QKIFL/FL;PLPCreERT mice
- Figure 4.3.6: Diminished QKI expression results in demyelination and disruption of paranodal structures in the adult AN
- Figure 5.3.1: Differences in the state of myelination and expression of putative QKI-RBP target genes in ANs between pre-peak and peak myelination
- Figure 5.3.2: Abrogation of QKI RBP expression in myelinating glial cells after knockout of *qkl* gene
- Figure 5.3.3: Developmental-stage dependent QKI-KO induces hypomyelination or dysmyelination of AN fibers at P14
- Figure 5.3.4: *qkl* KO at P5 leads to chronic hypomyelination and morphologically abnormal SCs
- Figure 5.3.5: Eventual dysmyelination of type I SGN fibers and somata in P21 after *qkl* KO at P7

Figure 5.3.6: MBP expression is chronically depleted and Iba+ cells are present in great numbers adjacent to dysmyelinated somata in either qkl KO group

Figure 5.3.7: qkl KO caused abrogated Cntn1 expression and disruption of paranodal structures

Figure 5.3.8: qkl KO-induced hypomyelination leads to loss of AN function

Figure 5.3.9: Eventual dysmyelination due to qkl KO at peak myelination may lead to functional declines in later development

CLARIFICATION OF COMMONLY USED TERMS

Nodal domains – include the node, paranode, and juxtaparanode

Nodal domain-related genes – include genes related to the node, paranode, and juxtaparanode

Excitable nodal domain – the voltage-gated ion channel-filled node region of the heminode, axonal node, and ganglion node

Onset of hearing in the mouse – the time when the ear canal naturally opens and external sound can pass through

ABSTRACT

The auditory nerve (AN) is an integral part of the auditory system and without it, we cannot hear sound. Glial cells insulate type I spiral ganglion neurons (SGNs) with myelin sheaths, which are protective and constrain electrical signal within SGNs, facilitating propagation. Formation of excitable nodal domains containing clusters of voltage-gated ion channels in unmyelinated gaps along axons also allow for rapid saltatory conduction. Sensorineural hearing loss is commonly attributed to loss of synaptic connections between the AN fibers and hair cells, hair cell loss, or SGN death. Primary glial dysfunction in the AN is not as well-studied. Demyelinating diseases such as Guillain-Barre and Charcot-Marie-Tooth, characterized by myelin and nodal abnormalities, result in reduced nerve function manifesting into muscle weakness, sensational changes, and neuropathy. In this dissertation, we identified for the first time three types of excitable nodal domains in the AN and how these nodal structures form/refine during postnatal cochlear development. Our results reveal that maturation of the nodal domains contributes to gain in hearing function. In addition, our data demonstrate that dysregulation of glial function and dysmyelination after noise in young adult AN is partly responsible for noise-induced hearing loss. Lastly, we determined that primary glial dysfunction in AN development via knockout of myelination-regulator *Quaking* results in chronic dysmyelination and abnormal nodal structure formation leading to slower conduction, dyssynchronous AN firing, and hearing loss.

Chapter 1: Introduction

1.1 The neural aspects of the auditory nerve

1.1.1 The spiral ganglion neurons

The mammalian auditory nerve (AN) is composed of thousands of neurons, numbering at approximately 8000 in mice and 30000 in humans^{1,2}. The neurons are divided into two types – the type I and type II spiral ganglion neurons (SGN). The type I SGNs are bipolar neurons which make up ~90-95% of the AN and have their axons myelinated by Schwann cells (SC) and their somata myelinated by satellite glial cells (SGC). The type II SGNs, which make up the remaining AN population, are monopolar, unmyelinated, and smaller in size compared to the type I SGNs. The SGN cell bodies reside in the bony labyrinth of the cochlea, termed Rosenthal's canal (RC), and their peripheral dendrites pass through the shelf of this labyrinth, termed osseous spiral lamina (OSL). The dendrites pass through narrow openings, termed habenula perforata (habenula or hab), to innervate the sensory hair cells (HC) in the organ of Corti on top of the basilar membrane. The central processes enter the central modiolus, which the bony labyrinth coils around, and are organized into a nerve bundle which leaves the cochlea through the tractus spiralis foraminosus to connect to the brainstem.

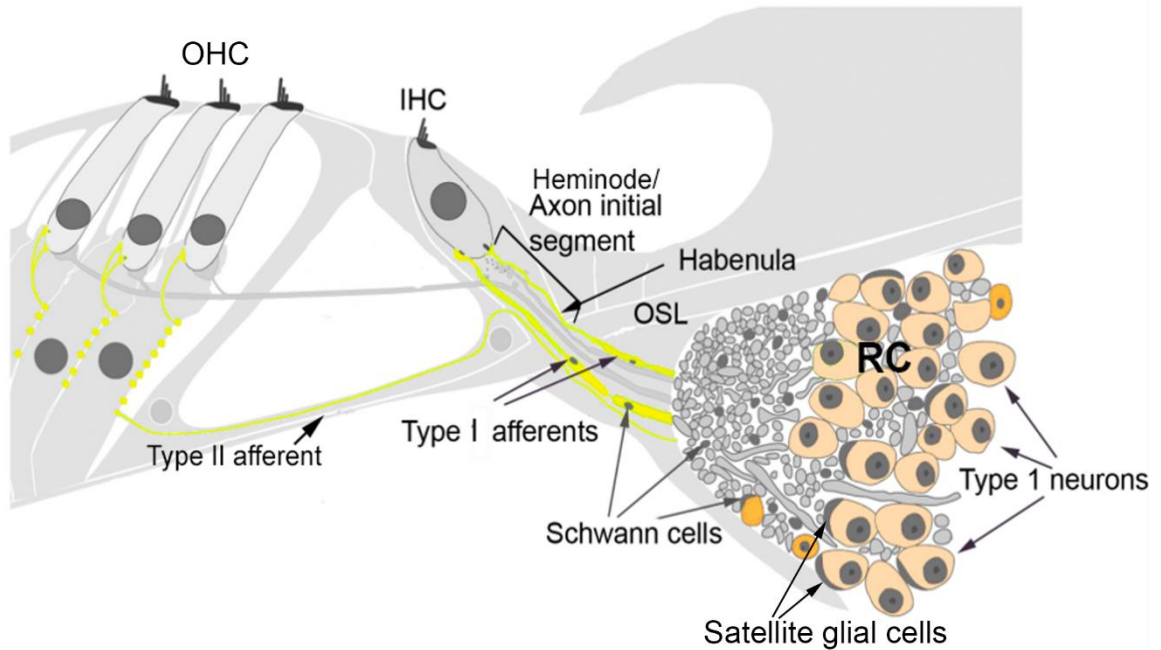


Figure 1.1.1: Schematic of the auditory nerve

The figure shows the afferent neurons of the auditory nerve (AN) connecting to the hair cells (HCs). Type I spiral ganglion neurons (SGNs) are myelinated and connect to the inner HCs (IHC) and type II SGNs are unmyelinated and connect to the outer HCs (OHC). Their cell bodies or soma of the SGNs reside in Rosenthal's canal (RC) and their peripheral afferents pass through the osseous spiral lamina (OSL), and through small holes in the habenula to connect to the HCs. To pass through the habenula, type I SGNs demyelinate; forming the heminodes/axon initial segments. Type I SGNs are myelinated by Schwann cells and satellite glial cells.

The type I SGNs innervate the inner HCs, and together, they are responsible for sensing sound stimulus and encoding its properties into electrical impulses to be relayed to the central auditory pathway. The type I SGNs are the main conductors of sound information in the peripheral auditory system. The outer HCs, by their own mechanical function, are known to amplify sound waves to increase sensitivity and frequency selectivity of the inner HCs³. Therefore, the type II SGNs that innervate these outer HCs may not have much to do with encoding of sound, and their function is less clear than their type I counterparts. In comparison with type I SGNs in response to stimulus, type IIs have slower accommodation (it takes a longer time for stimulus to be translated into action potentials (AP)), lower AP thresholds, and prolonged response to depolarization⁴. Recent studies have suggested that these type II fibers, which have similar properties to C type pain fibers in the nervous system, are playing a role in “auditory nociception” after loud noise exposure, via their trauma-induced increase in activation^{5,6}.

1.1.2 Tonotopic arrangement and frequency- and intensity-based activity of the SGNs

The SGNs and HCs follow a tonotopic arrangement of the cochlear structure – from fibers responding to high frequency at the base, to low frequency at the apex. In terms of function, this arrangement is important for the neural encoding of the frequency property of a given sound wave. For a pure tone sound stimulus, the traveling wave it produces causes the basilar membrane to vibrate at the

cochlear tonotopic location of that pure tone's frequency. Each fiber on the tonotopic arrangement is most sensitive and has the lowest threshold of response to one characteristic frequency (CF)⁷. They do respond to frequency stimuli close to their CF, but the stimuli would need to be stronger to cross a higher threshold level of response. Damaged or degenerated fibers at a certain location will no longer be able to encode response for sounds stimulating that frequency, leading to loss of information.

One type I SGN synapses with one inner HC, but one IHC can be innervated by multiple type I SGNs. Type I SGNs can be further divided subtypes which differ in their spiking properties, even if they innervate the same inner HC. When activity of single neurons were recorded in relative absence of sound, they showed different spontaneous rates (SR) of activity^{8,9}. High-SR fibers have lower thresholds of excitation, while low-SR fibers have higher thresholds of excitation. Therefore, at the lowest audible threshold of sound, it is likely that only the high-SR fibers are contributing to the AN compound action potential (CAP). The high-SR fibers tend to innervate the pillar side (towards the periphery of the cochlea) and the low-SR fibers innervate the modiolar side (towards the center of the cochlea) of the inner HCs. The high-SR fibers tend to be larger and have more mitochondria than their thinner low-SR counterparts¹⁰. The synapse region and number of synaptic vesicles are also increased on the side of the HC where the low-SR fibers synapse¹¹, which may help increase the fibers' activity. Different firing properties of the type I SGNs are thought to increase the dynamic range of intensity of sound that the cochlea can detect.

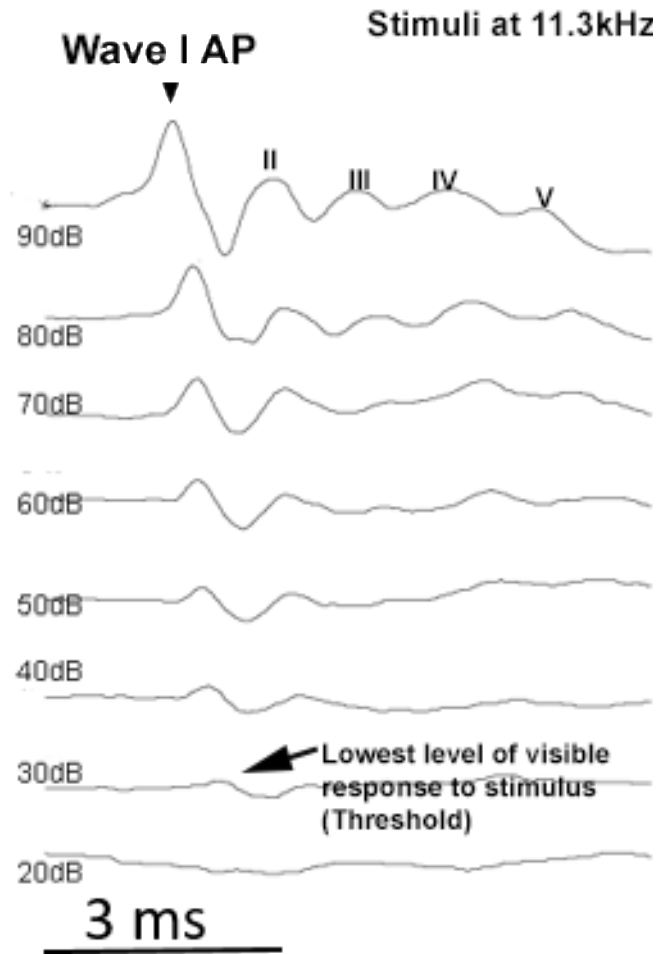


Figure 1.1.3: Auditory brainstem response test waveforms

Example of auditory brainstem responses (ABRs) evoked by stimuli given at the 11.3kHz frequency with decreasing levels of intensity in decibels (dB). The black arrowhead indicates the wave I action potential (AP) response of the AN. The black arrow indicates the threshold, which is the lowest level of visible response to the given stimulus. (Adapted from the Lang Lab, unpublished data).

1.1.3 Auditory brainstem response and neuropathy: Making sense of stimulus-based auditory nerve activity

The auditory brainstem response (ABR) test is a simple method that allows for analysis of stimulus-based AN response. Electrodes placed on the animal record the generated responses from the peripheral AN (Wave I) and at the level of the brainstem from the very proximal AN close to the cochlear nucleus to the lateral lemniscus (Wave II-V) (**Figure 1.1.3**). Although very useful and easy to perform, ABR testing is not the perfect test for AN activity because the evoked responses may also encompass activity of the HCs. Wave I represents the CAP evoked by the AN. The latency of the onset of Wave I can indicate how soon the fibers are activated and how fast they can fire. It would be expected that the high-SR fibers are the main contributors of activity at the onset of latency. Longer latencies of firing could indicate slower conduction velocity of the AN. The peak amplitude indicates the magnitude of response and can suggest in part the synchrony of firing of the fibers. Even though the CAP is a summed response, the width of the wave should indicate information on the firing activities of the various fibers. A shorter width could also suggest synchrony, and fibers contributing to the tail end of the width would be indicative of their slower conduction and higher thresholds of response. Threshold is another important measurement, as it indicates the lowest intensity level of response evoked from the fibers by a given stimulus.

Subjects with sensorineural hearing loss due to loss of HCs or SGNs usually have higher thresholds compared to subjects with normal hearing.

However, it is entirely possible for subjects to have “normal” thresholds compared to their healthier counterparts, but still have hearing impairment. Recent studies have termed this as “hidden hearing loss (HHL),” and is characteristic of having normal thresholds, but with decreased amplitudes compared to normal subjects at suprathreshold responses¹². This suggests that there is no gross loss of HCs or SGNs, but that there is still some form of causative neurodegeneration present. Recent studies have shown that degeneration of synapses or heminodes of the SGN afferents can be implicated with causing HHL. A study by Kujawa and Liberman has shown that the permanent decrease of suprathreshold amplitude responses, even after threshold response has recovered to normal after noise-exposure, is due to synaptopathy of the SGN afferents and not loss of HCs¹³. The disruption of the heminodal organization may also be a cause of HHL¹⁴. The heminode is the unmyelinated portion of the SGN axon as it crosses the habenula to innervate the HC, and it is myelinated on its side that is proximal to the soma by a SC. The heminode is an excitable nodal domain that is said to be the site of action potential generation in the SGN¹⁵, akin to the axon initial segment at the axon hillock of multipolar neurons. This is a very interesting finding because it highlights the importance of proper maintenance and function of auditory glia cells and excitable nodal domains on normal auditory function.

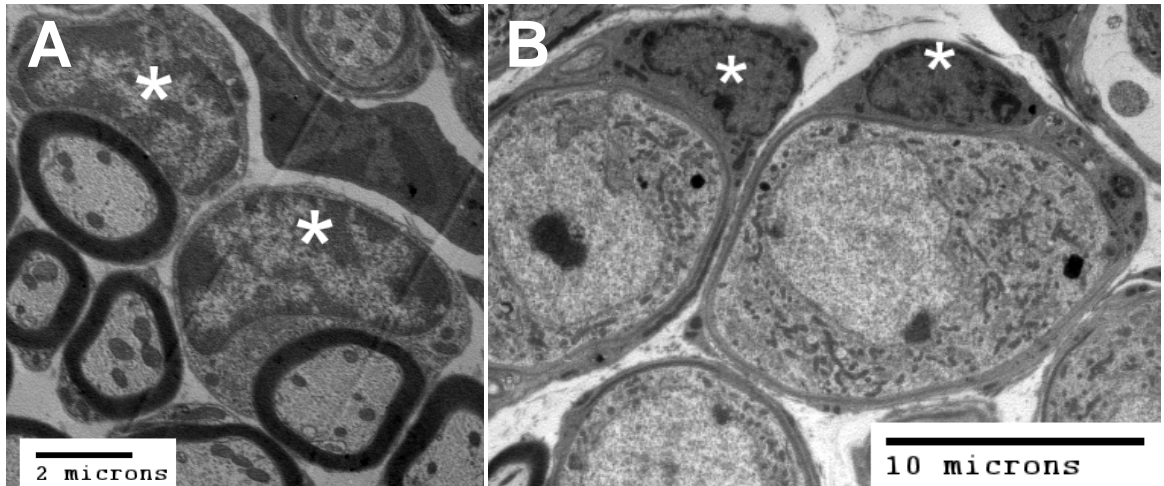


Figure 1.2.1: The auditory nerve glial cells

A The asterisks indicate the nuclei of myelinating Schwann cells (SCs). The SCs enwrap the type I SGN axons with dense myelin lamellae. **B** The asterisks indicate nuclei of myelinating satellite glial cells (SGCs) which surround the type I SGN somata with myelin layers that are less dense compared to the Schwann cell myelination of axons.

1.2 Glial cells and myelination

1.2.1 The auditory glial cells

There are two types of peripheral glia cells in the cochlea – the satellite glia cells (SGC) and the Schwann cells (SC) (**Figure 1.2.1**). SGCs myelinate the somata of Type I SGNs. Besides electrical insulation, SGCs may play a role in neuroprotection by providing trophic support to the soma¹⁶. Death of the SGCs in young-adult mouse ANs by accumulation of sulfatides led to eventual primary degeneration of SGNs¹⁷. Myelinating SCs form dense, multi-layered myelin sheaths around the type I SGN peripheral axons, and one SC myelinates only one axon. SCs also myelinate the central processes of SGNs, up until the glial transition zone near the tractus spiralis foraminosus, where the nerve fibers become myelinated by oligodendrocytes of the central nervous system¹⁸. The compression of each layer of the multi-layered myelin sheath gives it its characteristic dark, electron-dense appearance. Conduction velocities of neurons are greatly increased by myelin insulation. Non-myelinating SCs ensheath multiple type II SGNs, each with at least one cytoplasm-dense process.

1.2.2 Myelination in the peripheral nervous system during development

The SCs of the AN and the rest of the peripheral nervous system (PNS) originate from the neural crest, which are able to give rise to both neurons and glia, amongst other cell types¹⁹. These neural crest cells transition into SC precursors at embryonic (E) days 12-13 in mice²⁰. Factors inducing this transition

into SC precursors are not absolutely clear, although studies have shown that NRG1²¹ and Notch²² signaling can inhibit neural crest cells from turning into neuronal precursors and instead promote gliogenesis. The SC precursors grow in close proximity to the axons they will ensheath and their survival is promoted by axonal NRG1 neurotrophic factor signaling to erbB receptors expressed on the SC precursors²³. These then transition into immature SCs by E12-15 in mice and are capable of promoting their own survival via autocrine signaling²⁰. These immature SCs ensheath groups of axons. Radial sorting will then occur, in which an immature SC will ensheath a single axon, usually one that is large in caliber, and become pro-myelinating²⁴. The remaining immature SCs ensheathing smaller caliber axons, are designated to be mature, non-myelinating SCs. Studies suggest that the reason large axons are chosen for myelination is because they express more NRG1 type III ligands on their axons, which the erbB receptors on the immature SCs can contact, and that these ligands are strongly able to induce myelination by activating PI-3kinase pathway in the SCs²⁵. There are several signaling factors that promote myelination, and the majority of them converge to upregulate the expression of or activate Krox 20, which is considered the master transcriptional regulator of myelination and terminal differentiation of SCs^{26,27}. Markers of mature myelinating SCs include expression of proteins such as P0, MBP, and PMP22, which are structural components of compact myelin sheaths²⁷.

In the PNS, remyelination of the injured or demyelinated nerve can readily occur because of the highly plastic nature of mature SCs. After injury, the mature

SCs can degrade and phagocytose their own myelin at the site of injury²⁸. Through the actions of the transcription factor c-Jun, the mature SCs can transdifferentiate into glia cells specialized for repair and regeneration of the axon²⁹. SCs also proliferate in order to provide trophic support and replace dead SCs. SCs can then re-differentiate in order to remyelinate the repaired axon, possibly through the direction of NRG1 Type I signaling³⁰. However, remyelinated fibers tend to have thinner myelin and slower conduction velocities than their undamaged counterparts³¹.

Evidence of remyelination and axon regeneration in the AN is not as widespread as it is in other peripheral systems. However, some studies do suggest that auditory glia cells may play a role in axonal regeneration. Research studying dissociated SGNs grown in co-culture with multiple non-neuronal cell types from the spiral ganglion region showed that the neurites grown out from the SGNs spontaneously associated with auditory glia cells in the culture³². Another study has shown that auditory glia cells may dedifferentiate back into an immature phenotype, as marked by upregulation of Sox2, and can proliferate after induced AN injury³³. These studies suggest that signaling from auditory glia cells could help promote regeneration of SGNs and that the glia cells also play a role in injury response in the cochlea.

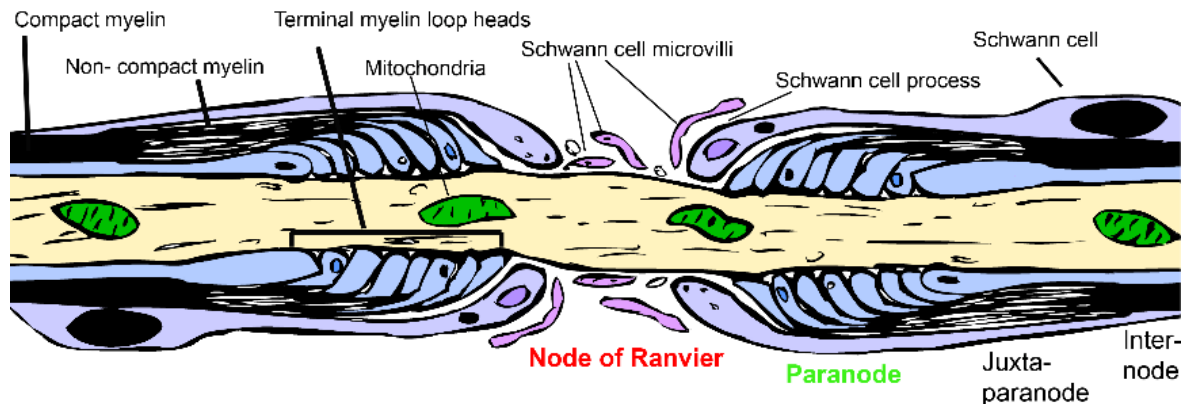


Figure 1.3.1: Schematic of a node of Ranvier and flanking segments

The node of Ranvier is the unmyelinated gap between myelin sheaths created by two separate SCs. The nodal axolemma (i.e., excitable nodal domain) is filled with voltage-gated sodium channels (VGSCs) that are responsible for AP regeneration. Thick, cytoplasm-filled SC processes may extend over the node. The paranodal region is where the myelin lamellae terminate (i.e. terminal myelin loop heads) and form axoglial connections with the paranodal axolemma. This physical barrier acts to separate the VGSCs in the node from the voltage-gated potassium channels in the juxtapanode (VGKC). The VGKCs are responsible for repolarization of the nodal structure and act to reduce hyperexcitability of the neuron. Lamellae at the paranodal-juxtapanodal regions are non-compact, but gradually become more compact towards the myelinated internode region.

1.3 The nodes of Ranvier and flanking nodal domains

1.3.1 The nodes of Ranvier of the PNS

Formation of myelin sheaths on the axon allows for the creation of unmyelinated gaps between opposing myelin sheaths. These naked gaps, commonly termed nodes of Ranvier in other neural systems, are the primary site of ion exchange across the axonal membrane and cluster voltage-gated sodium channels (VGSC) that are necessary for depolarization for the generation/regeneration of AP (**Figure 1.3.1**). When an electrical stimulus is strong enough to cross the threshold of excitation, the VGSCs open to allow sodium inside the axon, leading to a depolarization event which produces the AP. Because of myelin insulation, the electrical signal cannot be lost via diffusion across the axolemma and the AP can rapidly propagate forward to the next excitable nodal domain to cause another depolarization/AP regeneration. Aside from the rapid conduction velocity, myelination also reduces the metabolic cost of AP propagation³⁴ and provides structural support which helps allow for larger axonal calibers³⁵.

Clustering of the VGSCs at the node is made possible by complexes formed in the node region. Myelinating glia express gliomedin and glial-NrCAM at the SC microvilli contacting the node space^{36,37}, and complex with Nfasc186³⁸ and axonal-NrCAM in the nodal axolemma. During development, these proteins initiate the formation of the node by recruiting anchoring protein, Ank-G, and scaffolding protein, BIV-spectrin, which cluster and stabilize the VGSCs at the

node^{39,40}. In addition, complexes forming axoglial junctions between the terminal loops from each myelin lamellae and the axolemma at the paranode regions flanking the node serve as physical lateral diffusion barriers that help to cluster and stabilize the node components⁴¹⁻⁴³. These axoglial complexes are made up of glial Nfasc155 and axonal Cntn1 and Caspr. The paranode regions also act to physically separate the nodal VGSCs from the juxtaparanodal voltage-gated potassium channels (VGKC). In sciatic nerve studies, loss of axoglial connections at the paranode can cause the VGKCs and VGSCs to diffuse towards each other and lead to lower conduction velocities^{42,44}. These previous studies in sciatic nerves have also shown that the nodal and paranodal components are required for proper VGSC clustering, because their genetic knockout in development or induced loss in adulthood cause loss of/aberrant clustering of VGSCs, elongation of the node region, and overall decrease in nerve conduction velocity and excitability.

The juxtaparanodal region is the domain in between the paranode and internode and is covered by non-compact myelin lamellae. The VGKCs are anchored to the juxtaparanodal axolemma by transmembrane Caspr2^{45,46}. The clustering of VGKCs by Caspr2 is assisted by the axo-gial cellular adhesion molecule Cntn2⁴⁶. These VGKCs assist in repolarization and inhibit aberrant repetitive AP firing⁴⁷. Reduced expression of VGKCs at the juxtaparanode after nerve injury is associated with neuronal hyperexcitability⁴⁸. Studies have shown that SCs may be required for normal distribution and localization of VGKCs in the juxtaparanode after remyelination and that their presence at the juxtaparanodal

domain is more dependent on maintenance by SCs compared to presence of the less transient VGSCs at the node⁴⁹. Besides losing electrical insulation along the internode and mislocalization of VGSCs and VGKCs across the nodal domains, demyelination can lead to uncovering and exposure of VGKCs at the juxtaparanodal axolemma, contribute to decreased excitability of the neuron⁴⁹.

1.3.2 The excitable nodal domains of the auditory nerve

In the murine AN, there are three different types of excitable nodal domains (Lang Lab unpublished data, ⁵⁰). There is the heminode, as previously mentioned in the preceding sections. Then there is the axonal node, which is flanked on both sides by paranode regions myelinated by SCs, and of which there is at least one along the peripheral dendrite of the SGN. The exact number per dendrite is yet to be determined. Lastly, there is the ganglion node, aptly named because they flank the ganglion body on both sides. These are myelinated on the axonal side by a SC and the soma side by a SGC. SGC paranode axolemma is contacted by much less compact terminal myelin loops compared to the SC paranode side (Lang Lab unpublished data). The ganglion nodes also tend to have longer gap lengths compared to the axonal nodes (Lang Lab unpublished data). As of now, not much is known about the differences in depolarization and action potential firing properties of each excitable nodal domain, or if the axonal nodes vary in number or location along the SGN depending on where the fiber is on the tonotopic map. Any of these variations, if they exist, may help contribute in some way to the different characteristics of the

fibers along the cochlea. To elucidate some information of the different excitable nodal domain AP generation properties, it may be possible to infer some information from their VGSC composition densities and gap lengths. Aside from the previously stated hearing impairment associated with heminodal disruption, elongation of axonal node gaps and dysmyelination at the paranodes after acoustic overexposure are also correlated with hearing loss⁵¹. This loss of function manifested from the decreased conduction velocity and conduction block of the auditory fibers, possibly because of the abnormal nodes. These recent findings in the cochlea have helped highlight the contribution of the understudied excitable nodal domains of the AN to hearing function.

1.4 The Quaking RNA binding proteins as regulators of myelination and paranodal maintenance

Indication of the role of the quaking gene (*qkl*) in myelination was first realized through its spontaneous mutation in the DBA/2J mouse strain, which manifested in hindlimb tremors seen starting at postnatal day 10 and demyelination of the central and peripheral nervous systems⁵². The demyelination and tremors of these *quaking viable* mice were found to be caused by loss of the *qkl-6* and *qkl-7* isoforms⁵³. The *qkl-6* isoform is located in the nucleus and cytoplasm of glia cells and *qkl-7* is also found in glial cytoplasm. These two isoforms are highly expressed during myelination. The third *qkl* isoform, *qkl-5*, is upregulated during embryogenesis, is located in the nucleus, and is not affected in the *quaking viable* mice, which is why they can survive.

This ground-breaking study by Ebersole et.al. has identified the isoforms to differ only in their C-terminal regions and classified them as part of the signal transduction and activator of RNA (STAR) family of proteins⁵³. These isoforms are translated into quaking (QKI) RNA binding proteins (RBP) that each have a STAR domain. This domain is made up of the QUA1 region, which is necessary for isoform dimerization⁵⁴, and the KH and QUA2 regions, which are necessary for binding to targets with quaking recognition elements (QRE)⁵⁵. RBPs are regulators of glia differentiation, myelination, and paranodal formation through post transcriptional modifications of target RNAs. Demyelination in *quaking viable* mice may be due in part to the nuclear retention of *MBP* RNA by QKI-5 in the absence of competitive binding by QKI-6/7⁵⁶. Sole presence of QKI-5 in the *quaking viable* mice is also implicated in aberrant alternative splicing of *MAG* pre-mRNA, an important myelin component, leading to an imbalance in *MAG* protein isoform expression⁵⁷. Addition of QKI-6/7 to SC and neuron co-cultures inhibited proliferation of SCs and promoted myelination, possibly through inducing the expression of the pro-myelinating factor p27kip1⁵⁸. Recently, a knockout model inducing the deletion of all three *qki* isoforms has led to the finding that QKI-5 affects alternative splicing of the nodal/paranodal *Nfasc* pre-mRNA⁵⁹. Loss of paranodal *Nfasc155* expression after the induced knockout led to loss of axo-glial connections and dysmyelination at the paranodes. These current findings suggest that QKI RBPs are important regulators of myelination and paranodal maintenance.

1.5 Sensorineural hearing loss and dysmyelination

1.5.1 Sensorineural hearing loss

Hearing impairment (HI) is an epidemic affecting people of all ages worldwide, with diagnoses ranging from slightly detectable to debilitating, profound loss. Approximately 2 to 3 out of 1000 infants screened had congenital hearing loss in the United States alone, and that increased to an estimated 6 per 1000 live births in developing countries^{60,61}. A study conducted on 20-69 year-old men and women sampled from different demographics estimated that 27.7 million Americans had speech-frequency HI, while 61.1 million had high-frequency HI⁶². The most common cause of HI is sensorineural hearing loss (SNHL). The term SNHL roughly describes a two-part condition – the dysfunction or loss of sensory hair cells (HC) which are responsible for mechanotransduction of sound into electrical impulses, and the dysfunction or loss of the peripheral AN fibers. AN afferents synapse with HCs and serve as the first part of the auditory relay and processing system that ends with the central auditory cortex. At present, the best treatments include the use of sound amplification devices, such as hearing aids, and cochlear implants for direct stimulation of *intact* AN⁶³. These are invaluable forms of treatment, especially for those whose suffering is mainly due to sensory hair cell damage/loss, but these devices mostly function to patch the problem instead of addressing the root cause.

1.5.2 Demyelination and hearing loss

Demyelinating diseases, such as Charcot-Marie-Tooth (CMT) and Guillain-Barre Syndrome (GBS) are long known to be associated with HI. The *Trembler* mouse model of CMT present with paranodal dysmyelination which, in addition to the dysmyelinated internodes, may contribute to their phenotypic tremors⁶⁴. Some patients with GBS were shown to have antigens against nodal and paranodal molecules⁶⁵. Preservation of proper myelination and nodal structures are necessary for retaining and optimizing the physiological function of SGNs. At present, there has not been much research on the development of electrically excitable nodal domains in the cochlea and gaining such knowledge will allow us to have a comparative standard for mutant or disease models.

Auditory glial cells are important for maintenance and support of SGNs. Previous studies in animal models and in humans have shown that SGNs can survive after primary sensory HC loss, and can remain with relatively-intact somata and central processes, but with degenerated peripheral dendrites⁶⁶⁻⁶⁸. SGCs have been shown to play a role in SGN survival, possibly due to neuroprotective support via intercellular channels³⁶. Degeneration of SGCs and subsequent demyelination of SGN axons in a mouse model of myelin component deficiency eventually led to degeneration of SGNs⁵⁷. Recent studies have shown that synaptopathy and SC disruption can be primary causes of hearing loss. The ground-breaking publication by Kujawa and Liberman showed that synaptopathy can occur after noise exposure and lead to hearing deficits even as the HCs remain normal¹⁷. Very recently, a study has shown that transient ablation of SCs

caused chronic disruption of the heminodes, but had no effect on HCs or synapses¹⁴. The heminodal disruption was associated with permanent increase in latency and decrease in amplitude of AN responses. As well as being important for insulating the neurons, myelinating glia express components necessary for the initiation of nodal assembly³⁶. De-regulation of glial function, leading to glial dysfunction may disrupt nodal assembly and cause loss of nodal structural integrity in addition to dysmyelination. The ensuing loss of structural integrity of the nodal domains and myelin may contribute to loss of AN function.

1.6 Purpose of this study

Environmental sound is mechanotransduced by sensory hair cells into electrical impulses that are promptly propagated by the AN to the central auditory system for processing. SGN peripheral axons are myelinated by SCs and the somata are myelinated by SGCs beginning around P2 and with peak myelination occurring at around P7. Excitable nodal domains, commonly known as nodes of Ranvier, and proper myelination are required for fast conduction of action potentials along bipolar type I SGNs of the AN. Preservation of myelin and nodal structures are essential for normal auditory response, and understanding their postnatal development in the AN would be an important step for conceiving gene-based therapeutic approaches to hearing loss. The roles of abnormalities in myelination by AN glial cells and nodal segments of the AN in sensorineural hearing loss are understudied. With our research, we will take the opportunity to study *qkl* and its role in regulating AN myelination. With this project, we will

address the questions of 1) how the nodal domains normally develop in the AN before and after hearing onset, and if auditory glial dysfunction can lead to dysmyelination and abnormal nodal assembly resulting in hearing deficits 2) after noise injury and 3) during AN development. Our overarching goal is to determine the contribution of normal nodal structures to hearing maturation in development and to elucidate the effects of glial dysfunction due to *qkl* knockout on AN function.

Chapter 2: General methods

2.1 Animals

2.1.1 Vivarium and parameters for use

Mice, unless specified otherwise, were bred and kept in a low-noise environment at the Medical University of South Carolina's (MUSC) Animal Research Facility. All aspects of animal research were conducted in accordance with the guidelines of the Institutional Animal Care and Use Committee of at MUSC. All mice received food and water *ad libitum*. The animal rooms were maintained on a 12-hr light/dark cycle. Subjects with signs of external ear canal and middle ear obstruction or middle ear infection were excluded. Whenever possible, mice of either sex were used for the studies.

2.1.2 Normal hearing and noise studies

The CBA/CaJ mouse strain is commonly used for normal hearing studies due to their lack of genetic mutations related to hearing and their ability to age without progressive hearing loss⁶⁹. The CBA/CaJ mice were purchased from the Jackson Laboratories (Bar Harbor, ME). Postnatal (P) mice ages P0, 3, 7, 10, 14, 21, and 1-month-old were used for the developmental studies. Young-adult CBA/CaJ mice aged 6-15 weeks were used for the noise studies.

2.1.3 Mutation models

2.1.3.1 Diminuendo

The Diminuendo (Dmdo) mouse strain, with an N-ethyl-N-nitrosourea (ENU) induced point mutation that leads to immature stereocilia and hair cell development, were acquired from the lab of Dr. Karen P. Steel and were also bred and kept at MUSC⁷⁰. These mice were kept in the C3HeB/FeJ background strain. Dmdo pups were genotyped to select for homozygous (Dmdo/Dmdo) animals that are characterized to be profoundly deaf at birth⁷¹, and their wildtype (WT (+/+)) littermates as controls. Mice aged P14 of either sex were used for the studies.

2.1.3.2 Quaking

The $QKI^{FL/FL;PLP-CreERT}$ model⁵⁹ was produced by crossing $QKI^{FL/FL}$, which has loxP sites flanking exon 2 of *qkl*, with $PLP-CreERT$ ⁷². This mutation model was used to knockout the *qkl* isoforms 5, 6, and 7, which encode the QKI RBPs 5, 6, and 7 respectively. With the $PLP-CreERT$ cross, the knockout of *qkl* occurs in *Pip1*-expressing cells, which in the AN are the auditory nerve glial cells. These mice were kept in the C57BL/6J background strain. Knockout of *qkl* was induced via intraperitoneal injections of 10mg/ml 4-hydroxytamoxifen (TAM) diluted in corn oil. A portion of the studies using young-adult $QKI^{FL/FL;PLP-CreERT}$ model were performed in the Lady Davis Institute for Medical Research Small Animal Research Core at McGill University in Montreal, Quebec, Canada. The

collaborative research at McGill University were conducted in accordance with the McGill University guidelines set by the Canadian Council on Animal Care. For the postnatal Quaking studies, the $QKI^{FL/FL}$ and $PLP-CreERT$ mice lines were imported from the Richard Lab at McGill University to MUSC.

To establish the line at MUSC, the $QKI^{FL/FL}$ mouse was bred with C57BL/6J to obtain $QKI^{FL/-}$ offspring. Heterozygous $QKI^{FL/-}$ mice were mated together to produce homozygous $QKI^{FL/FL}$. Homozygous $QKI^{FL/FL}$ breeder pairs were used to maintain the Quaking mouse line. The $PLP-CreERT$ mouse was bred with C57BL/6J to obtain offspring hemizygous for $PLP-CreERT$ and to maintain the mouse $PLP-CreERT$ mouse line. Hemizygous $PLP-CreERT$ were then bred with homozygous $QKI^{FL/FL}$ mice to produce $QKI^{FL/-};PLPCreERT$ offspring. These were then mated to with $QKI^{FL/FL}$ mice to obtain the $QKI^{FL/FL};PLPCreERT$ pups to be used for the conditional Quaking knockout (i.e., QKI-KO mice). For these studies, either $QKI^{FL/FL}$ or $QKI^{FL/-}$ littermate mice negative for the $CreERT$ were used as controls (i.e., QKI-Ctrl mice). Protein expression analyses from our collaborator⁵⁹ and our own experimental results on the control mice showed no significant difference between the homozygous and heterozygous flox.

2.1.3.3 Genotyping

Experiment-appropriate Diminuendo and Quaking pups were selected via genotyping. DNA was extracted from tail clippings from each mouse either by using the Genra Puregene Mouse Tail Kit (Qiagen, Germantown, MD) and the associated manufacturer's instructions or via the quick genotyping method which

consists of extraction by hot sodium hydroxide and tris as described by Truett et.al., 2000⁷³. The extracted DNA was then used to amplify the identifying, target sequence via polymerase chain reaction (PCR) (see **Table 2.1.3.3** for primers used).

The amplified sequence from the Diminuendo mice shows up as one band at 224bp and the band cannot indicate if the sample came from a Dmdo/Dmdo or Dmdo/+ mouse. To determine the genotype, the samples were sent out to Genewiz (South Plainfield, NJ) for sequencing. From the sequences, homozygous mice can be identified by the A to T mutation in the mir-96 seed region⁷⁰.

To select for QKI-KO versus littermate QKI-Ctrl, the PCR products were run on 2% agarose gels. Amplification for the Cre and QKI-2lox sequence were performed on each sample. We searched for the single Cre band present at ~100bp. For the QKI-2lox amplification, we searched for bands at 309bp and 191bp. A single band at 309bp is indicative of homozygous $QKI^{FL/FL}$ while a single bad at 191bp is indicative of a flox null mouse. Bands at both 309bp and 191bp is indicative of a heterozygous $QKI^{FL/-}$ mouse. Due to our breeding scheme, we conclude that our $QKI^{FL/FL};PLP^{CreERT}$ mice should be hemizygous for $PLP-CreERT$, since our original $PLP-CreERT$ breeding pair consisted of a $PLP-CreERT$ mouse and a C57BL/6J mouse.

Table 2.1.3.3: Primer sequences used for genotyping

Primer	Sequence
Dmdo Forward	AGACCTCCTCTGCTCCTTCC
Dmdo Reverse	CTCCTCACCCAGCAGTAAGC
Cre Forward	GCGGTCTGGCAGTAAAACTATC
Cre Reverse	GTGAAACAGCATTGCTGTCACTT
QKI-2lox Forward	ACAGAGGCTTTTCCTGACCA
QKI-2lox Reverse	TTCAGAACCCCCACATTACC

2.2 Physiological studies

2.2.1 Auditory brainstem response

For each auditory function measurement, animals were anesthetized via an intraperitoneal injection of 20 mg/kg xylazine and 100 mg/kg ketamine cocktail. ABRs were performed in a sound-isolation booth with the lights turned off. Each ABR equipment was professionally calibrated before use, and sound stimuli were delivered into the ear canal via a 10mm long, 3-5mm diameter tube. Unless otherwise stated, ABR measurements were acquired via Tucker Davis Technologies (TDT) equipment System III (Tucker Davis Technologies, Gainesville, FL) and processed via SigGen software package (Version 4.4.1) following the Lang Lab protocol used in previous studies⁷⁴. For postnatal and young-adult CBA/CaJ mice, stimuli were evoked at 4, 5.6, 11.3, 16, 22.6, 32, 40, and 45.2 kHz frequencies. The stimuli consisted of 5ms-duration tone pips with cos² rise/fall times of 0.5ms and were delivered 31 times/s with a period of 32.2581ms. Responses were collected from 90 to 10dB SPL sound intensity levels, with each succeeding level being reduced by 5dB steps. Results for each mouse tested were analyzed for wave I threshold.

2.2.2 Continuous ABR method to calculate Phase Locking Value (Intertrial Coherence) and other metrics of wave I

ABR activity was recorded continuously using TDT OpenEx. ABRs were evoked at 1.1ms-duration pure tone at 11.3kHz frequency with cos² rise/fall

times of 0.55ms. Stimuli were presented at a rate of 21 times/s with a period of 47.619ms. Data was epoched offline (-2 10ms). Time frequency analysis was used to estimate the mean Phase Locking Value (PLV) of wave I via EEGLab. Estimation of the PLV aims to measure the synchrony of AN firing across a given number of trials (i.e., intertrial coherence). Peak amplitude and peak latency were obtained from average responses via ERPLab. This method was adapted for use in mice from methods used by the Harris Lab in their human studies⁷⁵.

2.3 Transcriptomic analyses

2.3.1 Cochlear nerve tissue collection and total RNA isolation

Cochleas from young-adult noise-exposed, non-noise-exposed controls, and postnatal CBA/CaJ mice were collected at their designated end-points for RNA isolation. Microdissections were performed to isolate the whole AN from the rest of the cochlear structures, taking care to preserve peripheral fibers and to exclude the components of the organ of Corti, vestibular system, and lateral wall. Each individual sample consisted of total RNA from both ANs per mouse. Purification of total RNA from the samples required the use of the miRNeasy Mini Kit (Qiagen Inc, Germantown, MD) and the manufacturer's instructions were followed for the isolation. Contamination of genomic DNA was removed during the RNA isolation via genomic DNA binding columns. Quality of the RNA products was assessed using the Agilent 2100 Bioanalyzer (Agilent

Technologies, Santa Clara, CA). Samples that showed degradation or contamination of genomic DNA were excluded from the experiments.

2.3.2 Microarray hybridization

Procedures for probe preparation, hybridization, and microarray data processing were modified from those described previously⁷⁶. Total RNA amounting to 50 ng was converted into biotin-labeled cRNA using the 3' IVT Express Kit (Affymetrix, Santa Clara, CA). Each group consisted of 2 biological replicates. Hybridization to Mouse 430 2.0 GeneChips (Affymetrix) and post hybridization washing, staining, and fluorescence scanning were conducted using Affymetrix instrumentation following manufacturer recommendations. Normalized hybridization data was obtained by Robust Multi-array Average (RMA)⁷⁷ and detection calls obtained by MAS 5.0 using Expression Console software (Affymetrix).

2.3.3 RNA sequencing

Total RNA (50 ng) with RNA integrity numbers (RIN) of 8.9-10 were used for the RNA-sequencing (RNA-seq) experiments. Each group consisted of 3 biological replicates. Library preparation and paired-end next-generation sequencing using the Illumina HiSeq2500 was performed by the MUSC Genomics Share Resource Core. Data was generated in FASTq format. The MUSC Bioinformatics Core used the FASTq datasets to create files of raw counts of gene expression and as well as log₂ transformed, normalized count

files via DeSeq2. For the following experiments, the log₂ transformed, normalized count datasets were used.

2.3.4 Quantitative PCR

Detailed descriptions of quantitative PCR (qPCR) experiments for each study are included under each chapter. In short, two-step reverse transcription qPCR (RT-qPCR) was performed. First, total RNA was converted into cDNA via reverse transcription. Then, the resulting cDNA products were used to query for expression of genes of interest via qPCR. Depending on the experiment, either TaqMan probes (Applied Biosystems) or commercial/custom DNA oligo primers paired with SYBR dye chemistry. Each experiment included a no RT control and the reactions were performed in technical triplicate with 40 cycles of 2-step cycling. Melting curve analyses were also performed after each procedure. The melting curve profiles were reviewed to ensure that all amplifications produced single and specific products. For our studies, relative expression of target genes were measured by either one of two ways. The first quantification protocol included preparation of a standard curve from 10-fold serial dilutions of our DNA preparations to determine efficiency of amplification and ensure that our efficiencies were not suboptimal. Relative expression was then calculated via the $\Delta\Delta CT$ method as described^{78,79}. The second quantification method was to use the PCR Miner webtool which uses an algorithm to quantify efficiency and cycle threshold (CT) values of our genes of interest⁸⁰. The formula $1/(1+Efficiency)^{CT}$

was used to calculate the R0 values. Expression of our genes of interest were normalized using tissue-appropriate reference genes.

2.4. Histological analyses

2.4.1 Immunostaining and confocal imaging

Immunostaining procedures were modified from previous studies⁷⁴. At each designated time-point, mouse cochleae were collected and immediately fixed with 4% paraformaldehyde (PFA) solution in 1x phosphate buffered saline (PBS) for 2 hours at room temperature (RT) and decalcified with 0.12M ethylenediamine tetraacetic acid (EDTA) at RT for 1-2 days. For mouse cochlear section preparations, the cochleae were embedded in Tissue-Tek OCT compound and sectioned at thickness of ~10 μ m. For whole-mount preparations of mouse cochlear tissues, the ANs and attached organs of Corti were isolated from the rest of the cochlear structures. Fluorescent tagging of primary antibodies were achieved either indirectly using biotinylated secondaries conjugated with fluorescent avidin (Vector Labs, Burlingame, CA) or directly using Alexa Fluor Dyes (ThermoFisher Scientific, Waltham, MA). Counterstaining of nuclei were achieved using propidium iodide (PI), Hoescht, or DAPI. Slice and confocal image stacks were collected using a Zeiss LSM 880 NLO with a ZEN acquisition software (ZEISS United States, Thornwood, NY) or a Leica SP5 with an LAS AF acquisition software (Leica Microsystems Inc., Buffalo Grove, IL). Image stacks were taken at 0.75 μ m intervals with image sizes of

134.95 μm (x) x 134.95 μm (y) from the Zeiss and 144.72 μm (x) x 144.72 μm (y) from the Leica. Images were processed using ZEN 2012 Blue Edition (Carl Zeiss Microscopy GmbH), Leica Application Suite X (Version 3.0.2.16120) (Leica Microsystems CMS GmbH), and Adobe Photoshop CC (Adobe Systems Incorporated). A detailed list of antibodies used is in **Table 2.4.1**.

2.4.2 Identification of nodal structures and measurement of excitable nodal domain lengths

Excitable nodal domains were marked via immunostaining of either anti-NrCam or anti-Nav1.6. Paranodal domains were marked via immunostaining of anti-Cntn1. Node dimension measurements were performed on image stacks that were converted to maximum intensity projections. Node of Ranvier measurements were acquired using the measurement tool on ZEN. Confocal image stacks taken at 0.75 μm intervals from 10 μm cochlear frozen sections were processed into a single-layer maximum intensity projection. Length was considered as one end of the NrCAM node marker to the other end (**see Figure 2.4.2**). Wholly-intact nodes in the parallel plane were measured to limit possible inaccuracies. Node parallelism and wholeness were checked using (1) the presence of flanking paranodes, (2) 3D visualization of the tissue section using ZEN, and (3) the range-indicator tool on ZEN.

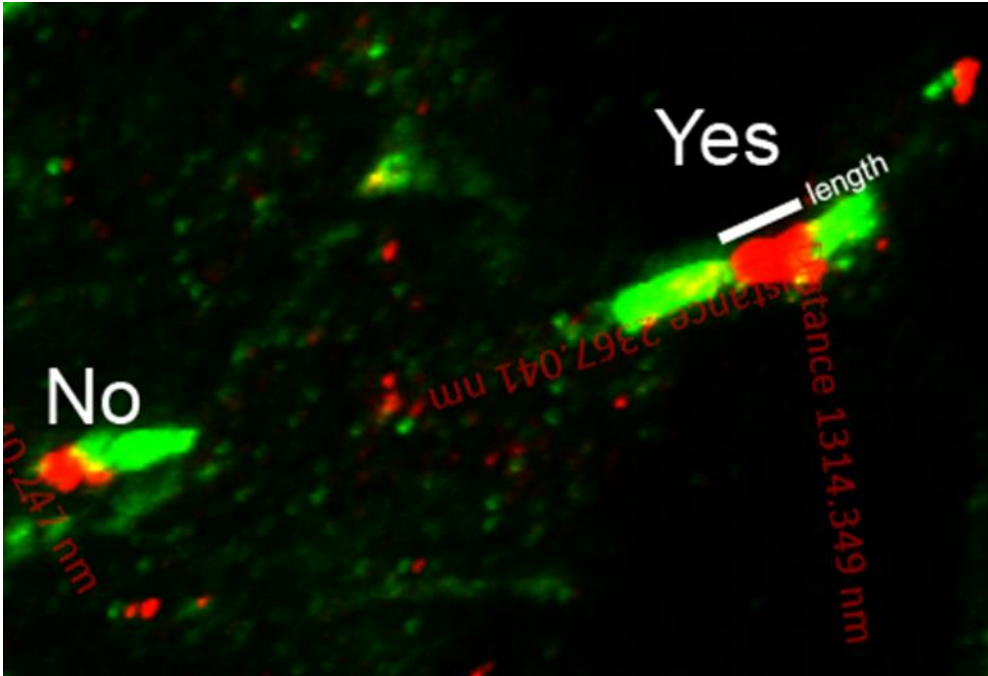


Figure 2.4.2: Node length measurement

This figure shows an example of a parallel axonal node that is good for measuring (indicated by “Yes”) and an axonal node that is not good for measuring (indicated by “No”). The excitable nodal domain is marked by immunostaining for anti-Nrcam (red) and the paranodal flanks are marked by staining for anti-Cntn1 (green).

2.4.3 Transmission electron microscopy

The tissue preparation and imaging procedures for transmission electron microscopy (TEM) were described previously⁷⁴. Briefly, mice 1 month-old and above were anesthetized and tissue was fixed via cardiac perfusion with a 4% PFA and 2% glutaraldehyde solution diluted in phosphate buffer. The collected cochleae were then further perfused with the fixative solution through the round window. Cochleae from mice \leq P21 were perfused with the fixative 3 times through the round window, as the mice were too small for cardiac perfusion. The 1 month-old and older cochleae were then kept overnight in the fixative at 4°C. The P21 and younger cochlea were kept for 4-7 days in the fixative at 4°C. To image cochlear sections without knife marks and to inhibit destruction of the diamond knife used to section cochlea, the samples were kept in EDTA for 2-3 days for thorough decalcification. Cochleae were post-fixed using a 1% osmium tetroxide and 1.5% ferrocyanide solution for 2 hours in the dark, subsequently dehydrated, and then embedded in Epon LX 112 resin. Semi-thin sections for pre-TEM observation of AN orientation were cut at 1 μ m thickness and stained with toluidine blue. Once a coronal plane for a given cochlear turn could be observed, ultra-thin sections at 70nm thickness were cut and stained with uranyl acetate and lead citrate and then examined using a JEOL JEM-1010 transmission electron microscope (JEOL USA, Inc., Peabody, MA).

2.5 Statistical analyses

Unless otherwise indicated, sample sizes (n) for each quantified measurement were a minimum of 3 animals. The n for physiological measurements (e.g., amplitude and latency), qPCR studies, and ultrastructural observations of type I SGNs (e.g., compactness of myelin and g ratio measurements) were based on prior studies^{74,81}. For microarray studies, prior analyses of injured mouse AN demonstrated that sample size n = 3 were sufficient for robust detection of differentially expressed genes while maintaining acceptable (i.e., moderate to low) false discovery rates (FDRs)⁷⁴. The n for each experiment will be indicated in the results or figure legend. Representative images from each experimental group for each confocal or TEM study are shown in the figures. Distribution of the data was tested using either Shapiro-Wilk or Kolmogorov-Smirnov Tests for normality. The appropriate parametric or non-parametric tests were then used. Statistical software and packages used in this project include DeSeq2⁸², dChip⁸³, Microsoft Excel, R (R project⁸⁴; version 3.5.2) or GraphPad Prism 7 (GraphPad Software, Inc., La Jolla, CA).

Table 2.4.1: Antibodies used

Primary Antibody	Host	Company	Catalog No.	Concentration
Anti-Cntn1	Polyclonal goat IgG	R&D Systems (Minneapolis, MN)	AF904	1:200
Anti-Iba-1	Rabbit	Wako (Osaka, Japan)	019-19741	1:100
Anti-NF200	Monoclonal mouse IgG1	Sigma-Aldrich (St. Louis, MO)	N0142	1:200
Anti-NrCAM	Polyclonal rabbit IgG	Abcam (Cambridge, MA)	ab24344	1:200
Anti-Pan-QKI clone N147/6	Monoclonal mouse IgG1	UC Davis/NIH NeuroMab Facility (Davis, CA)	75-168	1:200
Anti-QKI-5	Polyclonal rabbit IgG	Bethyl Laboratories (Montgomery, TX)	A300-183A	1:200
Anti-QKI-6 clone N182/17	Monoclonal mouse IgG1	UC Davis/NIH NeuroMab Facility (Davis, CA)	75-190	1:100
Anti-QKI-7 clone N183/15	Monoclonal mouse IgG1	UC Davis/NIH NeuroMab Facility (Davis, CA)	75-200	1:100
Anti-Sox10	Polyclonal Goat IgG	Santa Cruz Biotechnology (Dallas, TX)	sc-17342	1:100
Anti-Sox2	Polyclonal Goat IgG	Santa Cruz Biotechnology (Dallas, TX)	sc-17320	1:100
Anti-Calb2 (Calretenin)	Goat	Swant (Switzerland)	CG1	1:1000
Anti-MBP	Polyclonal chicken	EMD Millipore (Burlington, MA)	AB9348	1:100
Anti-Nav1.6	Polyclonal rabbit	Alomone Labs (Israel)	ASC-009	1:100
Anti-Calb1	Polyclonal rabbit	Cell Signaling (Danvers, MA)	13176S	1:100

Secondary Antibody	Host	Company	Catalog No.	Concentration
Anti-Goat Alexa Fluor® 488	Polyclonal donkey IgG (H+L)	Thermo Fisher Scientific (Waltham, MA)	A-11055	1:500
Anti-Rabbit Alexa Fluor® 568	Polyclonal donkey IgG (H+L)	Thermo Fisher Scientific (Waltham, MA)	A-11011	1:500
Anti-Rat Alexa Fluor® 488	Polyclonal donkey IgG (H+L)	Thermo Fisher Scientific (Waltham, MA)	A-21208	1:500
Biotinylated Anti-Goat IgG	Horse	Vector Laboratories (Burlingame, CA)	BA-9500	1:100
Biotinylated Anti-Rabbit IgG	Horse	Vector Laboratories (Burlingame, CA)	BA-1100	1:100
Biotinylated Anti-Mouse IgG	Goat	Vector Laboratories (Burlingame, CA)	BA-9200	1:100
Biotinylated Anti-Chicken IgG	Goat	Vector Laboratories (Burlingame, CA)	BA-9010	1:100
Anti-Biotin Dyes	Host	Company	Catalog No.	Concentration
Fluorescein Avidin DCS	N/A	Vector Laboratories (Burlingame, CA)	A-2011	1:100
Texas Red® Avidin D	N/A	Vector Laboratories (Burlingame, CA)	A-2006	1:100
AMCA Avidin D	N/A	Vector Laboratories (Burlingame, CA)	A-2008	1:100

Chapter 3: Myelination and nodal assembly in normal auditory nerve development

3.1 Introduction

Proper passage of electrical impulses and regulation conduction velocity through the AN are necessary for the effectual, precise function of auditory system. Apart from the contribution of properly mechanotransducing hair cells and maintenance of healthy endocochlear potential by the stria vascularis, complete myelination of type I SGNs by SCs and SGCs along with intact formation of the unmyelinated nodes of Ranvier along the fibers. Canonical nodal structures, which contain clustering molecules binding to voltage-gated ion channels (VGICs) responsible for the regeneration of action potentials necessary for their saltatory conduction throughout successive nodes of Ranvier, are essential for the transmission of stimuli. They are fundamental structures in myelinate fibers and because their importance for conduction is fact. Studies involving the nodes of Ranvier in the peripheral AN have been somewhat scarce, until recently. In the developing mouse AN, the contribution of the nodes of Ranvier to the onset of hearing and subsequent maintenance of auditory function remain to be fully elucidated.

Development of the nodes of Ranvier have been previously studied extensively in other systems, including the sciatic, brainstem, and optic nerve. Multiple interdependent mechanisms of nodal assembly have been found for the peripheral nervous system. In short, axonal cellular adhesion molecules (CAMs)

Neurofascin 186 (Nfasc 186) and neuronal-CAM (NrCAM) located at the edge of early enwrapping SC processes interact with gliomedin, a transmembrane protein located at SC microvilli^{36,37}. Together, these molecules work to cluster VGSCs that initially form as heminodes at the bilateral terminal edges of SC processes. The CAMs also bind other structural proteins at the node, such as anchoring protein Ankyrin G (AnkG) and scaffolding protein BIV-spectrin, which help secure the VGICs at the nodal axolemma and buttress the clusters respectively^{39,40}. Eventually, the heminodes fuse to form an axonal node of Ranvier. In conjunction with nodal formation, transmembrane proteins at the axolemma adjacent to the heminode act as axo-glia connecting proteins to attach the terminating myelin loops of the SC to the axolemma to form classic paranodal loops, which may act as physical barriers to contain nodal proteins within the node of Ranvier^{36,42}.

While there is a wealth of information about nodal formation in other nervous systems, nodal studies in the peripheral AN is still in its infancy. A recent paper by Kim and Rutherford has shed light on placement and maturation of voltage-gated ion channels important for saltatory conduction in the axon initial segments and axonal nodes of the cochlea and their importance for the onset of hearing⁵⁰. Further characterization of the structural formation of the nodes of Ranvier and the paranodal segments assembled by SCs at the axons and SGCs of the SGN somata are still necessary. In this chapter, we characterize the three types of nodal structures present in the AN – heminode, axonal node, and ganglion node – and their common and distinctive properties. We then show that

structural and molecular development and maturation of nodal structures, in parallel with myelination of the AN fibers, are important contributors to the onset of hearing and maturation of AN function. We also further emphasize their functional importance by highlighting nodal structural abnormalities present in the early AN development of an animal model of profound hearing loss.

3.2 Specific methods

3.2.1 Animals used

CBA/CAJ pups aged P3, 7, 14 and 21 were used for the RNA-seq and RT-qPCR analyses. The aforementioned age groups, with the addition of P10 and 1 month-old mice were used for histological analyses, including TEM and node length measurements. Pups aged P12 were included in the ABR thresholds measurements. Dmdo/Dmdo and +/+ WT control pups aged P14 were used for the heminodal clustering comparisons.

3.2.2. Developmental RNA-seq analyses of node-related genes

Normalized, log2 transformed RNA-seq datasets acquired from the FASTq files via DeSeq2⁸² from P3, 7, 14, and 21 mice were used. A list of node-related genes were compiled using literature^{39,42} and AmiGO⁸⁵ using the terms “node of Ranvier,” “paranode region of axon,” “paranodal junction assembly,” “juxtaparanode,” and “internode.” A pairwise comparison of the expression of the node-related genes between the age groups of the RNA-seq datasets were

performed using dCHIP⁸³. Significant differential expression was defined as $p < 0.05$ (Student's t-test, unpaired, 2-tailed) for at least one pairwise relationship among the different postnatal time points. The FDR after 1000 permutations was found to be 12.8%.

3.2.3 RT-qPCR

Total RNA was extracted from the ANs from postnatal CBA/CaJ pups at each designated time point. cDNA was produced from the total RNA samples amounting to 50ng each via reverse transcription using the QuantiTect Reverse Transcription Kit (Qiagen) and according to the manufacturer's protocol. The resulting cDNA products were then assayed for expression of our genes of interest and the 18s reference gene via TaqMan probes (Applied Biosystems) using a Lightcycler 480 (Roche Diagnostics). Relative expression was calculated via the standard curve/ $\Delta\Delta$ CT method and normalized with the 18s reference gene.

3.3 Results

3.3.1 Expression profiles of genes composing nodal structural domains exhibit temporal clustering and the onset of node formation in the mouse auditory nerve

In order to characterize nodal assembly in the mouse AN, we first looked at the expression profiles of node related genes in critical developmental time

points with relation to myelination and hearing onset. Previous TEM studies done in the Lang Lab show that myelination of the type I SGNs starts at around P3 and that peak myelination activity occurs at around P7. Literature showed that in mice, the onset of hearing occurs at P10-12⁸⁶, and that further maturation of AN function occurs after the ear canal opens and the AN is free to respond to external sound stimulus. We therefore chose the time points P3, 7, 14, and 21 for our RNA-seq studies to encompass these critical events.

With our RNA-seq analyses, we found that 39 out of the 42 genes in our node-related gene list were significantly differentially expressed ($p < 0.05$, Student's t-test, unpaired, 2-tailed) on at least one pairwise comparison between the age groups. After hierarchical clustering analyses of the data, we found that the expression profiles of the node-related genes grouped together in 3 distinguishable temporal-based clusters (**Figure 3.3.1 A, Table 3.3.1**). Cluster 1 (P3-P7) is composed of genes important for onset of nodal formation, including genes encoding for cell-cell interaction, scaffolding, cellular adhesion and extracellular matrix molecules^{39,87-89}. Also present in Cluster 1 is *Scn2a1* which encodes the voltage gated sodium channel Nav1.2, a marker of immature nodes of Ranvier later replaced by Nav1.6 in adult nodes of Ranvier after the onset of myelination⁹⁰. Cluster 2 (P7-P21) is mainly composed of genes involved in onset of paranodal junction assembly⁹¹ and myelination⁹²⁻⁹⁷. Cluster 3 (P14-21) is comprised of genes encoding structural proteins of the electrically excitable nodal domain^{40,98,99}, and axo-glial connector proteins at the paranode^{42,100} and juxtaparanode^{45,101}. Genes encoding for voltage-gated potassium channels of the

juxtaparanode^{48,49} and the mature nodal Nav1.6 are also present. This clustering of genes indicate that in the mouse AN, the onset of node formation is around ~P3, with myelination and formation of paranodal domains occurring at around P7, and assembly of juxtaparanodes occurring at around ~P14. The up-regulation of node genes encoding structural proteins of each domain and voltage-gated ion channels may indicate that the nodal structure is prepared to function for the onset of hearing.

We validated our findings with qPCR (**Figure 3.3.1 B-F**) and found similar expression levels with the RNA-seq datasets. We validated the presence of neuronal-CAM (NrCAM) node protein (**Figure 3.3.1 G**), which is encoded by the gene *Nrcam*, encodes responsible for signaling for node formation³⁹ using immunostaining, since the gene seemed to be present a steady amount during the developmental time points as shown by the qPCR analysis. In this immunostaining analysis involving NrCAM and neuronal marker NF200, we show that NrCAM protein is present very early in the nodes of the mouse AN. The node staining as marked by NrCAM was only present in the hook area of the AN, which is the basal most point of the AN. This may indicate that nodal assembly occurs in a basal to apical gradient.

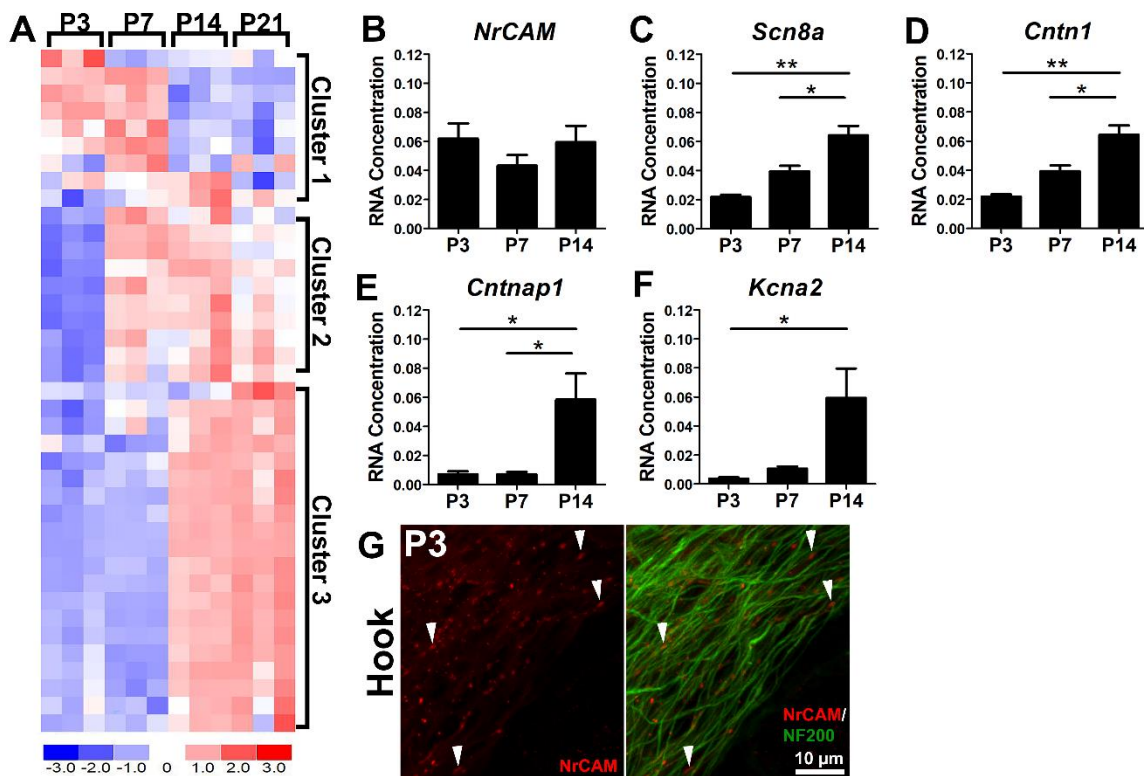


Figure 3.3.1: Expression profiles of genes composing nodal structural domains exhibit temporal clustering

(A) 39 out of 42 node-related genes were significantly differentially expressed between postnatal (P) day 3, 7, 14, and 21 ANs. Significant differential expression ($p < 0.05$, Student's t-test, unpaired) of the genes were found via pairwise comparisons between all postnatal days. The FDR for the analysis was at 12.8% (1000 permutations). In this heatmap, red indicates up-regulated gene expression, white indicates baseline gene expression, and blue indicates down-regulated gene expression. Hierarchical clustering analysis by peak expression of the genes distinguish 3 clusters (Table 1 lists genes in each cluster). (B-F) qPCR experiments validate presence of nodal (B,C), paranodal (D,E), and juxtaparanodal (F) genes in another set of P3, 7, and 14 ANs. One-way analyses of variance (ANOVAs) with Bonferroni post-test for multiple comparisons were performed to show differential expression among the different time points (* = $p < 0.05$, ** = $p < 0.01$).

Table 3.3.1: Temporal clustering of differentially expressed node-related genes

Cluster 1	Cluster 2	Cluster 3
Scn2a1	Myoc	Kcnab1
Spock1	Mag	Cntn1
Dlg1	Cd9	Nfasc
Pard3	Pmp22	Cldn5
Gnpat	Ncmmap	Kcna1
Nrcam	Sirt2	Scn1a
Cdh1	Mbp	Cntnap2
Dag1	Ugt8a	Kcna2
	Gjc2	Kcnab2
	Ermn	Scn1b
	Tubb4a	Bin1
		Dlg2
		Epb4.113
		Scn8a
		Sptbn4
		Cntn2
		Cntnap1
		Kcnq2
		Dlg4
		Sptan1

3.3.2 Hearing onset and maturation of AN function and their relation to SGN subtype differentiation

In order to bridge our molecular findings pertaining to nodal assembly to the function of the AN, we completed physiological studies by doing ABR measurements on mice aged P12 and P14 at the onset of hearing and shortly after, in P21, which is further along development, and in 1M, young-adult mice. **Figure 3.3.2 A** shows thresholds of hearing sensitivity drastically getting better from P12-14 and from P14 to P21. The thresholds from P21 and 1M are overlapping. Suprathreshold measurements tested at 11.3kHz, which represents fibers at the middle turn, are shown in **Figure 3.3.2 B-D**. Synchrony of AN firing across trials (**Figure 3.3.2 B**) between P14 and P21 are significantly higher at 80-90dB. Peak latencies are significantly shorter across all intensity levels (**Figure 3.3.2 C**). Although peak amplitudes are not significantly different between P14 and P21, the median response from the mice in the P21 group are consistently higher across levels compared to the P14 group. The P21 group response is also overall less variable compared to the P14 group. The variability in response in the P14 animals may be due to the young age of the animals and the rapid changes undergoing in the cochlea at that time.

Many events occur in the cochlea during early development, including the emergence of the endocochlear potential¹⁰², the maturation of the hair cells¹⁰³, and myelination of type I SGNs. One well-studied characteristic of the AN is the presence of 3 different subtypes of type I SGNs.

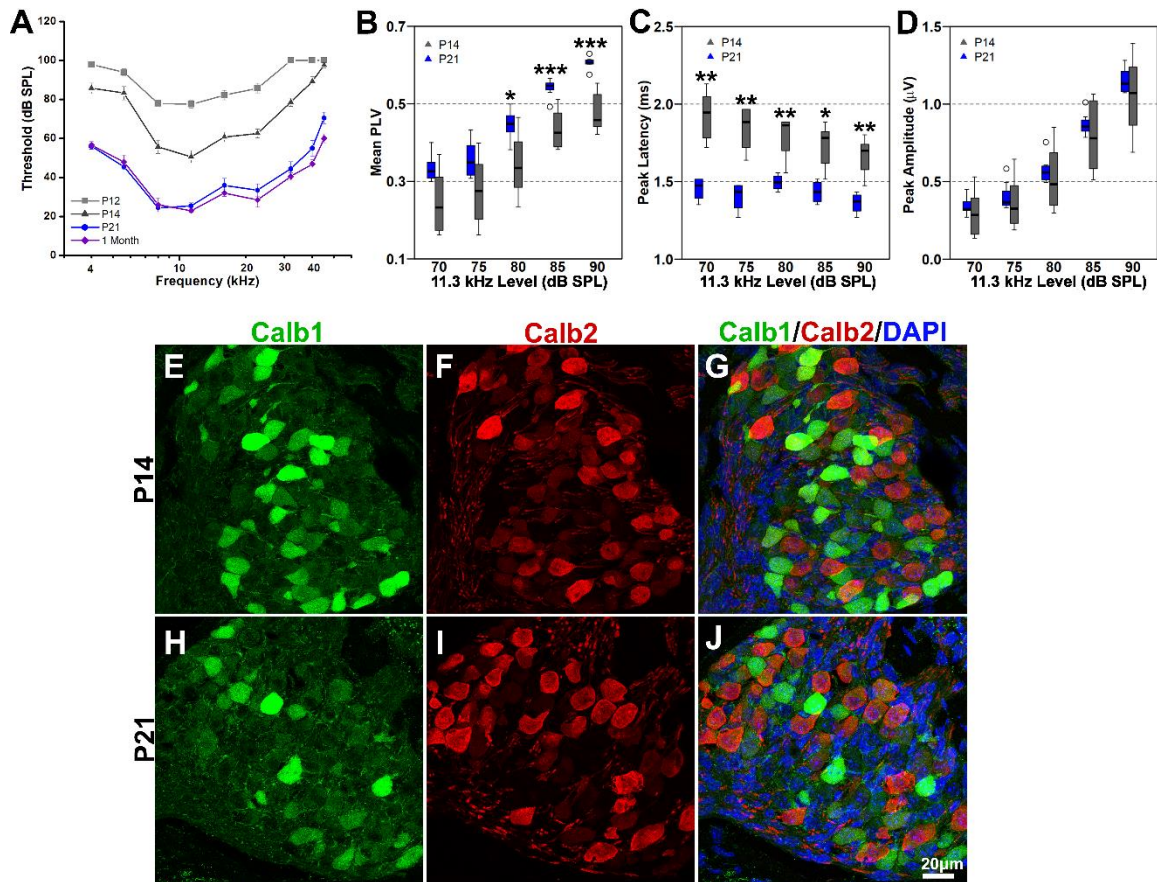


Figure 3.3.2: Hearing onset and maturation of AN function and their relation to SGN subtype differentiation

(A) Audiogram showing ABR wave I thresholds from P12, P14, P21 and 1M mice. N = 7 mice for P12 and P14; n = 5 mice for P21 and 1M. **(B-D)** shows suprathreshold measurements of ABR wave I from P14 and P21 mice at 11.3kHz. **(B)** Synchrony of AN firing of P21 mice are significantly better than in P14 mice for 80-90dB SPL (Mann-Whitney U Test, n = 8 mice/group). **(C)** Peak latencies are shorter across all shown levels (Mann-Whitney U Test, n = 8 mice for P14, n = 4 mice for P21). **(D)** Peak amplitudes are slightly higher in P21 animals, but are not significantly different compared to P14 mice (Mann-Whitney U Test, n = 8 mice/group). **E-J** show representative images of different type I SGN subtypes in P14 **(E-G)** versus P21 mice **(H-J)** as marked by Calb1 **(E,H)** and Calb2 **(F,I)**. The merged images with nuclear counterstain DAPI are shown in **G,J**. For the non-parametric Mann-Whitney u tests, * = p<0.05, ** = p<0.01, *** = p<0.001.

The physiological characterization of these subtypes were completed long ago in cats¹⁰⁴ and in gerbils⁹. It was not until recently that molecular markers for the 3 subtypes were found and that it was revealed that differentiation of the subtypes occurred in between the first and third postnatal weeks¹⁰⁵⁻¹⁰⁷, and that maturation of the subtypes were dependent their expression of their characteristic molecular marker. High SR fibers are marked by Calb2, mid SR fibers are marked by Calb1, and low SR fibers are marked by either Lypd1 or Pou4f1. In early development, the SGNs may express all these markers, while in later development, differentiated SGNs would express mainly one marker.

In our studies, we used Calb2 to mark high SR fibers and Calb1 to mark mid SR fibers (**Figure 3.3.2 E-J**). Deductive reasoning would lead us to conclude that cells negative in both Calb1 and Calb2 are most likely to be low SR fibers. In representative images taken from the middle turn of the AN from P14 and P21 mice, we show that Calb2⁺ cells, as well as Calb1⁻/Calb2⁻ cells, are greater in P21 compared to P14. This indicates that there are more high and low SR fibers in P21 mice compared to P14 mice, and that differentiation of the subtypes was occurring in between the P14 and P21 time points. The changing AN fibers post hearing onset may affect maturation of AN function and potentially other components of the AN, such as the nodal domains.

3.3.3 Assembly of nodal and paranodal proteins comprising the axonal and ganglion nodes

In most literature, the structure most commonly known as the nodes of Ranvier is usually thought of as the gap of axolemma nestled between two opposing myelin sheaths. This gap is known to be filled with voltage-gated ion channels responsible for action potential regeneration. Since we are researching the bipolar neurons of the AN in our studies, unlike the multipolar neurons popularized by textbooks, we show that these excitable nodal domains come in three different types. Two types of excitable nodal domains are the axonal nodes and the ganglion nodes. The axonal nodes can be described as the typical node of Ranvier, with the unmyelinated gap between two myelin sheaths (**Figure 3.3.3 N**). The ganglion nodes of the bipolar type I SGN flank either side of the soma. **Figure 3.3.3 O** shows one of the ganglion nodes on one side of the soma. The Cntn1-marked paranode on the SC myelinated side is clearly visible. The third excitable nodal domain is the heminode, which can be found only at the habenula underneath the IHC. The heminode will be discussed in greater detail later in the chapter.

Our immunostaining studies (**Figure 3.3.3 A-L**) in development show that heminodes are only found in the habenular region, axonal nodes are found along the axon in the peripheral side of the AN fiber at the OSL and the central side of the AN fiber at the Mod, and the ganglion nodes are found in the RC flanking the type I SGN somata. At P7, axonal nodes, as marked by NrCAM, are not yet all flanked by two paranodes, as marked by Cntn1, and the majority of ganglion

nodes do not have Cntn1 reactivity where the SC paranode should be (**Figure 3.3.3 C,D**). However, by P10, the axonal nodes have paranodal flanks, and so do the ganglion nodes (**Figure 3.3.3 G,H**). By P14, axonal and ganglion node structure are complete, coinciding with the onset of hearing and the cochlea's readiness for external sound stimulus-based responses.

We measured the axonal (**Figure 3.3.3 P-R**) and ganglion (**Figure 3.3.3 S-U**) node lengths to quantify and characterize how they change from pre-hearing onset (P7), around the time of hearing onset (P10-14), and after (1M). Our data shows that at P7, the axonal node lengths are significantly longer compared to P10 and P14 (**Figure 3.3.3 P,Q,R**). This may be due to the two opposing myelin sheaths being further away from each other. As myelination continues, the opposing myelin sheaths formed by two SCs get closer and push the nodal components in a shorter, smaller area. At P14, the axonal node gap is at its shortest for all three turns. By 1M however, the axonal nodes have significantly increased in length compared to P14. The mean node length at P14 was ~1.2-1.4 μm , while at 1M, the mean node length has increased to ~1.9 μm . For the ganglion node lengths, the length at 1M was significantly shorter than P14 in the apical turn (**Figure 3.3.3 S**). For the middle (**Figure 3.3.3 T**) and basal (**Figure 3.3.3 U**) turns, the ganglion node length in 1M were significantly shorter compared to P7, P10 and P14. Mean ganglion node lengths at P14 were ~3.6-4 μm , while for 1M, they decreased to ~2.9-3.3 μm .

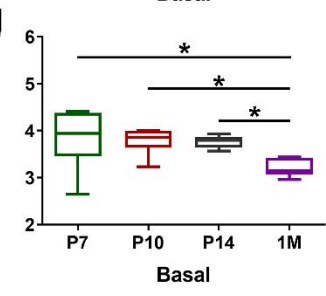
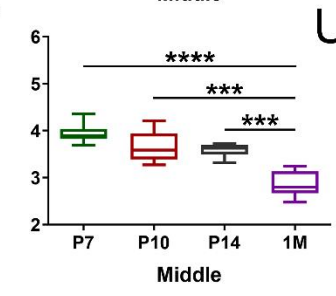
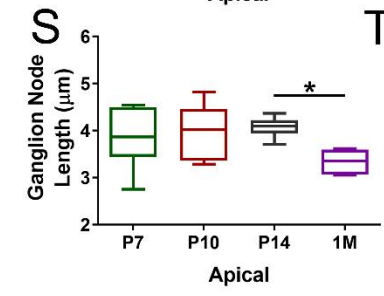
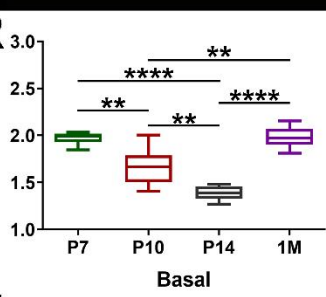
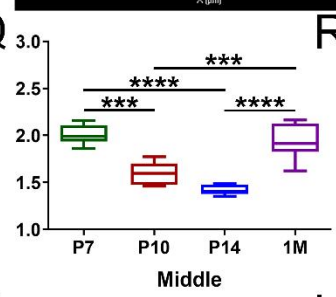
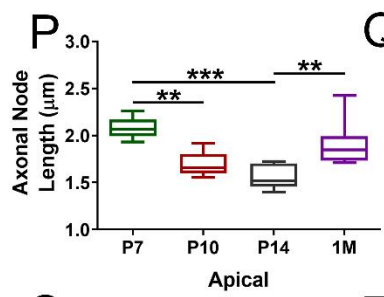
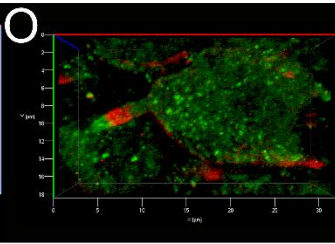
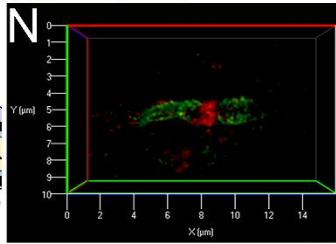
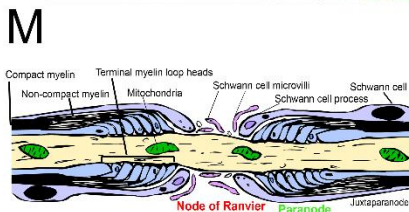
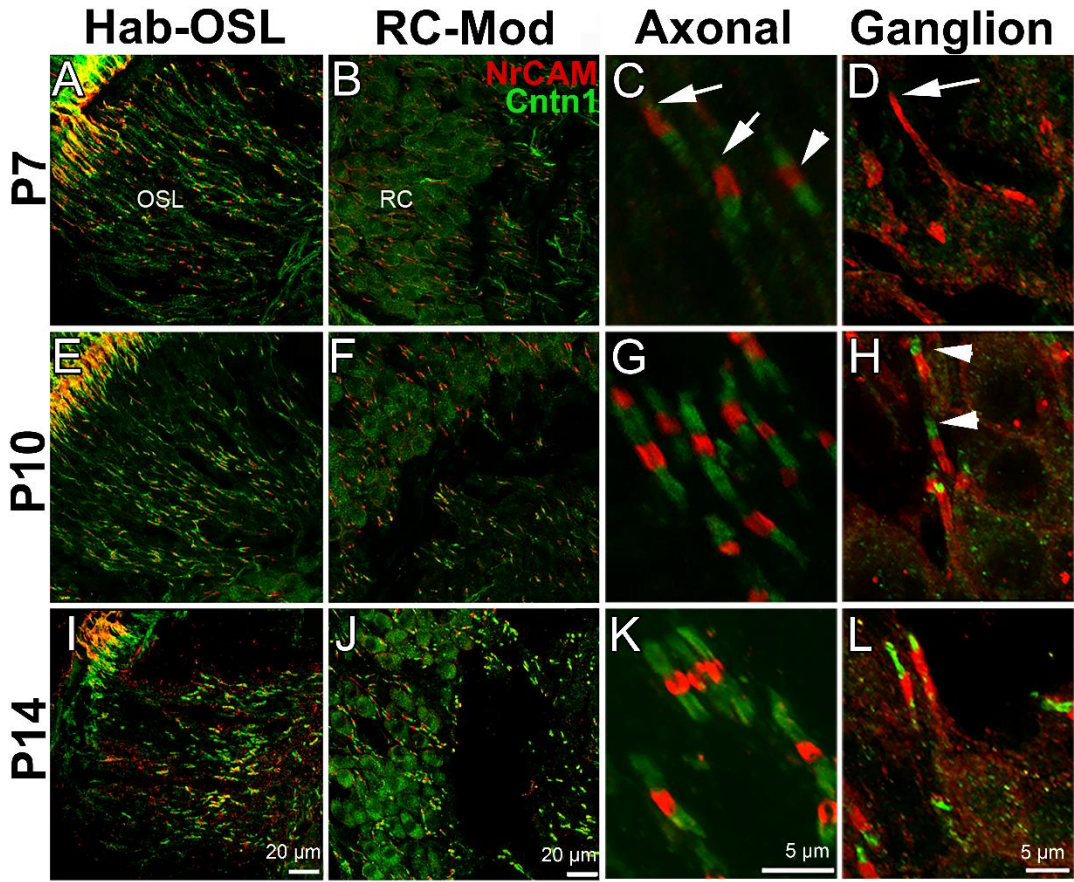


Figure 3.3.3 Assembly of nodal and paranodal proteins comprising the axonal and ganglion nodes

(A-H) The panels show assembly of the nodes, marked by NrCAM in red, and paranodes, marked by Cntn1 in green from P7, 10, and 14. **A,E,I** show the heminodes and axonal nodes where they are located at the habenula and OSL, respectively. **B,F,J** show the ganglion nodes which are located in the RC and the axonal nodes passing through the RC to the modiolus. **C,G,K** are enlargements of axonal nodes in P7 (**C**), 10 (**G**), and 14 (**K**) found in the OSL. The white arrows in **C** indicate axonal nodes with missing undeveloped paranode flanks and the white arrowhead indicates a node completely flanked by two paranodes on either side. **D,H,L** are enlargements of ganglion nodes found in the RC in P7 (**D**), 10 (**H**), and 14 (**L**). The white arrow in **D** indicates a ganglion node with no Cntn1-marked paranodal flank. The white arrowheads in **H** indicate the paranode flanks of the ganglion nodes. **M** shows a schematic of the axonal node indicating elements of the node, paranode, and juxtaparanode. **N** shows a canonical axonal node and **O** shows a canonical ganglion node in a 1 month-old mouse AN. Axonal and ganglion node measurements from P7, 10, P14, and 1M ANs are shown in **P,Q,R** and **S,T,U** respectively. The measurements are done along the three cochlear turns – apical (**P,S**), middle (**Q,T**), and basal (**R, U**). Statistical testing for significant differences between the average measurements from each time point were completed using one-way ANOVA with Tukey's multiple comparison test. N = 6 mice for groups P7, 10 and 14 and n = 7 mice for group 1M.

The change in axonal and ganglion node lengths between P14 and P21 can be explained in part by continuing maturation of myelination. This is especially true of the ganglion nodes, which have one flanking SC paranode and one flanking SGC paranode. Myelination of the somata by SGCs occurs later compared to myelination of the axonal afferents by SCs. Since recent literature and our own studies have shown that differentiation of type I SGNs into different subtypes are occurring in between P14 and P21, the molecular and structural changes may contribute to further maturation of the nodal domains leading to the axonal node lengthening and ganglion node shortening that we see.

3.3.4 Node lengths are associated with amplitude growth and decreasing latency

In order to elucidate the potential relationship between the changing node lengths and gain in amplitude between P14 and P21, we performed correlation analyses. Since the slope of the amplitude was not significantly different between the two age groups (**Figure 3.3.4 A**), we ruled out “age” as a factor contributing to the increased amplitude slopes of the animals in the P21 group compared to the animals in the P14 group. We did find that axonal nodes were significantly longer and ganglion nodes significantly shorter in the animals in the P21 group compared to those in the P14 group (**Figure 3.3.4 B,C**).

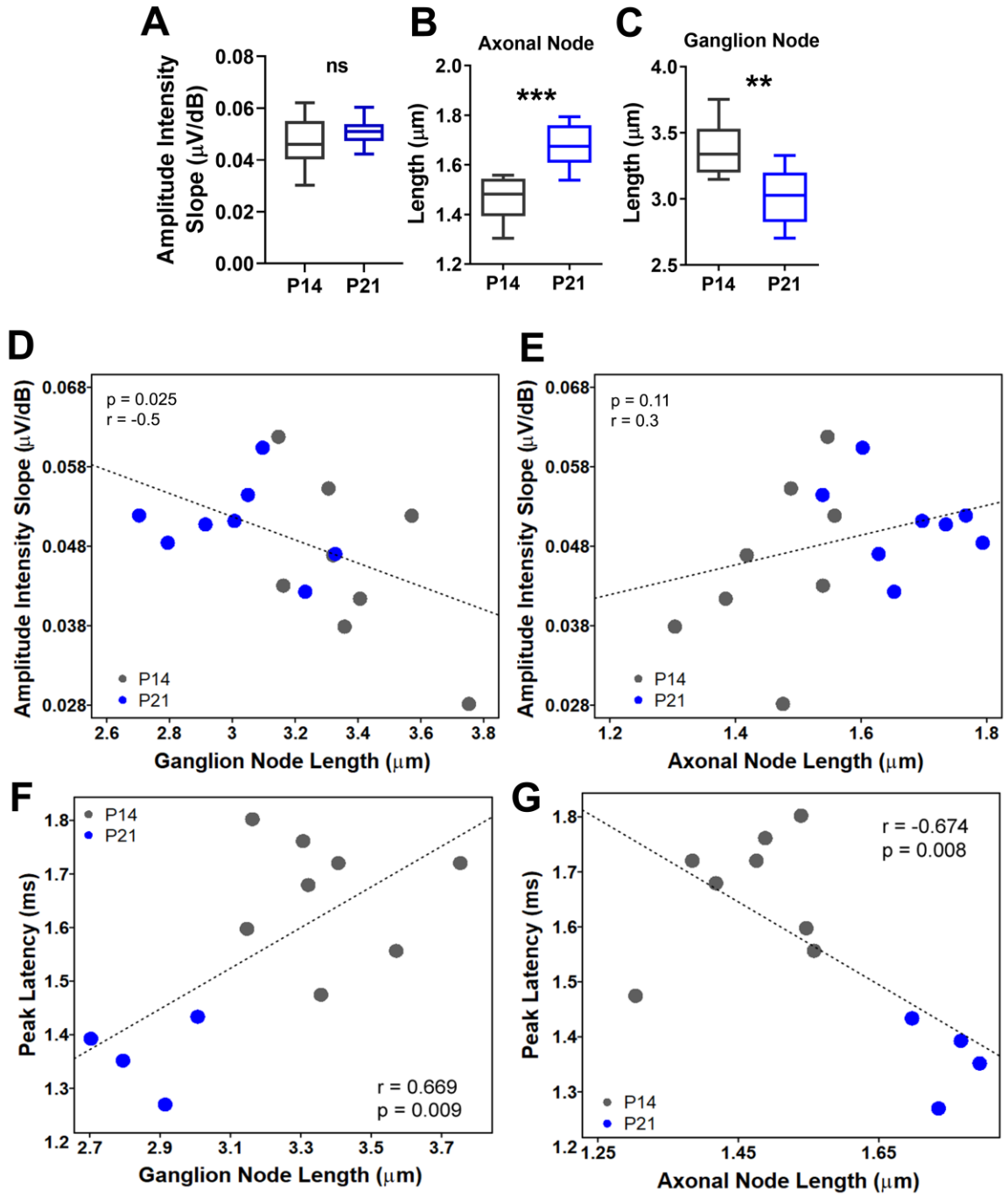


Figure 3.3.4: Node lengths are associated with amplitude growth and decreasing latency

A Shows the slope of the amplitudes from animals in the P14 group compared to those in the P21 group are not significantly different. **B** and **C** show that axonal node lengths are significantly longer and ganglion node lengths are significantly shorter for animals in the P21 group compared to those in the P14 group. **D** The correlation analysis shows that as the ganglion node lengths decrease, the slope of the amplitude increases. This association between these two variables were shown to be strong and significant, with $r = -0.5$ $p = 0.025$. **E** The correlation analysis between axonal node length and the slope of the amplitude showed that there was no significant correlation between the two variables. The correlation analyses show that ganglion node shortening (**F**) and axonal node elongating (**E**) are indicative of decreasing latencies. $N = 8$ animals/group for **A-E**; $n = 8$ animals for P14/ 4 animals for P21 for **F-G**. Mann Whitney U Test was performed in **A**. Student's t tests, unpaired, two-tailed were performed for **B** and **C**. Pearson's product-moment correlation tests, one-sided, were performed across the group data for **D-G**.

For our correlation analyses, we compared the node lengths and amplitude slopes across groups, since the relationship with the amplitude occurs independently of age. Our data in **Figure 3.3.4 D and E** show that decreasing ganglion node lengths, but not increasing axonal node lengths, are correlated with amplitude growth. To further emphasize the structure-function relationship between node lengths and AN function, we show that shorter ganglion nodes and longer axonal nodes are associated with faster conduction velocity.

We show in **Figure 3.3.2 E-J** that type I SGN differentiate into the 3 subtypes between P14 and P21 and we show here that node lengths change between P14 and P21. Although gain in amplitude across the levels tested were not significant, they were still present. We argue that the reason why the change in amplitude between the two groups were not significantly high was because the subtypes were differentiating and the node lengths were also actively changing at P14.

3.3.5 Ultrastructural assembly of axonal nodes and flanking paranodes

In order to better characterize nodal domain assembly pre-hearing onset and after hearing onset, we analyzed found and analyzed the nodal ultrastructures of the AN in P6, P10, P14, and 1M ANs.

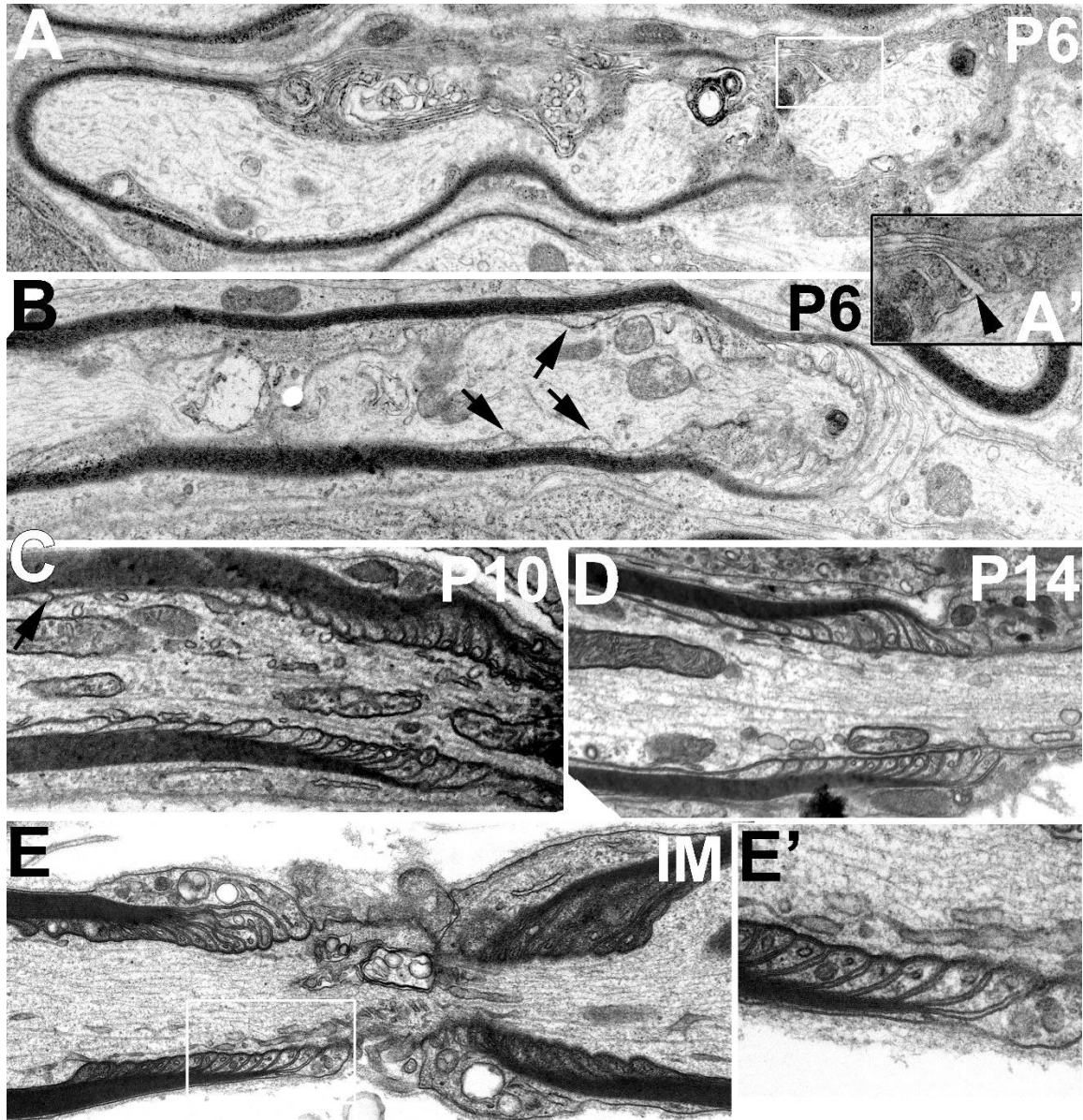


Figure 3.3.5 Ultrastructural assembly of axonal nodes and flanking paranodes

A and **B** show the nodal and one paranodal domain of a P6 AN fiber. The inset **A'** highlights the immature organization of the terminal myelin loops at connecting to the paranodal axolemma. Black arrows in **B** indicate terminal myelin loop heads connecting migrating from the internode, but not quite reaching the paranodal domain. Instead, they are currently at the juxtapanodal region, which is where the dense-compact myelin layer begins to become non-compact, transitioning to the paranodal domain. **C** shows the terminal myelin loop heads connecting to the paranode region. A few layers indicated by the black arrowhead are still in the juxtapanode region. **D** shows the terminal myelin loop heads connecting to the axolemma of the paranode similar to the organization seen in 1M as indicated in **E** and the inset in **E'**.

Axonal paranodes are created by the termination of the myelin lamellae from myelinating SCs at the paranodal axolemma. At the paranode, the terminating lamellae are seen as membrane loops filled with cytoplasm. This loop provides a larger surface area for axo-glial connections and glial-glial connections between the adjoining lamellae and terminal loops. We show that the myelin loop layers in P6 are still migrating to the paranodal domain from the internodal region (**Figure 3.3.5 A,B**). The terminal loops are still spaced far apart as shown in **Figure 3.3.5 A'**. In a canonical paranodal region, such as the one shown in **Figure 3.3.5 E**, the terminal myelin loop heads are connected to the paranodal axolemma and are juxtaposed closely together with no gaps. The terminal myelin loops and their axo-glial connection separate act as physical barriers to separate the VGSCs in the node from the VGKCs in the juxtaparanode^{41,42,49}. This axo-glial connection is accomplished by proteins such as Cntn1. We show previously in **Figure 3.3.3 G** that the axo-glial protein Cntn1 was fully present in both flanking axonal paranodes by P10. However, as we show in **Figure 3.3.5 C**, the ultrastructural connection at the paranode may not be fully complete. We show in **Figure 3.3.1 A** that gene encoding axo-glial connector proteins and structural supports are upregulated at P14. By P14, as shown in **Figure 3.3.5 D**, we found that organization of the terminal myelin loop heads were similar to that of the 1M animals.

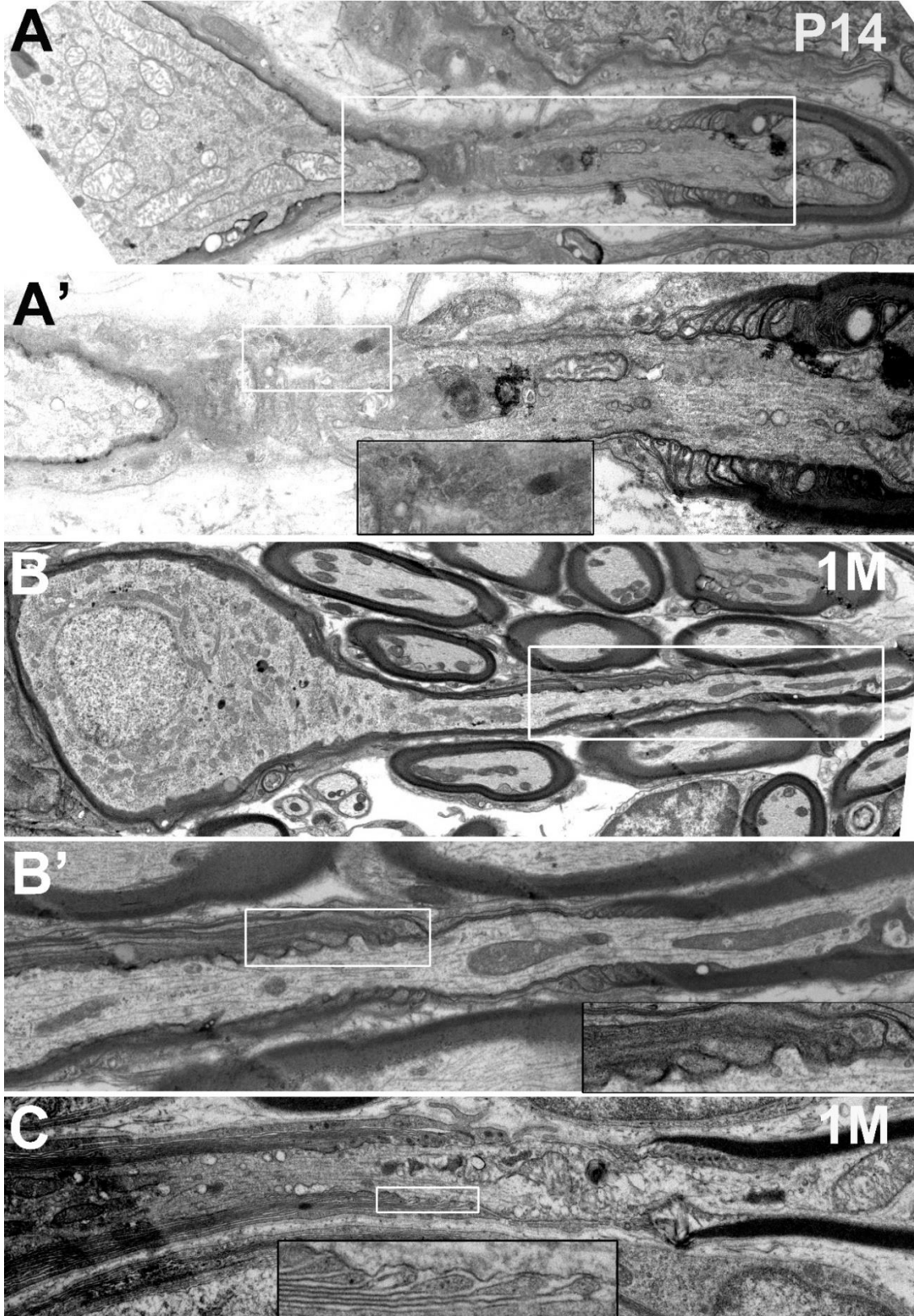


Figure 3.3.6: Ultrastructural assembly of ganglion nodes and satellite cell paranodes

A shows a ganglion node at P14, with an enlargement of the image shown in **A'**. The inset in **A'** shows few terminal myelin loop layers of the SGC lamellae connecting the SGC paranodal region. Axo-glia connections between the SGC lamellae and the SGC paranodal axolemma at P14 are neither distinct nor do the terminal loops solidly attach to the axolemma. **B** and **C** show ganglion nodes in 1M AN fibers. Each panel includes an inset highlighting a magnification of the boxed region of interest. The insets in **B'** and **C** highlight the connections of several SGC terminal myelin loops with the SGC paranodal axolemma.

3.3.6 Ultrastructural assembly of ganglion nodes and satellite cell paranodes

While the paranodal flank myelinated by SCs show clear organization and connection of the terminal myelin loops at the SC paranodal axolemma, the paranodal region myelinated by an SGC still show incomplete attachment of the SGC lamellae at the paranodal axolemma of the P14 ganglion node (**Figure 3.3.6 A, A'**). The SGC lamellae are very few and are loosely, if at all, attached to the axolemma (see enlarged region of interest in **Figure 3.3.6 A'**). In mature SGC ganglion nodal structures, as shown in **Figure 3.3.6 B,C**, the terminal myelin loop layers of both SGC and SC myelin are connected to the paranodal axolemma. The number of SGC lamellae have increased and the terminal myelin loops show distinct connection to the paranodal axolemma (see enlarged region of interest in **Figure 3.3.6 B'**).

Regardless of age of the AN, these ultrastructural studies also show the clear difference between SGC myelination of the soma/ganglion paranode and SC myelination of the axon. The myelin lamellae surrounding the soma and terminating at the ganglion paranode are less compared to SC lamellae. The terminal myelin loop heads, though connected to the axolemma, have much space in between the loops and layers, indicating that glial-glial connection of the SGC lamellae are less strong compared to SC lamellae. The incompleteness of the SGC paranodal structure by P14 compared to the completeness of the SC paranodal structure at the same age indicate that maturation of the SGC myelination occurs later compared to SC myelination and may also be related to SGN subtype differentiation.

3.3.7 Completion of heminodal clustering under inner hair cells is temporally dependent

The heminodes, also known as the axon initial segment of the type I SGNs, are the site of action potential generation for the AN fibers. The peripheral afferents begin to unmyelinate at the habenula in order to pass through the habenula perforata and connect to the IHCs. Towards the OSL side, the fibers are myelinated by SCs, and the heminodes therefore only have one paranodal flank. We show that in the AN turns pre-P14, the components of the heminodes, as marked by NrCAM and Nav1.6, are still travelling towards the habenula. In the basal turn at P7 (**Figure 3.3.7 A''**), this is less apparent, as more heminodes have clustered underneath the IHCs. Still, several heminodes are visibly approaching from the OSL region in the basal turn, but even fewer so in the P10 basal turn (**Figure 3.3.7 B''**). The number of heminodes approaching the habenula from the OSL are even more apparent in the middle turn at P7-P10 (**Figure 3.3.7 A',B'**) and in the apical turn at P7-P14 (**Figure 3.3.7 A,B,C**). By P14, we determined that clustering of heminodes underneath IHCs is mostly complete in the basal and middle turns, and in 1M, young-adult ANs, heminodal clustering is complete in all turns (**Figure 3.3.7 D,D',D''**). These observations support our idea that the completion of heminode migration and clustering underneath the IHCs are progressing from a basal to apical gradient.

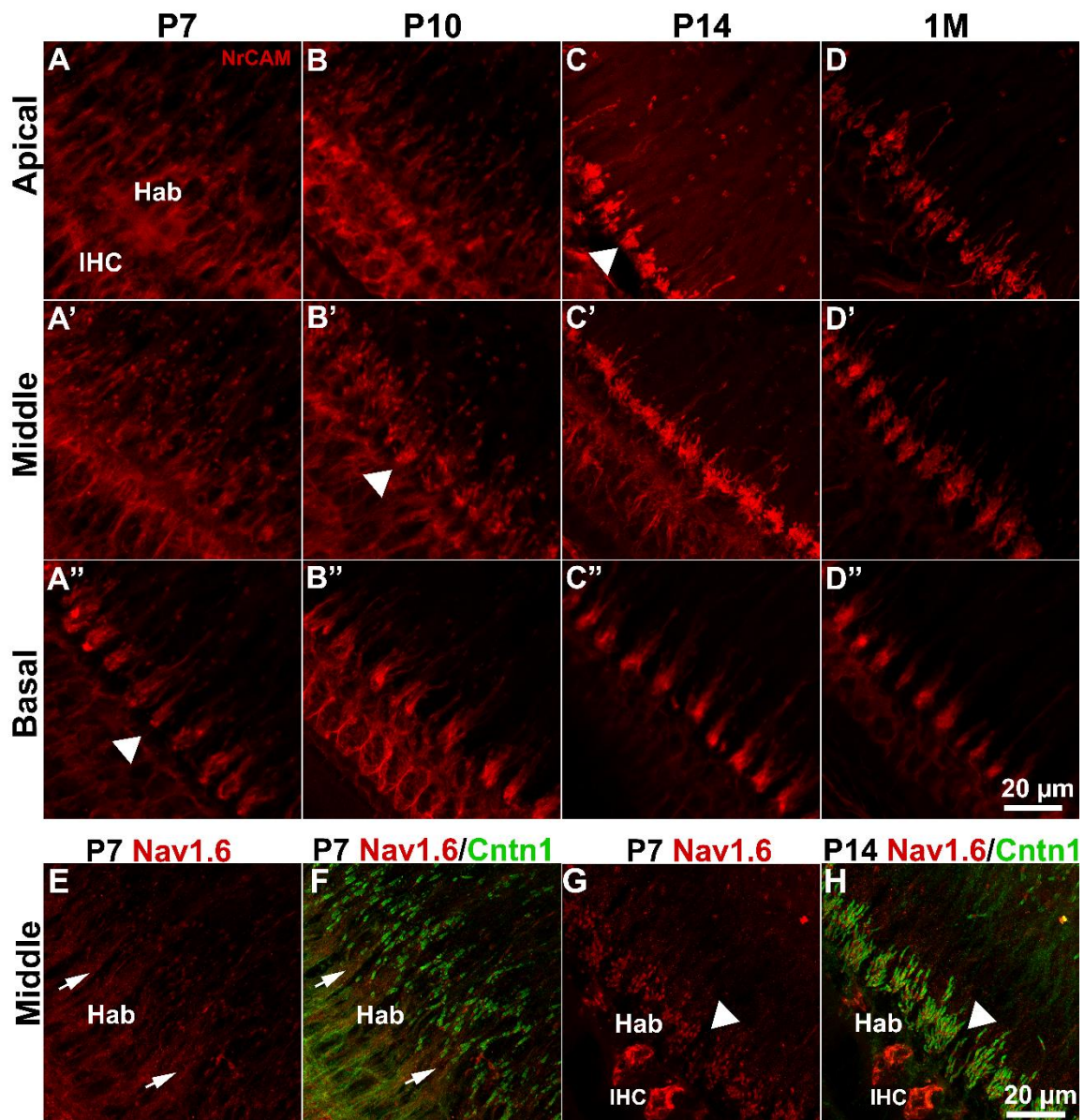


Figure 3.3.7: Completion of heminodal clustering under inner hair cells is temporally dependent.

Heminodal clustering indicated by NrCAM are shown horizontally across time points and vertically across AN location from apical, middle, and basal (A-D''). Arrowhead in C-C'' shows that clustering of the heminodes underneath the IHCs at the habenula are complete in all turns by P14 similar to that seen in 1M. Heminodal clustering of Nav1.6 is complete in the middle turn by P14 compared to P7 (E-H).

We show the flanking Cntn1 paranode to visualize the movement of myelination and the pushing of nodal components towards the habenula in **Figure 3.3.7 F**. We show that the heminode clustering is complete in the middle turn by P14, since the clusters are right under the IHCs, and they are spaced much farther apart across the OSL from the first axonal nodes which are clearly marked by two flanking paranodes (**Figure 3.3.7 H**).

3.3.8 Disorganization of the heminodes in a model of profound hearing loss

The homozygous Dmdo/Dmdo mice have an ENU-induced point mutation causing immature stereocilia and hair cell formation leading to profound deafness at birth^{70,71}. WT mice have normal hearing comparable to CBA/CaJ, mice while Dmdo/Dmdo littermates have no hearing sensitivity at P14 (Lang Lab, unpublished data). In this mouse model, the mutation causes the HCs to be perpetually immature throughout early development and degenerate in later development due to lack of activity. With this lack of activity, we hypothesized that since myelination and, to an extent, nodal formation may be driven by in spontaneously electrically active hair cells pre-hearing onset, nodal assembly may be inhibited or impaired in the Diminuendo mutant model. We show here that though we found no significant differences in the axonal and ganglion nodes, there is clear disorganization of the heminodal clusters in the Dmdo/Dmdo ANs compared to the WTs, especially in the apical and middle turns.

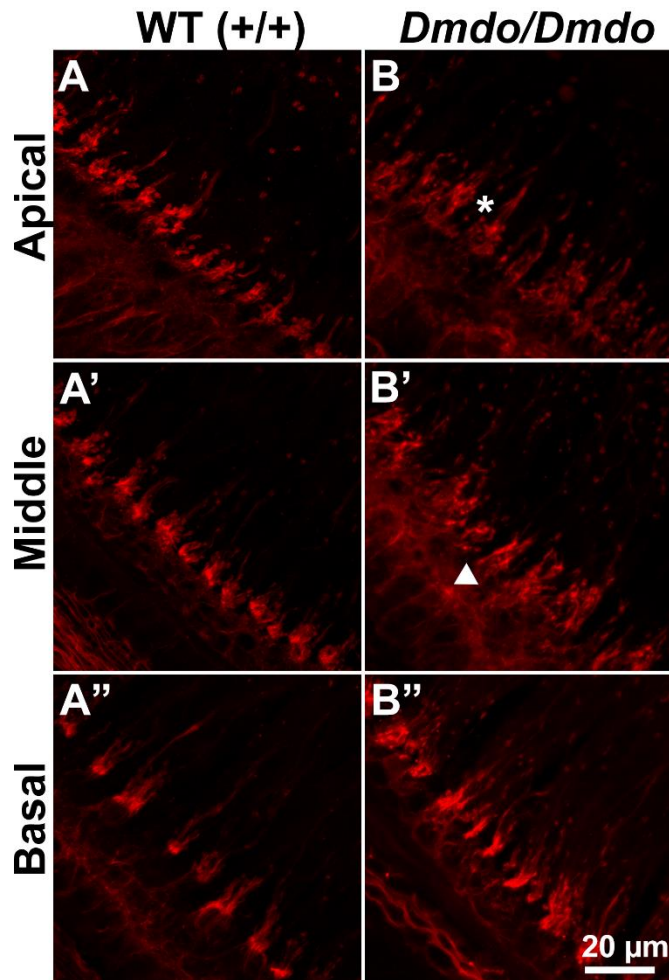


Figure 3.3.8: Disorganization of the heminodes in a model of profound hearing loss

Heminodes as marked by NrCAM in P14 wildtype (+/+) and homozygous Diminuendo (*Dmdo/Dmdo*) cochlear sections. Notice the compactness of heminode clusters at the habenulae in all cochlear turns of the WT sections, **A**, **A'**, **A''**. Asterisk and arrowhead denote the less condensed and more disorganized heminodal clusters in the apical **B** and middle **B'** turns of the *Dmdo/Dmdo* ANs.

The heminodes are further out from the habenula and are spread closer towards the OSL. Our findings suggest that lack of auditory input from IHCs may affect heminodal clustering.

3.4 Discussion

With these studies, we present three major findings pertaining to the mouse AN. First, we pioneered the characterization of the three different types of excitable nodal domains in the mouse AN type I SGNs. Then, we showed that SC and SGC myelination of type I SGNs is morphologically different from each other and that SGC myelination is slower compared to SC myelination. Lastly, we showed a significant structure function relationship between the nodal structures and AN function, with longer axonal nodes being associated shortening latencies and shorter ganglion nodes being associated with both shortening latencies and amplitude growth.

Most of the research on nodal domains in the PNS are usually conducted in the sciatic nerve due to ease of access/manipulation and because of its relatively straight layout (at least when compared to the spiral-shaped AN). Even now, there are only a small number of articles involving the nodes in the AN. In this chapter, we characterized the three nodes molecularly and ultrastructurally. Clustering of node-related gene expression showed up-regulation of these clustered genes in a time-dependent manner, indicating three main time points pertaining to the nodal structure: 1) onset of formation, 2) complete assembly of structural molecules, and 3) further maturation. Genes responsible for initiation of the excitable nodal domain

formation were found to be up-regulated at P3. Genes responsible for myelination and initiation of paranode formation were found to be up-regulated at P7. Genes encoding structural proteins of each nodal domain and the voltage-gated ion channels were up-regulated at P14, which coincides with the onset of hearing. In accordance to the transcriptomic data, we argue that molecular assembly of the nodes and paranodes were complete by the onset of hearing at around P14 via immunostaining of key structural and functional proteins, nodal NrCAM, paranodal Cntn1, and the functional Nav1.6. We show that NrCAM is present in the basal hook area as early as P3, which supports its importance as an initiator of nodal formation. Multiple studies have shown this CAM to be essential for the initial VGSC clustering at in the forming nodes and for maintenance and restriction of the VGSC clustering at the nodes³⁶⁻³⁹. We also highlight the temporal-dependent expression of axo-glial connector Cntn1 at each type of ganglion paranode, with Cntn1 present in all ganglion paranodes by P14. We conclude that the completion of nodal assembly parallels the onset of hearing.

We show that maturation of the nodal structures after the onset of hearing was possible through our measurements of the axonal and ganglion node lengths. For the axonal nodes, we found that axonal node lengths shortened towards hearing onset (from P7 to P14) and increased again between P14 to P21/1M. The shortening axonal nodes pre-hearing onset may be due to SC myelin still forming. We concluded this through our axonal node ultrastructural data which showed the dense, compact organization of the myelin lamellae throughout the internodes and terminal myelin loop heads strictly at the paranodal region of SC paranodes by

P14. The lengthening of the axonal nodes post hearing onset is in parallel with functional maturation. Lengthening of the axonal nodes may be due to clustering of additional voltage-gated ion channels in the node. The one other paper that focused on the nodal domains was the 2016 article by Kim and Rutherford⁵⁰, in which they characterized various VGSC and VGKC protein expression profiles via immunostaining in rat ANs around the onset of hearing. They revealed valuable information, especially pertaining to the clustering of low-voltage Kv1.1 VGKCs at the juxtaparanodes, which occurred starting at the time of hearing onset. They also showed the additional expression of certain VGKCs in specific nodal domains, including the excitable heminodes and nodes, after hearing onset. These findings corroborate our own conclusions that even after molecular and structural assembly of the nodal domains at P14 around the onset of hearing, maturation of the nodal structures continue to occur.

The lengthening of axonal nodes post hearing onset may also be due to the differentiation of the type I SGNs into the three subtypes which they have shown to occur approximately between P14 and P21^{105–107}, as we have also validated in this chapter. Single neuron studies from cats¹⁰⁸, gerbils⁹, and mice¹⁰⁹ show that SGN subtypes have distinct morphologies associated with their functional properties. Mainly, high SR/low threshold fibers have larger axon diameters compared to low SR/high threshold fibers, which have smaller diameters. Since axon diameter is related to thickness of myelination, high SR fibers may be more myelinated and low SR fibers may be less myelinated. Aside from the lengthening of the axonal nodes, we also show that the range of axonal

node lengths from min to max is much more variable in P21/1M compared to P14. This finding may indicate the presence of the different subtypes, with high SR axonal nodes possibly on the shorter end, and low SR axonal nodes possibly on the longer end of the length spectrum. To further study this idea, we would have to measure the nodes from the different subtypes to determine if each subtype is associated with a certain axonal node length.

In this chapter, we also showed the differing myelin morphologies of the SGC compared to the SC. We found that SGC myelination of the SGN cell body, although multi-layered, is less dense and especially less compact, as we show through our ultrastructural studies of SGC paranodes. SGC myelination is slower than SC myelination, since terminal myelin loop heads are fewer and are not strongly connected to the axolemma in P14 SGC paranodes. By 1M, even though there are more SGC terminal myelin loop heads that are strongly connected to the axolemma, the glial-glia connections between the loop heads are not as tight when compared to the connection between SC loop heads at either P14 or 1M. We show that ganglion nodes lengths decrease between hearing onset (P14) and hearing maturation (P21). The decreasing lengths between P14 and P21 may be due to the continuing SGC myelination. Not much is known about the function of SGCs, especially in the AN, but they are thought to play a role in supporting neuronal metabolism due to the presence of amino acid, nucleobase, and fatty-acid transporters on their surfaces¹¹⁰. SGCs myelinating cell bodies of other nerves are more commonly reviewed in the aspect of neuropathic pain^{111,112}. In the trigeminal nerve, the inhibition of Kir4.1 expression on the SGCs are shown to cause

dysfunction in potassium buffering, which leads to pain-like behavior in the mutant mice¹¹³. A recent study of the SGCs myelinating the dorsal root ganglia show that fractalkines resulting from induced inflammation target SGCs, which then produce inflammatory factors that are associated with hypernociception¹¹⁴. In the AN, we are able to show that SGC myelin/paranode morphology is different compared to SC myelin/paranode, but we are not absolutely certain of the functional significance of that differing morphology. At present, there are no studies querying pain associated with SGCs in the AN. We do show that a change in ganglion node length, but not axonal node length, is associated with amplitude growth. Perhaps in the AN, myelination of the SGN by SGCs is necessary for ease of depolarization of the large cell body.

Previous studies have shown that mice showing nodal abnormalities also have decreased hearing sensitivity. High intensity noise-injury was shown to lead to disruption of the axonal paranodes⁵¹ and transient ablation of glial cells was shown to lead to disruption of heminodal clustering¹⁴. The link between formation/maturation of normal nodal structures, especially that of the ganglion nodes, and proper AN function had yet to be studied. Here we showed that maturation of nodal structures after hearing onset (i.e., shortening of ganglion nodes, and elongation of axonal nodes), are associated with decreasing AN firing latencies. We also show that decreasing ganglion node lengths are correlated with increasing amplitude slopes. Our studies with the *Dmdo/Dmdo* mice also support the findings that proper heminodal clustering is important for normal AN function. With these findings, we determined that normal nodal formation/maturation

contributes to the enhancement of AN function between hearing onset and hearing maturation.

†Chapter 4: Glial dysfunction after noise injury leads to dysmyelination and loss of hearing function

†The following chapter includes data modified from an article we published in the Journal of Neuroscience on March 7, 2018.

The following are the list of authors, their affiliations and their contributions: Clarisse H. Panganiban^{1*}, Jeremy L. Barth^{2*}, Lama Darbelli^{3*}, Yazhi Xing^{1,4}, Jianning Zhang¹, Hui Li¹, Kenyaria V. Noble¹, Ting Liu¹, LaShardai N. Brown¹, Bradley A. Schulte¹, Stéphane Richard³, Hainan Lang¹

*** *These authors contributed equally.***

Affiliations: ¹Department of Pathology and Laboratory Medicine, MUSC;

²Department of Regenerative Medicine; ³Lady Davis Institute for Medical Research, Sir Mortimer B. Davis Jewish General Hospital, McGill University;

⁴Shanghai Jiao Tong University Affiliated Shanghai Sixth's People's Hospital

Author contributions: C.H.P., J.L.B., L.D. and H.L. designed research; C.H.P., L.D., J.L.B., H.L., Y.X., J. Z. and H.L. (Hui Li) performed research; L.D. and S.R. provided unpublished reagents and mouse model; H.L., Y.X., C.H.P., T.L., K.V.N., B.A.S., L.N.B. and J.L.B. analyzed data; H.L., C.H.P. and J.L.B. wrote the paper.

4.1 Introduction

After characterizing the different nodal types in the AN and highlighting the importance of proper myelination and nodal development/maturation in association with AN functional maturation, we wanted to next elucidate the relationship between noise injury and myelination. Studying myelin and the affiliated nodal structure maintenance, especially at the paranodal domain, as well as glial-related molecules, can be used to interpret glial cell function.

Hearing loss due to noise-injury has been a long-studied topic, with permanent threshold shifts (PTS) being apparent with high intensity noise exposure (≥ 106 dB). Studies by Liberman and Kujawa show that lower intensity

noise exposure may result in temporary threshold shifts but with loss of synaptic connection between the IHCs and AN afferent fibers causing suprathreshold response deficits¹³. Aside from synapse loss, many researchers attribute the cause of noise-induced hearing loss to death of hair cells^{115–117}, degeneration of lateral wall^{118,119}, and loss of AN neurons^{120–122}. One component of the cochlea, the auditory glial cells, have not been so well-studied in the post-noise setting.

About 95% of AN fibers are myelinated by cochlear glia, i.e., the SCs enwrapping the axonal processes and the SGCs shrouding individual somata. Myelinating glia regulate assembly of cellular adhesion molecules and ion channels that are key elements of axo-glial junctions and the paranodal structures at the node of Ranvier, a critical structure for saltatory conduction¹²³. Cochlear glia-associated paranodal structures and nodal clusters of Na⁺ channels are present along the entire length of AN processes where there are gaps between myelin^{50,124}. In the brain, dynamic regulation of nerve myelination, required for nerve plasticity and repair, continues into adulthood^{125,126}. Myelin deficiencies can significantly deplete neuronal activity due to loss of conduction velocity.

RNA binding proteins (RBPs) control post-transcriptional events such as pre-mRNA splicing and mRNA stability, localization and translation¹²⁷. This wide range of function allows these proteins to modulate the proteome of neural progenitor cells needed to facilitate differentiation into glial and neuronal cells and to conduct myelination and form neural circuitry⁵⁷. RBPs are known to have numerous downstream targets, and manipulation or dysregulation of these RBPs

can have extensive effects. The *Quaking (qkl)* gene encodes a KH-type family of RBPs and generates three major spliced transcripts encoding QKI-5, QKI-6, and QKI-7 isoforms that differ in their C-termini^{53,128}. QKI-5 harbors a nuclear localization signal and is located in the nucleus, while QKI-6 is expressed throughout the cell and QKI-7 is cytoplasmic^{57,129}. QKI-5 and QKI-6 directly or indirectly regulate myelin-specific genes such as myelin-associated glycoprotein¹³⁰⁻¹³². QKI-6 and -7 are largely expressed during active myelination¹²⁸. In the quaking viable mouse model, which is known for its myelin deficiency, the *qkl* isoforms and corresponding RBPs were reduced in glial cells compared to their wildtype counterparts^{128,133}.

In this study, we have examined the linkage between noise exposure and demyelination of SGNs and peripheral processes, focusing on the molecular mechanisms that drive myelinating glial dysfunction. For this purpose, we employed a noise-exposure paradigm in mice that resulted in permanent hearing loss. Our data show that noise exposure causes demyelination of SGNs and disruption of paranodal axo-glial junctions, promoting demyelination-associated inflammatory responses and widespread changes in myelin-related gene expression in the AN. Noise exposure caused a rapid response in QKI-RBP expression that was accompanied by changes in the expression of numerous QKI targets associated with myelination. Similar investigation of postnatal AN development revealed that upregulation of *qkl-6* and *qkl-7* and downregulation of *qkl-5* occurred around the first two weeks after birth, coinciding with myelination. Targeted deficiency of *qkl*/QKI-RBPs in adult

cochlear glia disrupted myelin structure and paranodal axo-glia junctions and resulted in hearing loss. Together, these results identify *qki*/QKI-RBPs dysregulation as a critical early component in the noise response, leading to glia dysfunction, demyelination and hearing loss.

4.2 Specific methods

4.2.1 Animals used

Young-adult CBA/CaJ mice aged 6-15 weeks and mice at ages P0, 3, 7, 10, 14, and 21 were used for this project. The *QKI^{FL/FL};PLP^{CreERT}*⁵⁹ model was produced by crossing *QKI^{FL/FL}*, which has loxP sites flanking exon 2 of *Quaking*, with *PLP-CreERT^{T2}*. The knockout was induced in ~10-week-old *QKI^{FL/FL};PLP^{CreERT}* mice by 5 intraperitoneal injections of 10 mg/ml TAM at 1mg/25g once per day. The knockout of exon 2, which is common for the three major QKI isoforms QKI-5, -6, and -7, should result in a null allele⁵⁹. Experiments were performed on ~15-week-old *QKI^{FL/FL};PLP^{CreERT}* mice 28 days after the final TAM injection. Age-matched *QKI^{FL/FL}*- littermates were used as controls.

4.2.2 Noise exposure

Noise exposure procedures were modified from previous studies¹³⁴. Young-adult CBA/CaJ mice were exposed to 8-16kHz octave-band noise at either 100dB, 106dB, or 112dB SPL for 2 hours using a Beyer DT48 drive

(Beyerdynamic, Farmingdale, NY) and monitored with a probe-tube microphone (B&K 4134; Bruel and Kjaer, Norcross, GA).

4.2.3 Physiological procedures

Mice anesthetized with ketamine/xylazine cocktail were tested for their ABR responses. ABR testing on the CBA/CaJ mice in this study was performed in a sound-isolation booth at MUSC. For the young-adult CBA/CaJ mice, ABRs were measured at 4, 5.6, 11.3, 16, 22.6, 32, 40, and 45.2 kHz frequencies. Stimuli were delivered 31 times/s and the signal consisted of 5ms tone pips with \cos^2 rise/fall times of 0.5ms. Responses were recorded from sound intensity levels from 90-10dB and each succeeding level was reduced by 5 dB steps. Wave I thresholds and suprathreshold responses of onset latency and peak amplitude were analyzed for each tested frequency. Pre-noise ABR recordings were used for as the control comparison, as well as for non-noise-exposed mice whose cochlea were used as control samples. For mice given noise exposure, ABRs were recorded immediately (Im), Day (D)1, D3, D7, D14, and/or D30 after noise exposure. ANs were harvested after each experimental time point. For each noise and control group, thresholds were averaged at each frequency and mean \pm standard error of mean (SEM) were calculated and plotted using Origin 6.0 software (OriginLab Corporation, Northampton, MA). For suprathreshold amplitude and onset latency, measurements for no-noise control and day 3 post-noise groups were averaged at each intensity level for each frequency.

ABR measurements were performed and collected from the right ears of each for mutant $QKI^{FL/FL;PLPCreERT}$ and $QKI^{FL/FL;-}$ littermate control mouse using a portable SmartEP system and software (Version 3.97) (Intelligent Hearing Systems, Miami, FL). Testing on these mice were performed in a portable sound-isolation apparatus at the Lady Davis Institute for Medical Research. ABRs were recorded just before the mice were sacrificed and ANs were collected. The ABRs were evoked at 8 and 16 kHz frequencies. The stimuli consisted of 1 ms in length Blackman pure tones which were delivered at 19.3 times/s. Sound intensity levels from 100-10dB SPL were tested, with each succeeding step being reduced by 10dB. Wave I thresholds were plotted by mean \pm SEM for each frequency for each mouse group. Suprathreshold wave I peak amplitudes and peak latencies were plotted by mean \pm SEM for each sound intensity level/frequency.

4.2.4 Microarray analyses

Noise-exposed AN samples were collected at 1m, D1, D7, and D14 after exposure. Comparative analyses were conducted with dChip software. AN samples were collected from mice of both sexes (n = 9 females, 6 males). To eliminate sex as a confounding variable, genes that were determined to be sex-dependent were excluded from all following microarray analyses. For unbiased expression analysis of the effect of noise, significant difference was defined as absolute fold change >1.5 and $p < 0.05$ (Student's t-test, unpaired, 2-tailed) for at least one pairwise relationship among the control and post-noise time points; FDR, estimated based on iterative comparisons using permuted group

assignments, approximated 24%. Enrichment analysis of biological process terms was conducted with DAVID (Database for Annotation, Visualization, and Integrated Discovery) ^{135,136}. Significantly enriched biological processes (adjusted $p < 0.05$, Benjamini and Hochberg adjustment) were summarized with REVIGO ¹³⁷. A set of myelin-related genes was compiled from several resources: 1) mRNAs enriched in myelinating oligodendrocytes in mouse cerebral cortex compared to astrocytes, neurons, oligodendrocyte progenitor cells, newly formed oligodendrocytes, microglia, and endothelia at FPKM thresholds of 0.1, 1, 10, 20 ¹³⁸; 2) mRNAs with normalized read counts of >100 and >2 -fold increase in male mouse brain myelin ¹³⁹; 3) genes on the mouse 430 2.0 GeneChip (Affymetrix) identified by query for the term myelin; and 4) a curated set of genes related to the node of Ranvier. A set of putative QKI target genes was compiled from genes alternatively spliced in a model of QKI deficiency ⁵⁹ and genes containing a QKI response element (QRE) ¹⁴⁰. Gene sets were processed with the NetAffx webtool (Affymetrix) to match genes with corresponding microarray content. Differential expression for focused analysis of myelin-related and putative QKI target gene sets was defined as $p < 0.05$ (Student's t-test, unpaired, 2-tailed) for at least one pairwise relationship among the control and post-noise time points.

4.2.5 RT-qPCR

Reverse transcription of total RNA was performed with the iScript cDNA synthesis kit (Bio-Rad) according to manufacturer protocol. Amounts of 25-50 ng of total RNA were used in 20 μ l reaction volumes and the obtained cDNA

products were diluted to 100 µl with nuclease-free water. qPCR was conducted as previously described¹⁴¹ in a CFX96 instrument (Bio-Rad) using SsoAdvanced Universal SYBR Green Supermix (Bio-Rad). Quantification of relative expression of our genes of interest were completed using the PCR Miner Web tool⁸⁰. Relative mRNA expression values for experimental genes were normalized using the reference genes *Tbp*, *Hprt* and *Actb*.

4.2.6 G ratio measurements

Myelin ultrastructures of mutant *QKI^{FL/FL;PLPCreERT}* and control *QKI^{FL/FL;-}* cochleas were analyzed via TEM. The myelin thickness and axonal diameters were measured from 3 ANs per experimental group, with 187 fibers being measured from the mutants and 224 fibers being measured from the controls. G ratios were calculated using the open-source imaging software, Fiji¹⁴², with the G Ratio for ImageJ plug-in (gratio.efil.de) using the developer's instructions.

4.3 Results

4.3.1 Noise-induced functional declines in the young-adult CBA/CaJ mouse AN

We first characterized pathophysiological alterations in cochleae of adult CBA/CaJ mice exposed to octave-band noise (8-16 kHz) at 106dB SPL for 2 hours. ABRs were measured at several time points after noise exposure to evaluate AN function. We calculated and show the threshold shifts, which can be found by subtracting the pre-noise threshold from the post-noise threshold results. For noise exposure at SPLs of 106dB, threshold shifts up to ~65 dB were seen at 1m (**Figure 4.3.1 a**). Although wave I thresholds improved by D3, PTS of >20 dB were present at 16 kHz and higher frequency regions for the 106 dB exposure. Suprathreshold measurements of amplitudes (**Figure 4.3.1 b**) showed significantly reduced wave I amplitudes D3 after noise compared to control. These results apparent for the mid-frequency at 11.3 kHz and much more so for the higher frequency at 32.kHz. To determine possible delays in conduction after D3 noise, we also measured onset latencies of wave I (**Figure 4.3.1 c**). We found that, especially in the higher frequency, there were significant delays in wave I latency in D3 compared to non-noise exposed controls. Larger, permanent threshold shifts and diminished wave I amplitudes post-noise can be explained by noise-induced hair cell death, as well as SGN apoptosis. The longer onset latencies imply pathological changes in the myelin and nodal structures.

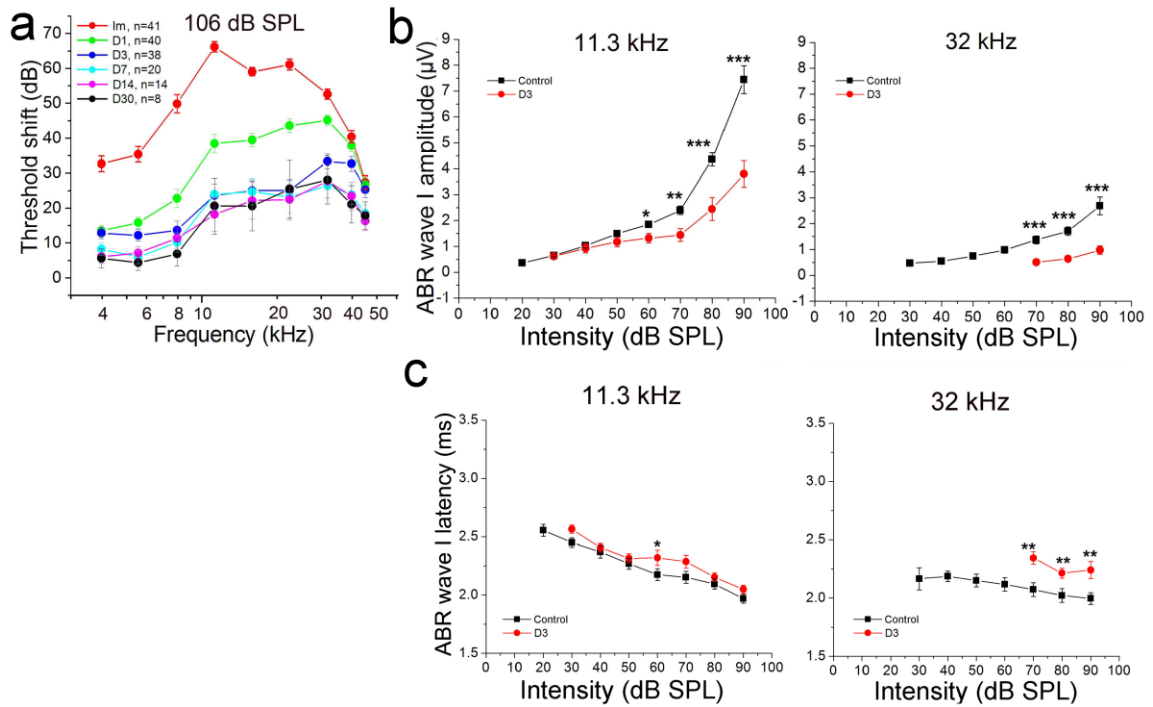


Figure 4.3.1: Noise-induced functional declines in the young-adult CBA/CAJ mouse AN

(a) ABR wave I threshold shifts showed dynamic alterations of mouse hearing sensitivity after noise exposure (b) Wave I amplitudes were reduced at 11.3 kHz (n = 11-17 noise; 16-17 control mice) and even more so at 32 kHz (n = 8-17 noise; 17 control mice) at D3 after 106 dB noise exposure (c) Onset latencies of wave I did not greatly change at 11.3 kHz (n = 11 noise, 17 control), but were significantly longer at 32 kHz (n = 8-17 noise, 17 control). (*p < 0.05, **p < 0.01 and ***p < 0.001; Mann-Whitney U test).

4.3.2 Noise-induced demyelination, disruption of paranodal axo-glial junctions, and recruitment of macrophages

Our previous studies of mouse and human cochleae demonstrated that myelin abnormalities occur prior to a significant AN loss, suggesting that glial dysfunction plays a critical role in the early phase of AN degeneration in sensorineural hearing loss⁸¹. To investigate this supposition, we examined ultrastructure of myelinating glia in mice exposed to 106 or 112 dB noise. Since this exposure paradigm induces PTS in the frequency range of 16 kHz and above (**Figure 4.3.1 a**), sections from 16-45.6 kHz regions of the cochlea were selected for TEM examination. Electron micrographs from control mice showed that type I SGNs are ensheathed with multiple layers of compact myelin lamellae proximal to the glia and multiple layers of non-compact myelin lamellae proximal to the neuron (**Figure 4.3.2 a,b**). Myelinating cells enclosing axons have often only compact myelin (**Figure 4.3.2 b**). Myelin paranodal loops were seen to be in tight contact with axons through axo-glial junctions (**Figure 4.3.2 b**). Loss/disruption of myelin was frequently observed in the AN nerve within RC at D1 (**Figure 4.3.2 c**), whereas no gross pathological alterations were seen in the neuronal bodies. Disruptions were also present in paranodal axo-glial junctions (**Figure 4.3.2 d**). Myelin abnormalities were more pronounced at D14 and included loss/disruption of compact myelin lamellae and the appearance of degenerative myelin whorls were very much pronounced (**Figure 4.3.2 e**).

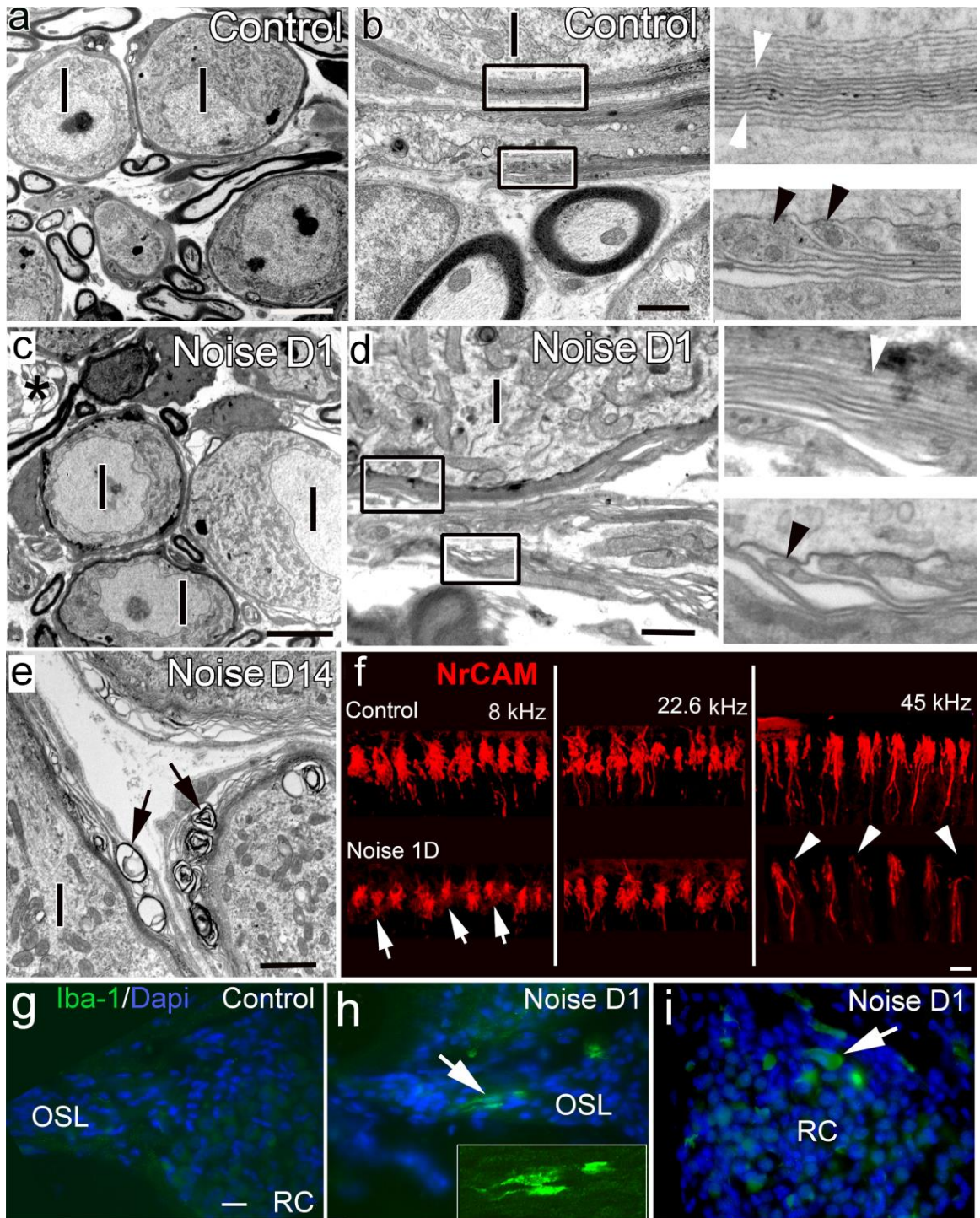


Figure 4.3.2: Noise-induced demyelination, disruption of paranodal axo-glial junctions, and recruitment of macrophages

(a, b) Normal type I (I) SGNs and myelinating glial cells in an adult CBA/CaJ mouse. Enlargements of (b) show compact myelin lamellae (white arrowheads) and paranodal axo-glial junctions (black arrowheads). (c) Disruption of the myelin sheath surrounding neurons (asterisk), (d) loosening of SGN myelin (white arrowhead), and disruption of axo-glial junctions (black arrowhead) D1 after 106dB noise. (e) Myelin whorls and cytoplasmic vacuolization (arrows) of dysmyelinated SGNs D14 after 106 dB noise. (f) Reduction (arrows) and eventual loss (arrowheads) of NrCAM⁺ nodal structures at the habenula at D1 after 112 dB noise. (g) No Iba-1⁺ macrophages seen in control AN. (h-i) Increased presence of Iba-1⁺ macrophages in OSL (h) and RC (i) are seen D1 after 106 dB noise.

Neuronal cell adhesion molecule (NrCAM) is expressed in the nodal axolemma and plays an important role in maintenance of the axon initial segment and the nodes of Ranvier³⁸. Immunostaining of the AN with anti-NrCAM antibody at D1 revealed a loss of axon initial segments (heminodal) at the habenula opening in regions encoding 8 kHz and higher frequencies (**Figure 4.3.2 f**). These results were consistent with the appearance of myelin abnormalities and disruption of paranodal structures at similar frequencies, perhaps leading to slower conduction velocities.

Macrophages contribute to the process of nerve degeneration by phagocytosing myelin debris and axonal remnants. Macrophage recruitment/migration into the cochlea has been reported to occur following noise-induced cochlear insult^{143,144}, ototoxic drug-induced SGN degeneration¹⁴⁵ and genetic modification-induced hair cell loss¹⁴⁶. To validate the presence of macrophages in the AN, sections from control and noise-exposed ears were immunostained with Iba1, a key calcium binding protein that is expressed by microglia/macrophages, but not neural cells¹⁴⁷. Iba1⁺ macrophages were present in several regions of the AN in noise-exposed cochleae compared to control (**Figure 3.4.2 g-i**).

4.3.3 Expression patterns of QKI variants and potential targets of QKI in response to noise injury

To understand molecular changes following noise exposure, we performed microarray transcriptional profiling on AN from control adult mice and mice at 1m, D1, D7, or D14 (n = 3 per group). Differential expression analysis

identified 1247 gene representations (probe sets) corresponding to 901 unique genes that were significantly different among the pairwise relationships (**Figure 4.3.3 a**). Examination of expression patterns for the noise responsive genes showed that most exhibited transient up- or down-regulation after exposure that peaked in I1m or D1 samples, but returned to near normal levels in D14 samples. Analysis of biological processes enriched among all of the differentially expressed genes detected a core set of related processes associated with wounding and inflammation (**Figure 4.3.3 b**, upper network), including the process that had the overall highest enrichment score, immune response ($p_{adj} = 5.9 \text{ E-}08$). Also enriched among the differentially expressed genes was a set associated with apoptosis and DNA metabolism (**Figure 4.3.3 b**, middle network) and independent processes that included cell cycle and positive regulation of development (**Figure 4.3.3 b**, lower panel).

To address the myelin pathologies observed following noise exposure, we specifically examined expression data for myelin-related genes. The list of myelin genes interrogated was compiled from several sources, including the gene ontology database and data sets produced from recent RNA-seq profiling of myelinating cells^{138,139}. The compiled myelin list comprised 1849 unique genes that in turn corresponded to 3510 probe sets for the microarray platform used in our experiments. Analysis of expression of these myelin-related genes in response to noise (**Figure 4.3.3 c**) found that roughly half were statistically different ($p < 0.05$) for at least one pairwise relationship in our data set (1063 of 1849 unique genes = 57%; 1560 of 3510 probe sets = 44%).

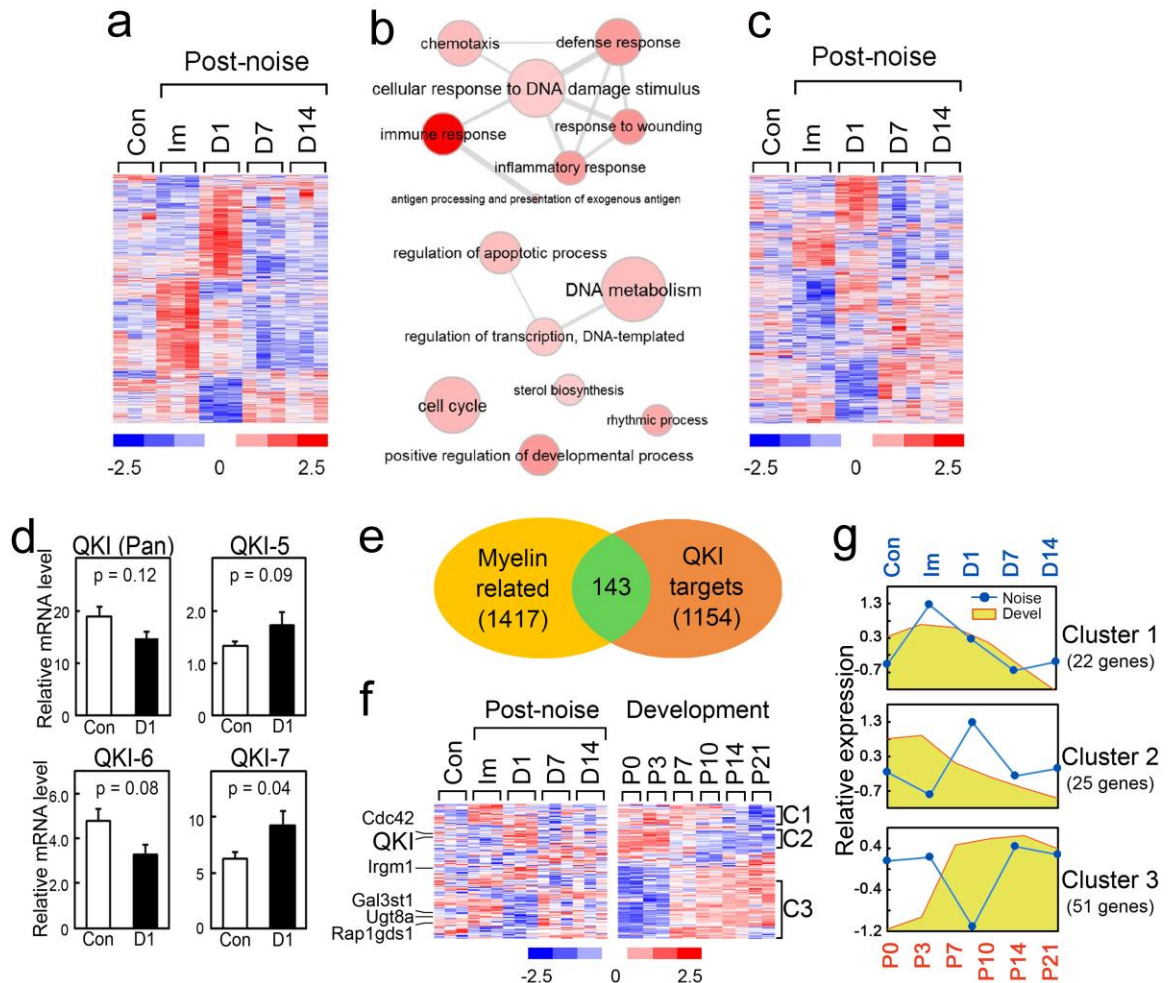


Figure 4.3.3 Expression patterns of QKI variants and potential targets of QKI in response to noise injury

(a) Microarray analysis identified 1247 gene probe sets differentially expressed (fold change >1.5 and $p < 0.05$; Student's unpaired t-test) following noise. **(b)** Enrichment analysis results for gene ontology biological process terms associated with the analysis in **a**. **(c)** Microarray expression profiles of 1560 myelin-related genes probe sets that were affected by noise exposure ($p < 0.05$, Student's unpaired t-test). **(d)** Relative expression levels of all QKI mRNA (Pan) and QKI variants in control mice and mice at D1 after noise exposure. **(e)** Overlap between myelin-related genes and putative QKI targets regulated by noise exposure. **(f)** (Left panel) Microarray expression profiles for the 143 gene probe sets depicted in that are myelin related, putative QKI targets and differentially expressed in response to noise. (Right panel) Expression profiles of the 143 genes in the developmental ANs at P0-21. **(g)** Average relative (Z standardization) expression patterns for clustered genes identified in **f**. Relative noise responses are summarized by line graph (blue); relative developmental patterns are summarized by area graph (yellow).

Clustering analysis of expression patterns for these genes again showed that many underwent transient up- or down-regulation that peaked in I1m or D1 samples.

Among genes differentially expressed in response to noise, the *qkl* gene is well characterized as a key regulator for the formation and maintenance of myelin and axo-glial junctions in the central nervous system⁵⁹. The *qkl* gene generates three major spliced transcripts encoding QKI-5, QKI-6, and QKI-7 isoforms⁵³. Here we examined the expression of total QKI (pan) and specific variants in response to noise. Quantitative PCR analysis of isoform expression in the mouse AN 1 day after noise exposure revealed significant change in QKI-7 but not in QKI-5 and -6 (**Figure 4.3.3 d**). These data, coupled with our findings of differential expression of QKI by microarray, demonstrated that QKI isoform expression is altered in response to noise and suggests that targets of QKI may also be affected.

We therefore reanalyzed the microarray expression data to examine putative targets of QKI-RBPs, compiling a list of 1416 mRNAs containing the QKI response element (QRE), a bipartite consensus binding sequence¹⁴⁰, and 28 RNAs detected as differentially spliced in mouse oligodendrocytes⁵⁹. Collectively, the list of putative QKI targets corresponded to 3102 probe sets on the microarray platform used for our study. Query of these probe sets revealed that 1297 (42%) were statistically different ($p < 0.05$, Student's t-test, unpaired) for at least one pairwise relationship in our data set. Clustering analysis of expression patterns for these putative QKI targets regulated by noise again

showed that most underwent transient up- or down-regulation peaking at Im or D1 after noise exposure.

Given the established relationship between QKI and myelin¹⁴⁸, we determined the overlap between the myelin-related genes affected by noise and the putative QKI targets affected by noise. Of the 1560 differentially expressed myelin related probe sets and the 1297 differentially expressed QKI target probe sets, 143 were both myelin-related and putative QKI targets (**Figure 4.3.3 e**)

Unsurprisingly, QKI was one of the genes identified by this analysis; other genes of interest included *Cdc42*, *Irgn1*, *Ugt8a*, *Egr2*, *Mal*, *Kcna1*, *NF1* and *Nfasc*. Our previous study revealed that acute nerve injury caused transcriptional effects in the AN resembling a developmental transition from mature to immature state⁷⁴. For example, AN injury caused up-regulation of *Sox2* and other neural progenitor-related genes and increased proliferation of a subset of glial cells. Specific temporal patterns of QKI expression in developing nerve tissue are associated with the states of glial cell differentiation and myelination. For example, expression of QKI-6 and QKI-7 peak around P14, coinciding with myelination of brain tissues^{53,128}. We next examined if this select group of genes, which are myelin-related, and putative QKI targets that are responsive to noise injury also exhibited evidence of developmental regulation. To address this, we queried our previously described microarray data set that profiled mouse auditory development from postnatal days 0 to 21 (P0-P21)⁷⁴, which covers a critical period for glial maturation and myelination. Clustering analysis of these genes (**Figure 4.3.3 f**) revealed that nearly all showed vivid patterns of up- or

downregulation during the developmental period. Inspection of the heatmap involving both injury and development profiles identified three prominent clusters, with two (clusters 1 and 2) showing up-regulation by noise and down-regulation during development and the third (cluster 3) showing the opposing pattern of downregulation by noise and upregulation during development (**Figure 4.3.3 g**). Among these clusters, only cluster 1 showed temporal patterns for development and noise-exposure that were fundamentally similar. For clusters 2 and 3, the developmental and injury temporal response patterns were largely opposing. Of the 143 myelin-related, putative QKI target, noise responsive genes, 98 were present in these three clusters (69%). Opposing temporal relationships were also apparent in the unclustered QKI targets, which contain 31% of myelin-related QKI targets. These results highlight that there is similarity but also discordance in how putative QKI targets are regulated in the developmental, pro-myelination state, versus the injury response state.

4.3.4 Expression patterns of QKI isoforms in postnatal and adult ANs.

To extend our observation of QKI regulation in AN during postnatal development, we analyzed expression of total QKI (Pan) and the three different isoforms, focusing on three critical stages of myelination: P3, 7, and 14 (**Figure 4.3.4 a**) Pan-QKI expression increased gradually through postnatal development, with a significant increase in expression between P3 and P14.

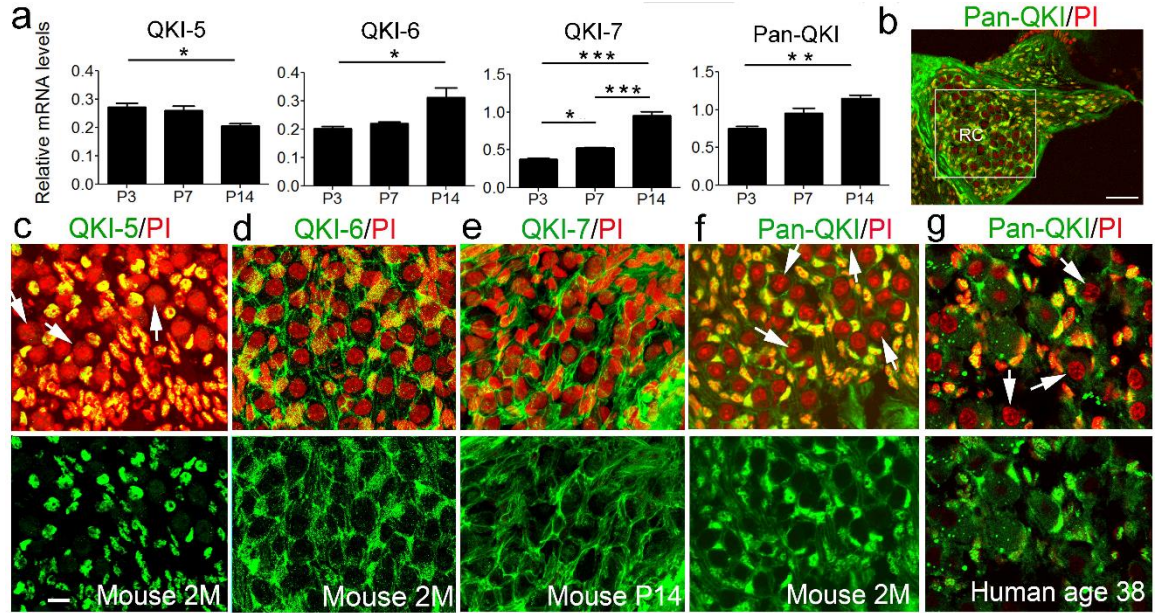


Figure 4.3.4: Expression patterns of QKI variants in normal postnatal and adult AN

(a) Expression levels of *qki-5* mRNA decrease from postnatal (P) day 3 to 14, while QKI-6 and QKI-7 levels increase from P3 to P14, presenting a pattern similar to that seen for Pan-QKI. Relative expression levels of all QKI mRNA (Pan and QKI variants) were measured by qPCR analysis in the ANs of CBA/CaJ mice at P3, P7, and P14. Expression levels shown are normalized to *Hprt* and *Actb*; error bars indicate SEM; * $p < 0.05$, ** $p < 0.01$, and *** $p < 0.001$ by ANOVA with Bonferroni's post-test. $N = 3$ mice/time point. (b) Low magnification image of AN section immunostained with anti-Pan-QKI highlighting location of RC where all images were obtained. (c-g) Immunostaining with anti-QKI antibodies showing protein expression patterns of QKI-RBPs in the glial cells, but not neurons (white arrows) of the normal ANs from mice aged 2 months (2M; c,d,f) or 14 days (e) and temporal bone from a human ear, aged 38 years (g). The nuclei were stained with PI. Scale bars: 50 μm in b; 8 μm in c (applies to c-g).

All three of these transcripts were detectable throughout postnatal development with *qki-7* being more abundant than *qkl-5* and *qkl-6*. The isoforms *qkl-6* and *qki-7* were both significantly upregulated during postnatal development while *qkl-5* was significantly downregulated. These patterns match findings for *qkl* isoform expression in the mouse brain⁵³, with *qkl-6* and *qki-7* increasing and *qkl-6* and *qki-7* decreasing in the mouse AN at times that coincide with the onset of myelination.

We further examined auditory QKI expression, detecting total and variant QKI proteins in mouse and human cochlear sections. Analyses in mice were focused on RC (**Figure 4.3.4 b**), which contains SGCs that ensheath soma of SGNs and SCs that myelinate fibers. Immunohistochemical analyses were done on cochlear sections from 2-month-old young-adult mice (**Figure 4.3.4 c-f**) and P14 mice (**Figure 4.3.4 e**), and both ears from a 38-year-old human donor (**Figure 4.3.4 g**). QKI-5 was expressed in nuclei of both SCs and SGCs (**Figure 4.3.4 c**). QKI-6 and -7 were expressed predominantly in the cytoplasm of glia surrounding SGNs and fibers (**Figure 4.3.4 d,e**). Pan-QKI detection in mouse confirmed that total QKI protein was distributed in both nucleus and cytoplasm but that it was limited to glial cells (**Figure 4.3.4 f**). Pan-QKI detection in human temporal bones revealed a similar distribution, with QKI present in nuclei and cytoplasm of SCs and SGCs, but not neurons (**Figure 4.3.4 g**).

4.3.5 Reduction of QKI protein expression in AN glial cells of adult $QKI^{FL/FL};PLP^{CreERT}$ mice

To investigate the importance of QKI-RBPs to glial cell function in the auditory system, we examined the effects of *qkl* deficiency by using the $QKI^{FL/FL};PLP^{CreERT}$ mouse model that targets all *qkl* variants in glial cells. The $QKI^{FL/FL};PLP^{CreERT}$ mouse model was generated by crossing $QKI^{FL/FL}$ with an inducible Cre knockout line, *PLP-CreERT*, that induces *qkl* knockout in *Plp1* expressing glial cells after being activated by injections of TAM⁷².

Immunostaining analyses of RC and OSL regions were performed on cochleae of 15-week-old TAM-treated $QKI^{FL/FL};PLP^{CreERT}$ mice and compared to $QKI^{FL/FL};-$ littermate controls (**Figure 4.3.5 a**). Immunostaining for Pan-QKI showed that nuclear QKI was notably reduced in SGC nuclei in QKI deficient cochleae compared to glia in control cochlea (**Figure 4.3.5 b**). QKI was also substantially reduced in glial cytoplasm of $QKI^{FL/FL};PLP^{CreERT}$ mice compared to controls, which had a QKI distribution comparable to that seen in CBA/CaJ mice (**Figure 4.3.4 f**). Figure 4.3.5c illustrates a substantial loss of QKI in nuclei and cytoplasm of SCs ensheathing peripheral fibers in the OSL. To determine QKI reduction specifically in the glial cells, dual immunostaining was performed for Pan-QKI with Sox10, a marker of glial cell nuclei ^{149,150}.

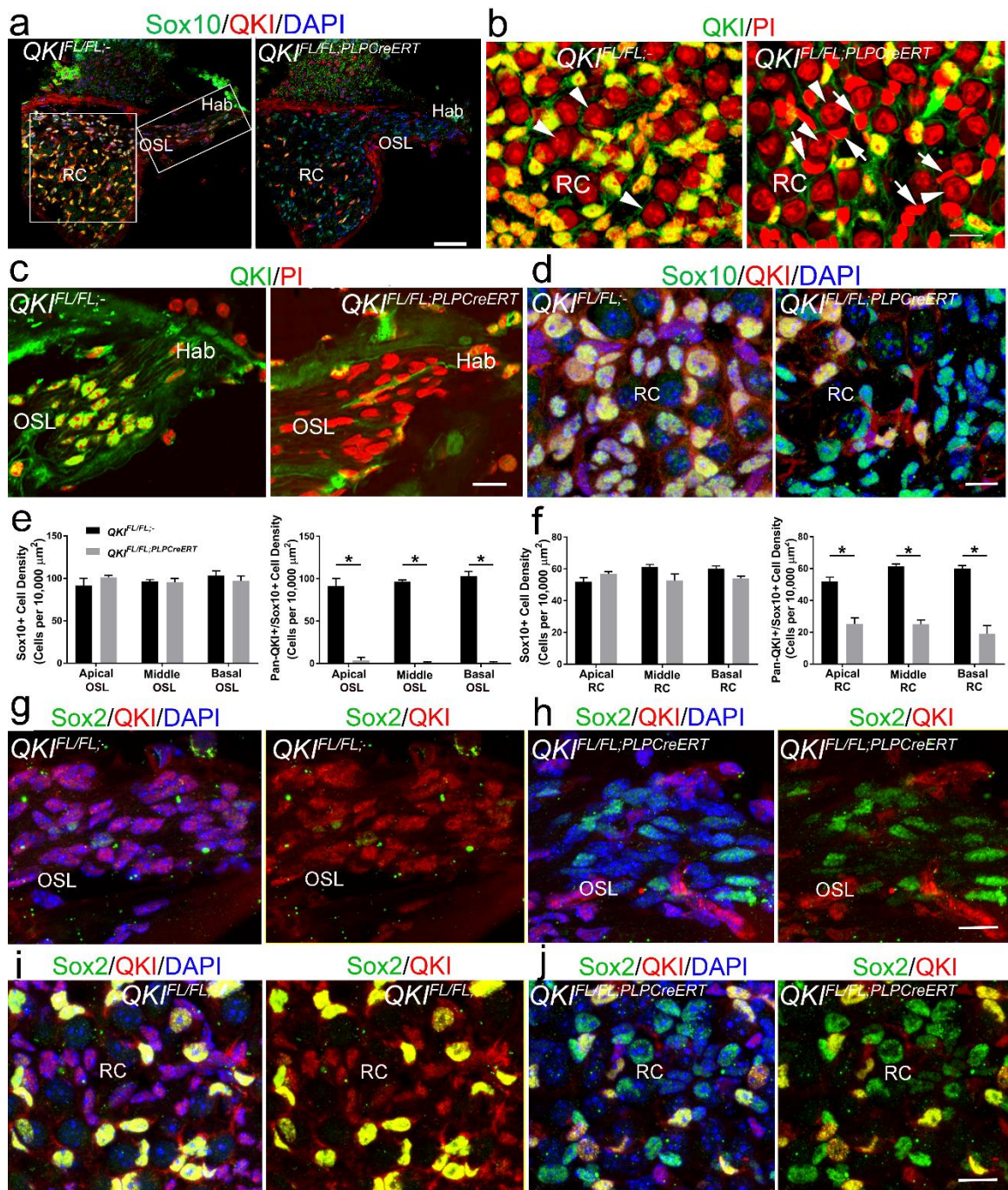


Figure 4.3.5: Reduction of QKI protein expression in AN glial cells of adult *QKI^{FL/FL};PLP^{CreERT}* mice

(a) Low magnification images of *QKI^{FL/FL}*^{-/-} and *QKI^{FL/FL};PLP^{CreERT}* ANs after TAM immunolabeled for Pan-QKI and Sox10. RC, OSL, and Hab regions are indicated. Nuclei were counter stained with PI. **(b,c)** Pan-QKI (QKI) immunoreactivity in glial cell nuclei is greatly reduced in both RC **(b)** and the OSL **(c)** of QKI exon 2 mutation mice. Control *QKI^{FL/FL}*^{-/-} and mutant *QKI^{FL/FL};PLP^{CreERT}* mice were evaluated 4 weeks after TAM injections. **(d)** Dual immunolabeling for Pan-QKI and Sox10, demonstrates the loss of QKI expression in most Sox10⁺ glial cells (green). Nuclei were counter stained with DAPI. **(e-f)** Cell density counts for total glial cells in OSL (as indicated by Sox10⁺ cells) and glial cells expressing QKI (as indicated by cells positive for both Sox10 and Pan-QKI) in OSL **(e)** and RC **(f)** from the three cochlear turns in *QKI^{FL/FL}*^{-/-} and mutant *QKI^{FL/FL};PLP^{CreERT}* mice. Total glial cells, based on density, were not significantly different between control and mutant mice in the OSL and RC of any of the turns (left panels for **e,f**). There were almost no QKI positive glial cells in the OSL **(e**; right panel); QKI positive glial cell density in RC **(f**; right panel) was decreased by more than half in all cochlear turns in QKI deficient mice compared to controls. N = 4 for each group; error bars indicate SEM; * *p* < 0.05 by the Mann-Whitney test **(g-j)** Dual immunostaining for Pan-QKI and Sox2, a glial progenitor marker, revealed much higher reactivity of Sox2 in the OSL **(g-h)** and RC **(i-j)** in *QKI^{FL/FL};PLP^{CreERT}* compared to control *QKI^{FL/FL}*^{-/-} mice. Scale bars: 50 μm in **a** and 15 μm in **b-d, g-j**.

We chose the pro-differentiation/myelination factor Sox10 because it is expressed in fully differentiated, mature SCs in the adult peripheral nervous system^{149,151,152}. In control mice, QKI colocalized with Sox10 in nuclei of SGCs and SCs in RC (**Figure 4.3.5 d**). However, only few QK⁺ cells stained positively with Sox10 antibody in QKI-deficient mice (**Figure 4.3.5 d**). Quantification of Sox10⁺ glia cells expressing QKI showed that there was a profound reduction in Pan-QKI⁺/Sox10⁺/DAPI⁺ cell density in the OSL of *QKI^{FL/FL};PLPCreERT* mice compared to controls (**Figure 4.3.5 e**). Quantification of Pan-QKI⁺/Sox10⁺/DAPI⁺ cells in RC also showed a significantly reduced density in QKI-deficient mice compared to controls (**Figure 4.3.5 f**). Total glia cell counts were not significantly different between *QKI^{FL/FL};-* and *QKI^{FL/FL};PLPCreERT* ANs.

To investigate further the consequences of QKI deficiency in cochlear glial cells, we evaluated distribution of Sox2, a glial progenitor marker^{153,154}, in control and QKI-deficient mice. Sox2 is a marker of immature, undifferentiated glia and negatively regulates myelination by inhibiting SC differentiation^{153,155} and promotes a progenitor-like glial state associated with neuronal repair after injury¹⁵⁶. Sox2 expression declines as glia mature¹⁵⁵, but is present in SGCs in adult nerves¹⁵⁷. In our studies, OSL of control mice contained only few Sox2⁺ cells and there was no colocalization of Sox2 with QKI in SCs (**Figure 4.3.5 g**). Sox2⁺ cells were more abundant in RC of control mice and these Sox2⁺ SGCs stained positively for Pan-QKI antibody (**Figure 4.3.5 i**). Interestingly, QKI-deficient mice showed a substantially different profile of Sox2 expression. In the OSL, there was a notable increase in the number of Sox2⁺ SCs (**Figure 4.3.5 h**)

though there was still no evident colocalization of Sox2 and residual QKI in the mutant animals. In RC of QKI-deficient mice, Sox2⁺ SGCs appeared to be increased compared to controls (**Figure 4.3.5 j**). These findings suggest that QKI deficiency may lead to dedifferentiation in a subset of cochlear glia.

4.3.6. Diminished QKI expression results in demyelination and disruption of paranodal structures in the adult AN

To examine further the role of QKI-RBPs in AN architecture and function, we assessed ultrastructure of myelin and flanking paranodes in *QKI^{FL/FL};PLP^{CreERT}* mice in OSL, Hab, and RC regions (**Figure 4.3.6 e**). We examined 41 nodal structures associated with 54 glial cells of 3 *QKI^{FL/FL};PLP^{CreERT}* mice, and 17 nodal structures associated with 34 glial cells of 3 *QKI^{FL/FL};⁻* control mice. QKI-deficient mice showed evidence of hypomyelination, with a reduced number of lamellae wrapping some type I AN fibers (**Figure 4.3.6 a,f**). Mutants also exhibited aberrant myelin structure and the presence of unmyelinated fibers (**Figure 4.3.6 f**). In addition, QKI-deficient mice exhibited pathologies in the paranodal region flanking the node of Ranvier. In the control mice, terminal myelin loops of each lamellae were well-organized, closely-apposed to each other and appeared to have proper septate-like junctions connecting the loop heads to the axolemma (**Figure 4.3.6 b**). In the QKI-deficient animals, the paranode had thinner terminal loop heads that were more broadly spaced, with some large gaps present within the structure (**Figure. 4.3.6 g**).

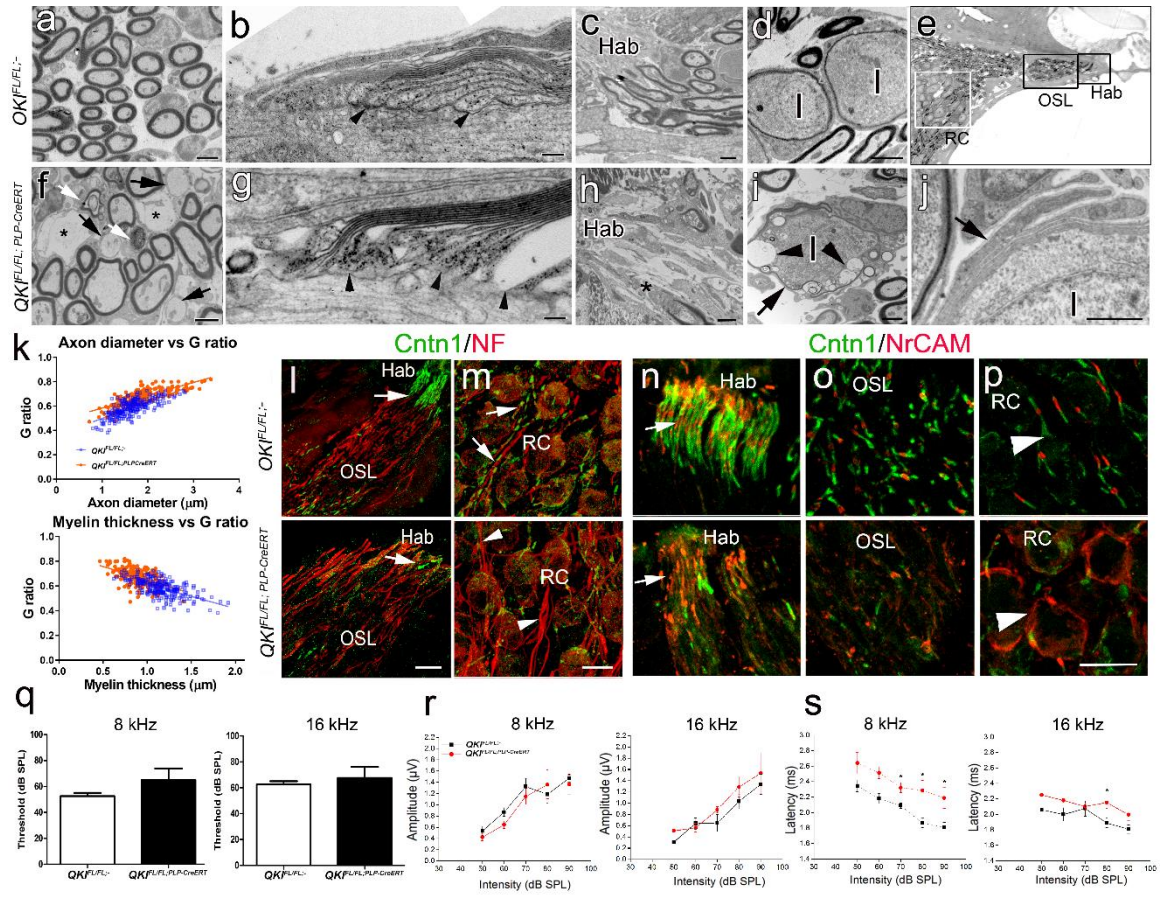


Figure 4.3.6: Diminished QKI expression results in demyelination and disruption of paranodal structures in the adult AN

(a-d) Ultrastructural features of **(a)** AN fibers, **(b)** a paranodal junction, **(c)** axon initial segments at the habenula (Hab) opening and **(d)** SGNs in cochleae from control $QKI^{FL/FL;-}$ mice 4 weeks after TAM injections. **(e)** Low magnification image of a control AN highlighting the location of RC, OSL and Hab. **(f-j)** Abnormalities in myelin morphology around axons and type I (I) SGNs and paranodal structures in $QKI^{FL/FL;PLPCreERT}$ mice 4 weeks after TAM injections. Pathological manifestations associated with diminished QKI expression included missing nerve fibers (**f**; *), myelin enfolding (**f**; white arrows), thinning myelin or reduced myelin lamellae (**f,i,j**; black arrows), a loss of the myelin sheath at the axon initial segment (**h**; *), and cytoplasmic vacuolization in glial cells (**i**, black arrowheads). The image in **g** shows disruptions in a paranode (black arrowheads) of a mutant mouse. Terminal myelin loops of the paranodal junctions flanking the nodes of Ranvier in the mutant mouse are disorganized, with abnormal spaces between the lamellae, and loop heads disconnected from the axolemma. Myelin lamellae ensheathing the somata of a mutant mouse are less compact and decreased in number (**j**; black arrow). **(k)** G ratio analysis revealed hypomyelination in the AN fibers, in particular the large-caliber fibers (with diameters $>3\ \mu\text{m}$), in $QKI^{FL/FL;PLPCreERT}$ mice. $N = 3$ mice/group. **(l-m)** Immunostaining for paranodal Cntn1 and the neuronal marker neurofilament 200 showed that while numbers of NF⁺ nerve fibers (white arrows in **m**) remained similar, expression of paranodal Cntn1 was decreased greatly (white arrows in **l, m**) in mutant mice. **(n-p)** Immunostaining for Cntn1 and the nodal marker NrCAM revealed the disappearance of Cntn1⁺ paranodal flanks in heminodes at the Hab (white arrows in **n**), the nodes of Ranvier along fibers in the axonal (**o**) and in ganglion nodes (**p**). ABR measurements from control and mutant mice showed no significant difference in ABR wave I thresholds (**q**) or amplitudes (**r**) between the two groups at 8 and 16 kHz. In contrast, ABR wave I onset latencies (**s**) were significantly increased in the mutant mice (* $p < 0.05$ by Student's unpaired t test, $n = 4$ $QKI^{FL/FL;-}$ mice; 3-4 $QKI^{FL/FL;PLPCreERT}$ mice). All data were presented as mean \pm SEM. Scale bars, 2 μm in **a,f**; 400 nm in **b,g**; 2 μm in **c,d,h,i**; 800 nm in **j**; 8 μm in **l,m**; 8 μm in **p** (applies **n-p**).

In the habenular region, where AN fibers form heminodes, demyelinate naturally and connect to the organ of Corti, the control AN showed thickly myelinated fibers close to the bony perforation, along with unmyelinated heminodes (**Figure 4.3.6 c**). In contrast, in the QKI-deficient sample there were few myelinated fibers which were in different states of dysmyelination, and there was a large open space clear of heminodes and axons (**Figure 4.3.6 h**). Soma of type I SGNs were densely myelinated and appeared healthy in control mice (**Figure 4.3.6 d**), whereas type I neurons in the QKI-deficient mice showed dysmyelination, with debris-laden spaces separating the cell membrane from the lamellae (**Figure 4.3.6 i**). Additionally, regions of hypomyelination with limited, noncompact lamellae could be seen in close proximity to densely myelinated somata (**Figure 4.3.6 j**). The observation of hypomyelination in the QKI-deficient animals was supported by a measured increase in the G ratio compared to controls (**Figure 4.3.6 k**).

To understand what may be causing the structural aberration in the axo-glia junctions at the paranodes in QKI-deficient animals, we performed co-immunostaining for Cntn1, an axo-glia connector protein⁴², and neurofilament 200¹⁵⁸. Sections from the OSL and RC in control samples showed characteristic paranodal patterns throughout the nerve fibers (**Figure 4.3.6 l,m, upper panels**). Conversely, Cntn1 staining and the distinctive patterns were largely absent in the QKI deficient samples (**Figure 4.3.6 l,m; lower panels**). As another measure of the effect of QKI deficiency on nodal structures, we performed dual immunostaining for NrCAM and Cntn1. In QKI-deficient animals, paranodes

flanking the heminodes were devoid of Cntn1 at the habenula (**Figure 4.3.6 n; lower panel**) and were mostly absent on the flanks of axonal nodes of Ranvier in the OSL compared to controls (**Figure 4.3.6 o**). Some Cntn1⁺ paranodal structures were seen in the RC in QKI-deficient cochleae (**Figure 4.3.6 p**).

AN function was tested in QKI-deficient animals by ABR measurements. Comparison of controls versus QKI-deficient animals showed that latencies of ABR wave I responses were significantly delayed for 8 and 16 kHz stimuli in QKI deficient animals (**Figure 4.3.6 s**). However, ABR thresholds of wave I were not significantly different between control and QKI-deficient groups for 8 and 16 kHz stimuli (**Figure 4.3.6 q**) and neither were the measured amplitudes (**Figure 4.3.6 r**). These findings show that QKI-deficient mice have ABR defects consistent with the dysmyelination observed in these animals.

4.4 Discussion

While it is well-established that myelination of nerve fibers by myelinating glia, and dynamic regulation of this activity, is crucial for proper nerve function, little is known about pathological changes in cochlear myelinating glia following injury/stress such as noise exposure. Our findings show that noise exposure sufficient for inducing nerve degeneration and permanent hearing loss elicits a rapid cellular and molecular response on myelinating glia. Our data reveal that dysfunction of QKI-RBPs and their putative targets lead to myelinating glial dysfunction, resulting in SGN demyelination, disruption of paranodal axo-glial

junctions, and AN functional deficiencies. These findings implicate a new mechanism of AN functional deficiency in noise-induced hearing loss (NIHL).

In these studies, we used a model of NIHL with more severe noise exposure levels of 106 or 112 dB SPL for 2 hours at 8-16 kHz. Within a short time, young-adult mice showed PTS across most cochlear frequency regions. This exposure protocol generates a cochlear injury of sufficient magnitude to allow characterization of the cellular and molecular responses of the AN. In a previous study, a noise-exposure regimen of 110 dB SPL for 9 h in adult rat ears resulted in demyelination of the central portion of the AN and decreased conduction velocity⁵¹. Our data expand on this important finding, showing that such noise causes demyelination of the SGNs and paranodal axo-glial junctions in the peripheral process in the ANs. These results are also consistent with a previous report in which thinner myelin sheaths were identified in the peripheral process of the AN after noise exposure¹⁵⁹.

Another interesting finding of our study is that inflammatory cells, particularly activated macrophages, are involved in demyelination of SGNs and ANs after noise exposure. Our data showed that the macrophages appear to be recruited in regions of noise-induced demyelination. This was supported by our gene expression analysis, which found inflammation to be one of the top biological processes induced in AN after noise exposure. After injury in the peripheral nervous system, degenerating myelin and axon debris is phagocytosed by either resident or infiltrating macrophages¹⁶⁰. Emerging evidence suggests that macrophages can be both detrimental and beneficial with

regard to nerve regeneration and remyelination¹⁶¹. Our recent study demonstrated that hematopoietic-derived macrophages contribute to AN remodeling after SGN loss¹⁴⁵. Additionally, Kaur et al. (2015), reported that macrophage recruitment into the cochlea enhances survival of SGNs in a model of selective hair cell deletion. Further experiments are needed to determine whether macrophages in the AN promote remyelination of AN and neuron survival.

Glial proliferation following injury is an important aspect of remyelination involved in nerve repair. In the peripheral nervous system, rapid SC proliferation is required for remyelination following injury¹⁶². In the central nervous system, glia (e.g. oligodendrocytes) can proliferate after injury, but the period is more restricted than that of the SCs in the peripheral nervous system¹⁶². Even under severe injury conditions that induce rapid type I SGN loss, glial cells show a dramatic increase in proliferation. However, despite this remarkable capacity of glial cells to proliferate in response to injury, there is no direct evidence of AN remyelination or axon regeneration after cochlear injury for animal models of NIHL, despite several decades of study^{163–168}. Here, our finding that QKI-RBPs and associated myelin targets undergo dysregulation after noise exposure provides molecular insight into the failure of remyelination and regeneration after noise injury and is potentially applicable to forms of neurodegenerative disease¹⁶⁹.

Here, our transcriptomic data revealed distinct QKI isoform expression patterns in noise-exposed animals as well as during mouse hearing

development. During development, the transition from immature to mature (myelinating) state was matched by an increase in *qkl-6* and *qkl-7* and decrease in *qkl-5*. Interestingly, in noise-exposed ANs, while there were suggestive expression differences for all *qkl* isoforms, only an up-regulation of *qkl-7* was detected as significant. Thus, the *qkl* isoform expression pattern following noise injury does not fully recapitulate a developmental, pro-myelination state. These data suggest the possibility that this deficiency in the *qkl* isoform response, and the downstream consequences on myelin target gene expression, are causal factors in the failure of remyelination leading to NIHL. A better understanding of how *qkl* isoform expression is controlled in cochlear glia may lead to new therapeutic interventions for NIHL and other neurodegenerative disorders.

Our studies reveal the critical roles of myelinating glia and QKI-RBPs in the maintenance of young-adult AN. In response to noise injury, young-adult mice rapidly exhibit glial dysfunction and altered expression of QKI-RBPs in the AN. Transcriptomic analysis and pathophysiological evaluation of noise-exposed mice indicate that these dysfunctions represent a primary response to noise injury that ultimately culminates in NIHL. Furthermore, our data suggests that the influence of *qkl* on myelination is dependent on precise control of *qkl* isoform expression.

Chapter 5: Glial dysfunction in auditory nerve development leads to dysmyelination and loss of hearing function

5.1 Introduction

In Chapter 3 we highlighted the importance of proper nodal formation and maturation for AN function. In addition to our findings, we found the methods we used in these nodal studies to be useful tools in assessing glial function, especially pertaining to their ability to generate and maintain normal compact myelin with strong, organized connections with SGN axolemma. In Chapter 4, we showed that AN glial cells become dysfunctional after noise injury, in part due to the dysregulation of QKI-RBPs and their downstream targets. We also determined that *qkl* KO in young-adults causes dysmyelination, leading to disruptions in the axo-glial connections at the paranodal domain and loss of hearing function. Thus far, we showed the importance of normal myelination and nodal formation/maturation for enhancement of hearing function after hearing onset and revealed the importance of myelin/axo-glial maintenance for normal hearing function after noise injury.

In both the developmental and noise settings that we studied, there are other cochlear factors that are involved that are affecting hearing function. During cochlear development, there are other cochlear components forming and maturing. The stria vascularis of the cochlear lateral wall is composed of cells that are responsible for potassium cycling in the endolymph. Potassium in the

endolymph and the generation of the endocochlear potential is required for proper mechanotransduction of the IHCs. Both the emergence of the endocochlear potential and the maturation of HCs, especially the connection between HC synapse ribbons and the afferent AN fibers, occur during early postnatal development around the onset of hearing^{103,170}. In noise injury, the HCs and lateral wall are affected along with the AN fibers/glia. We and other studies¹¹⁸ show that hair cells degenerate after high-intensity noise exposure that resulting in PTS. Lower-intensity noise exposures also cause synapse ribbon loss that result in temporary threshold shifts¹³. After noise, the cochlear lateral wall show signs of edema and the endocochlear potential is reduced^{118,119}, both of which are associated with NIHL.

From our studies in Chapter 4, we found that knocking out *qkl* in young-adult mice caused glial dysfunction which led to dysmyelination and reduced hearing function, mainly through slowing of AN conduction velocity. We showed that in the young-adult AN, *qkl* and the QKI RBPs it encodes are important for maintaining myelination of the type I SGNs. However, the role of *qkl* during AN development is not as clear. The purpose for the studies in this chapter is two parts. First, we wanted to determine the effects of primary glial dysfunction via induced *qkl* KO on AN structural and functional development and maturation. Second, we wanted to elucidate the role of *qkl* around the critical period of AN myelination by determining the effects of its depletion on formation of myelin, nodal assembly, and auditory functional development/maturation by knocking it out pre-peak myelination and during peak myelination. Our findings in this

chapter would demonstrate the importance of normally functioning glial cells for proper AN function and elevate the AN glial cells and *qkl* as valid therapeutic targets in SNHL.

5.2 Specific methods

5.2.1 Animals used

CBA/CaJ mice aged P3 and P7 were used for AN harvesting and subsequent RNA-seq from total AN RNA. These data sets were the same as the ones used in Chapter 3. We also compared myelin and axonal ultrastructure acquired from TEM of P3 and P7 CBA/CaJ mice. To analyze the effects of QKI depletion in auditory glial cells, *QKI^{FL/FL;PLPCreERT}* (QKI-KO) pups were used with Cre-negative littermate controls (QKI-Ctrl). The TAM-induced knockout of *qkl* were generated via intraperitoneal injections of 10mg/ml TAM for 2-3 consecutive days starting at either P5 or P7. P5 was chosen to elucidate the effects of QKI-KO pre-peak myelination (Group 1) and P7 was chosen to elucidate the effects of QKI-KO during peak myelination (Group 2). We chose P5 to represent the pre-peak myelination time point instead of P3 because the survivability of the pups injected at P3, no matter the genotype, was less compared to P5. Due their larger size, P5 mice were more accurately injected with the correct amount of TAM and had less, if any, back flow of TAM solution from the injection site. After

induction, we measured ABR and collected ANs at two endpoints: P14 which is around the onset of hearing and P20/21 which, based on our studies in Chapter 3, is around the period when the AN is functionally mature. See **Figure 5.3.2 A** for the experimental schematic.

5.2.2 RNA-seq analyses of expression of glia-related genes and putative QKI target genes in development

The list of putative QKI-RBP target genes^{59,140} used in Chapter 4 were modified to be compatible with RNA-seq data sets and are used in these studies. In order to find genes possibly affected by *qki* KO at either pre-peak or peak myelination, we compared differential expression of putative QKI-RBP target genes in P3 compared to P7 RNA-seq datasets ($P > 0.05$, Student's t-test, unpaired, two-tailed). The FDR for this analysis after 1000 permutations was 1.7%. To narrow our list of DE genes for each time point, we sorted the genes by greatest absolute fold change (fc) per time point. We then looked at the top 15 up-regulated genes for each period and performed enrichment analysis via DAVID on the combined list to find the top biological processes associated with the list.

5.3 Results

5.3.1 Transcriptomic analyses of putative QKI targets pre-peak and during peak myelination

Based on literature^{56,57,59,128} and our own studies in Chapter 4 showing *qkl*'s presence in the AN, specifically in the auditory glial cells (**Figure 4.3.4**) and their importance for myelin maintenance, we decided to use the inducible *qkl* KO mouse, *QKI^{FL/FL};PLP^{CreERT}*, as our model for developmental dysmyelination in the AN. Our next task was to determine which day(s) may be best for inducing the KO. Our RT-qPCR analysis in **Figure 4.3.4 a** shows that the *qkl* isoforms were all present in P3 and P7. It is of interest to us that *qkl-7* is significantly differentially expressed between P3 and P7 ANs. Along with *qkl-6*, the *qki-7* isoform which encodes the QKI-7 RBP is important for promoting SC myelination⁵⁸. It is also the isoform we have shown to be significantly differentially expressed after one day post-noise injury (**Figure 4.3.3**) and may be associated with the dysregulated expression of the QRE-containing targets after noise. Previous studies¹⁷¹ and our own findings (**Figure 3.3.1 A, Figure 5.3.1 A,B**) show that the onset of myelination in mouse AN occurs at around P3 and that peak myelination activity occurs at around P7. In Chapter 3, we showed that genes that were important components of myelin, which are also markers of mature, myelinating SCs^{27,94,95}, and those that were associated with myelin maintenance^{92,93,97,172} were upregulated at P7 (**Figure 3.3.1 A**).

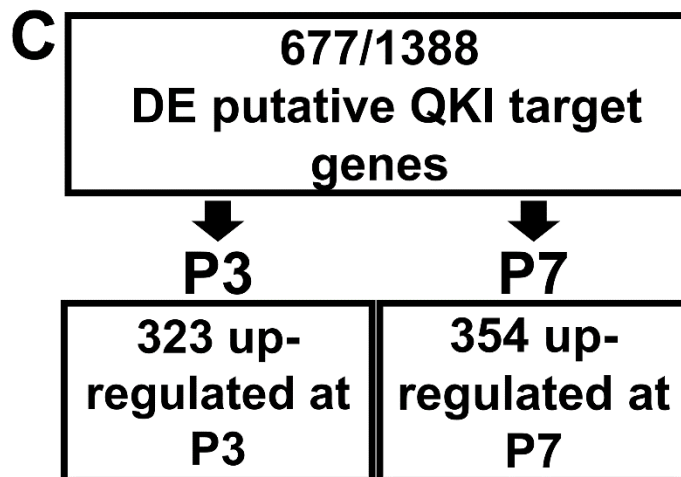
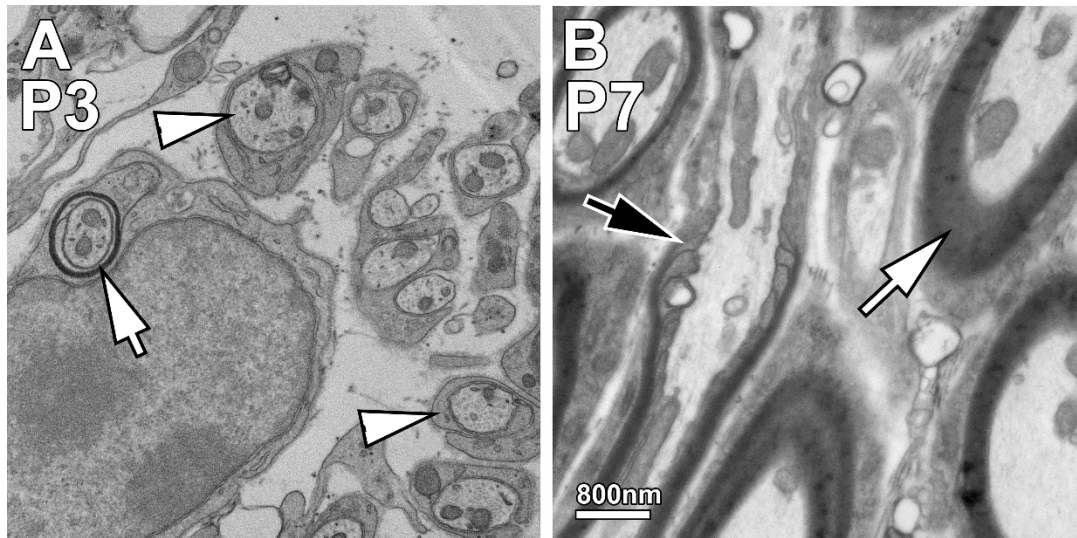


Figure 5.3.1: Differences in the state of myelination and expression of putative QKI-RBP target genes in ANs between pre-peak and peak myelination

This part of the study uses data acquired from postnatal CBA/CaJ mouse mouse ANs. **A** shows a representative image of P3 AN fibers, which are currently undergoing the beginnings of myelination. White arrowheads point to axons enwrapped by one layer of cytoplasm-dense SC processes which represent the myelination state of the majority of the AN fibers. The white arrow points to one of the few axons ensheathed by compact, multi-layered myelin. **B** shows a representative image of P7 AN fibers during the peak myelination stage. The majority of the fibers are densely myelinated. A representative myelinated fiber is marked by a white arrow. The black arrow indicates forming axo-glial connections in the paranodal domain. **C** is a schematic showing that 677 of the 1388 putative QKI-RBP target genes were DE between P3 and P7. 323 of the targets were up-regulated in P3 and 354 of the targets were up-regulated in P7.

Here, we show a representative TEM image of the CBA/CaJ mouse AN fibers at P3, the majority of which are only surrounded by one layer of cytoplasm-filled SC process and one fiber of only few with compact, multi-lamellae myelin sheaths (**Figure 5.3.1 A**). At P7, most of the AN fibers are ensheathed by dense, compact myelin (**Figure 5.3.1 B**). The axo-glial connections between the terminal myelin loop layers and axolemma of the paranodal domains are being formed.

In order to have a better molecular understanding of knocking out QKI around the critical myelination time point in early postnatal development, we queried the expression of putative QKI target genes containing QREs in our CBA/CaJ postnatal RNA-seq datasets (**Figure 5.3.1 C**). We compared the two time points P3 which we chose to represent pre-peak myelination, and P7 which we chose to represent peak myelination. For our differential expression analyses, we found that 677 of the 1389 putative QKI gene targets were differentially expressed between P3 compared to P7 ($p < 0.05$, Student's t-test, unpaired). We chose to look at the genes that have the largest differential expression, so we showed the Top 15 Up-regulated Genes in P3 compared to P7 and the Top 15 Up-regulated Genes in P7 compared to P3 (**Table 5.3.1**). Each list of 15 were acquired via ranking of absolute fold change. The genes were the subsequently sorted by significance. Using gene enrichment analysis via DAVID, we found that the top biological processes represented by the 30 combined genes were immune response-related[†] and myelination-related*.

Table 5.3.1: Top differentially expressed putative QKI target genes

Top 15 Up-regulated putative QKI target genes in P3 compared to P7			
Symbol	Name	FC	P value
Tgtp1[†]	T cell specific GTPase 1	16	0
Il7[†]	interleukin 7	11	0
Tgtp2[†]	T cell specific GTPase 2	15	0.001
Magel2	melanoma antigen, family L, 2	6	0.001
Ccr3	chemokine (C-C motif) receptor 3	6	0.001
Cd28[†]	CD28 antigen	5	0.002
Col10a1	collagen, type X, alpha 1	23	0.009
C1qtnf3	C1q and tumor necrosis factor related protein 3	5	0.01
Chrna6	cholinergic receptor, nicotinic, alpha polypeptide 6	16	0.01
Cxcl9[†]	chemokine (C-X-C motif) ligand 9	63	0.01
Irf7	interferon regulatory factor 7	-6	0.01
Isg15	ISG15 ubiquitin-like modifier	7	0.01
Gbp2	guanylate binding protein 2	5	0.03
Krt71	keratin 71	7	0.04
Ndst4	N-deacetylase/N-sulfotransferase 4	4	0.04
Top 15 Up-regulated putative QKI target genes in P7 compared to P3			
Symbol	Name	FC	P value
Gcg	glucagon	5	0
Mbp*	myelin basic protein	3	0
Mal*	myelin and lymphocyte protein	3	0
Gjb1	gap junction protein, beta 1	3	0.001
Ugt8a*	UDP galactosyltransferase 8A	3	0.001
Galr1	galanin receptor 1	5	0.001
Krt12	keratin 12	3	0.002
Myl1	myosin, light polypeptide 1	3	0.002
Plp1*	proteolipid protein 1	3	0.007
Ear1	eosinophil-associated, ribonuclease A family, member 1	3	0.009
Otop1	otopetrin 1	4	0.01
Il23a[†]	interleukin 23, alpha subunit p19	4	0.01
Mobp	myelin-associated oligodendrocytic basic protein	6	0.01
Emilin2	elastin microfibril interfacier 2	3	0.01
Cyp26a1	cytochrome P450, family 26, subfamily a, polypeptide 1	3	0.02

***Myelination-related genes**

[†]Immune-response-related gene

Our differential expression analyses of the putative QKI-RBP target genes indicate that knockout of QKI at pre-peak or peak myelination can affect different groups of target genes leading to diverging phenotypic consequences. After looking at the molecular and ultrastructural characteristics of the pre-peak myelination and peak myelination time points in CBA/CaJ mouse AN, we chose to induce *qkl* KO either beginning at P5 (Group 1) or at P7 (Group 2). The P5 time point was chosen to represent pre-peak myelination group in order to increase viability of the TAM injected pups.

5.3.2 Abrogation of QKI RBP expression in myelinating glial cells after knockout of *qkl* gene

After looking at the molecular and ultrastructural characteristics of the pre-peak myelination and peak myelination time points in CBA/CaJ mouse AN, we chose to induce *qkl* KO either beginning at P5 (Group 1) or at P7 (Group 2). The P5 time point was chosen to represent pre-peak myelination group in order to increase viability of the TAM injected *QKI^{FL/FL};PLP^{CreERT}* and littermate control pups. The *Plp1* promoter in the *PLP^{CreERT}* mouse used to for the *qkl* deletion was shown to be present in SGCs and SCs of mouse ANs¹⁴. In Chapter 4 (**Figure 4.3.4**) we showed that Pan-QKI is expressed in AN SCs and SGCs. Based on Pan-QKI and *Plp1* protein expression, the *QKI^{FL/FL};PLP^{CreERT}* model should only deplete *qkl* in AN glial cells. **Figure 5.3.2 A** shows a schematic indicating the experimental timeline.

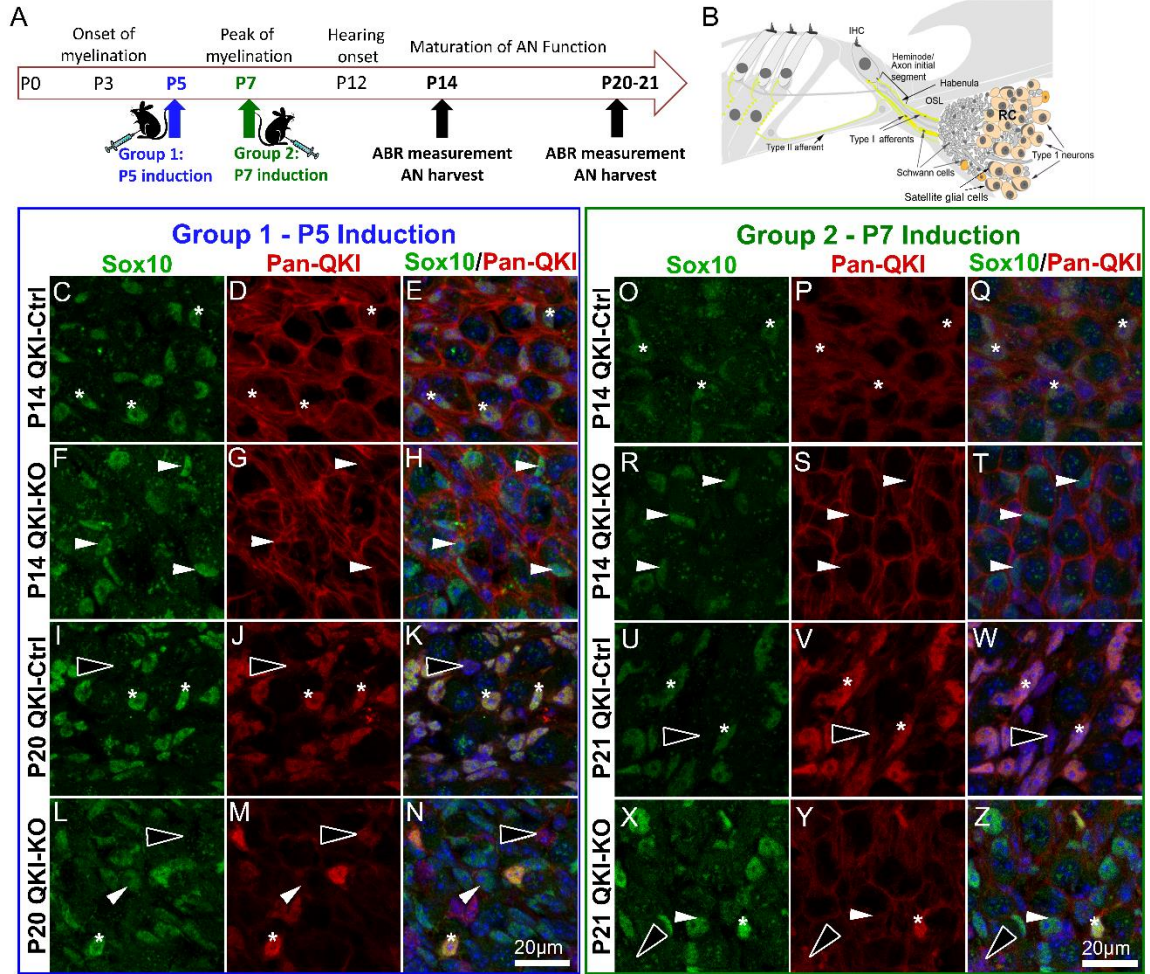


Figure 5.3.2: Abrogation of QKI RBP expression in myelinating glial cells after knockout of *qkl* gene

A The schematic shows the induction time points for the *qkl* KO and experimental outline for the following experiments. Group 1 included mice that were injected at P5 (pre-peak myelination). Group 2 included mice that were injected at P7 (during peak myelination). The groups were then further divided – animals from each group were tested for ABR and their ANs were harvested at either P14 or P20/21. **B** This is a schematic of a cochlear section showing the main components of the auditory nerve. **C-Z** These panels show effect of *qkl* KO for subjects from Group 1 (**C-N**) and Group 2 (**O-Z**). Cochlear sections were stained with Sox10 (green) to indicate SCs and SGCs, Pan-QKI (red) antibody was used to stain for all QKI-RBPs, and nuclei were counterstained with DAPI (blue). **C-E** and **O-Q** show presence of Pan-QKI in Sox10⁺ glial cells in P14 QKI-Ctrl mice from either induction group. Asterisks indicate representative cells with Sox10/Pan-QKI expression. **F-G**, **R-T** show ablation of Pan-QKI in Sox10⁺ glial cells in Group 1 (**F-G**) and Group 2 (**R-T**) P14 QKI-KO. White arrowheads indicate representative glial cells that have no Pan-QKI reactivity. **I-K**, **U-W** show presence of Pan-QKI in Sox10⁺ glial cells in Group 1 P20 (**I-K**) and Group 2 P21 (**U-W**) QKI-Ctrl ANs. White arrow heads indicate Asterisks indicate representative cells that are Sox10⁺/Pan-QKI⁺. Black arrowheads indicate representative cells in the AN that are Pan-QKI⁺, but not Sox10⁺. **L-N**, **X-Z** show abrogation of Pan-QKI expression in Group 1 P20 (**L-N**) and Group 2 P21 (**X-Z**) QKI-KO Sox10⁺ cells. White arrowheads indicate representative glial cells that have ablated Pan-QKI expression. Asterisks mark the few Sox10⁺/Pan-QKI⁺ cells in the ANs. Black arrowheads point to Pan-QKI⁺ cells that are not glial cells.

We measured ABRs and collected ANs from each group at P14, which is around the onset of hearing, and at P20/21, which is around the period when the AN should be functionally mature based on our studies in Chapter 3. **Figure 5.3.2 B** shows a cartoon of a cochlear section highlighting the regions of interest for our study. Most of our confocal and TEM images were focused on the Hab, OSL, and RC regions of the AN.

Before proceeding with our morphological and physiological studies, we needed to investigate the effectivity of our *qkl* KO in the AN glial cells. We performed co-immunostaining experiments with anti-Sox10 and anti-Pan-QKI, which detect all QKI variants, on our P14 and P20/21 cochlear sections. Sox10 is a marker for both SCs and SGCs¹⁵¹ in the AN. Immunohistochemical analyses show that the *qkl* KO was successful in depleting QKI-RBPs in P14 and P20/21 AN glial cells for both QKI-KO groups compared to littermate QKI-Ctrls. In the P14 QKI-KO, presence of QKI-RBP in both SCs and SGCs were ablated for both groups (**Figure 5.3.2 C-H; O-T**). For the P20/21 animals for both groups, most of the Sox10⁺ cells in the AN had no reactivity for anti-Pan-QKI (**Figure 5.3.2 I-N; U-Z**). There were only few Sox10⁺ cells in the AN that were positive for QKI-RBP expression. Based on our findings in Chapter 4, we concluded that these were SGCs and not SCs. In the KO animals, the few Sox10⁺ cells that were Pan-QKI⁺ were only present in the RC and not the OSL, and their morphology and attachment around the SGN somata indicate that these were SGCs. We also saw cells that were Pan-QKI⁺ but are negative for anti-Sox10 reactivity. We concluded that these were not type I SGNs as supported by previous literature¹²⁸

and because of the differing morphological characteristics between the cells that are Sox10⁻/Pan-QKI⁺ and SGNs. Other cells that reside among the SGNs and glial cells, which these Sox10⁻/Pan-QKI⁺/DAPI⁺ cells may be, include macrophages (as we show in Chapter 4 and **Figure 5.3.4-6**) and fibroblasts¹⁷³. Co-immunostaining of Pan-QKI with macrophage and fibroblast markers could be executed in future experiments to identify these cells. These findings show that our *qkl* KO and the subsequent depletion of QKI-RBP variants in both groups was sufficiently effective.

5.3.3 Developmental-stage dependent QKI-KO induces hypomyelination or dysmyelination of AN fibers at P14

The best way to visualize the effects of the *qkl* KO in the QKI-KO AN compared to QKI-Ctrl is to look at the ultrastructure via TEM. In this way, we could determine the consequence of the KO on the ability of the auditory glial cells to myelinate the AN fibers and somata. We first looked at the AN ultrastructures at the P14 endpoint. As we saw in association with the node studies in Chapter 3, the SGN fibers and, to a lesser extent, the somata, are ensheathed by compact, multi-layered myelin by P14 in parallel with the onset of hearing. Here we show that the QKI-Ctrls for Group 1 (**Figure 5.3.3 A-C**) and Group 2 (**Figure 5.3.3 G-H**) have dense myelination around their axons and have at least one layer of myelin lamella around their somata. We found in our studies in Chapter 3 that myelination around the somata by the SGCs is slower compared to myelination of the axons by the SCs.

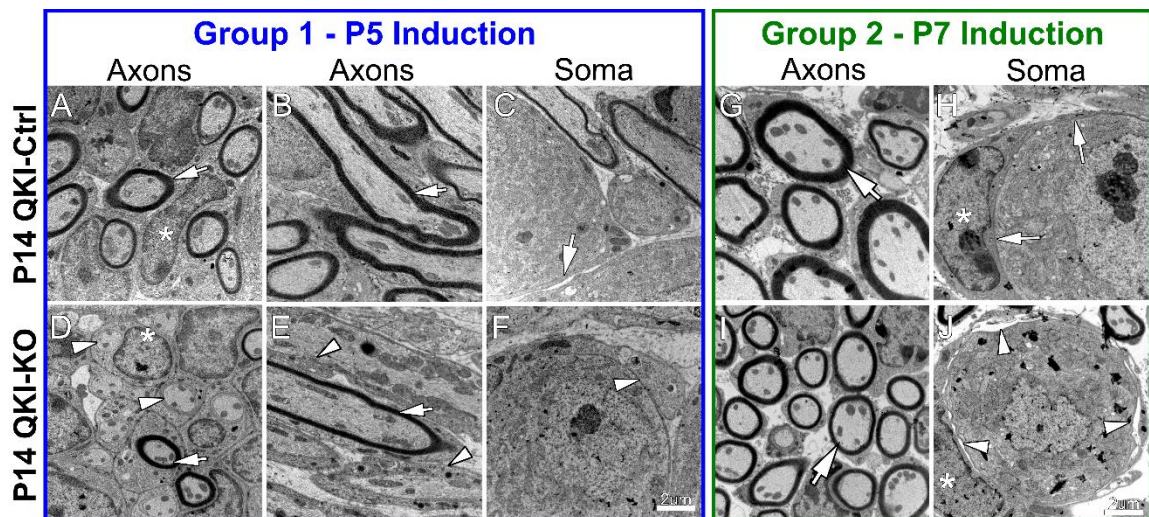


Figure 5.3.3: Developmental-stage dependent QKI-KO induces hypomyelination or dysmyelination of AN fibers at P14

The majority of AN fibers and soma lack dense myelination in P14 QKI-KO ANs (**D-F**) compared to littermate controls (**A-C**) when QKI deficiency is induced at P5. Compact myelin enwraps P14 QKI-KO axons when deficiency is induced at P7 (**I**), but dysmyelination occurs at the soma (**J**) compared to Group 2 littermate controls (**G,H**). **A-F** Ultrastructure of AN fibers in P14 QKI-Ctrl (**A-C**) and P14 QKI-KO (**D-F**) induced at P5. Transverse (**A, D**) and coronal (**B, E**) sections of type I SGN axons in OSL and soma (**C,F**) in RC. **A,D** Asterisks indicate SCs; white arrows indicate densely myelinated fibers. **D** White arrowheads indicate representative axons wrapped by a layer of cytoplasm-filled SC process. **B** A white arrow points to a representative axon that is densely myelinated. **E** White arrowheads indicate axons each ensheathed by single SC layer. A white arrow marks an example of the small number of densely myelinated fibers. **C** A white arrow shows a condensed myelin layer surrounding QKI-Ctrl soma. **F** A white arrowhead shows cytoplasm-filled SGC process wrapping around QKI-KO soma. **G-H** Ultrastructure of AN fibers in P14 QKI-Ctrl (**G,H**) and P14 QKI-KO (**I,J**) induced at P7. **G,I** show densely myelinated axons present in both QKI-Ctrl and QKI-KO. White arrows indicate representative fibers with dense myelination. **H** White arrows mark compact myelin layers surrounding QKI-Ctrl soma. **J** White arrowheads mark a loose myelin layer detaching from the soma; asterisks indicate SGC in **H,J**.

The reduction of cytoplasm within the ensheathing myelin lamella, as we see around the somata in **Figure 5.3.3 C** and **H**, is a sign of compact myelin development¹⁷⁴. In stark contrast to the QKI-Ctrls, we saw prevalent hypomyelination of the axons (**Figure 5.3.3 D-E**) and somata (**Figure 5.3.3 F**) in the Group 1 P14 QKI-KO. The majority of the Group 1 QKI-KO axons were wrapped only by thick, cytoplasm-filled SC processes. Only few axons were ensheathed by compact myelin. The membranes of somata were covered by a single thick SGC processes, if at all. The *qki* KO in P5 has impaired glial function. The under-developed myelin around these SGNs can either indicate that myelination during early postnatal AN development is delayed in Group 1 QKI-KO or if hypomyelination persists in later time points, glial dysfunction may be more severe.

Contrary to our findings in Group 1 QKI-KO, the axons of the Group 2 QKI-KO are densely myelinated (**Figure 5.3.3 I**) similar to their QKI-Ctrl counterparts. Upon closer visual inspection of our TEM image sets showing transverse sectioning of the fibers, however, we could argue that the dense myelin around the QKI-KO animals may be thinner compared to QKI-Ctrl. To solidify this suspicion, we will complete G ratio measurements for this group, as divergence from the optimal G ratio (~0.6 in PNS fibers) are associated with aberrant conduction¹⁷⁵⁻¹⁷⁷. In contrast to the subtle differences myelin difference between Group 2 QKI-KO and QKI-Ctrl, *qki* KO-induced dysfunction of the SGCs is clearer. In **Figure 5.3.3 J**, the enwrapping myelin is looser and detaching from the soma in several places in the QKI-KO. Dysmyelination around the somata

strongly implies that *qkl* KO in P7 affects the glial cells' ability to maintain myelination as opposed to the *qkl* KO in P5 which may affect the glial cells' ability to create myelin.

5.3.4: *qkl* KO at P5 leads to chronic hypomyelination and morphologically abnormal SCs

We continue our ultrastructural studies by analyzing at the effects of *qkl* KO in pre-peak myelination P5 at a later endpoint. The period around P20-21 is associated with AN structural and functional maturation. Very recent studies have shown that type I SGN differentiation into their mature subtypes, which are associated with their distinguishing firing properties, occur at around the third postnatal development week^{105–107}. As we have reviewed in Chapter 1, these SGN subtypes have different SRs that contribute to the canonical wave I response seen in functionally mature ANs^{8,9,104} (i.e., the ability of the different subtypes to be recruited for a greater summed response at higher intensity stimulation and the continued response of high SR fibers in low intensity stimuli). Previous studies⁸⁶, along with our own, (Appendix A-1) show that threshold and suprathreshold measurements of amplitude and latency from mice \geq P18 are comparable to those of young-adults.

In these studies, we show that hypomyelination of the SGN axons and somata persist at P20 in the QKI-KOs compared to QKI-Ctrls.

Group 1 P5 Induction

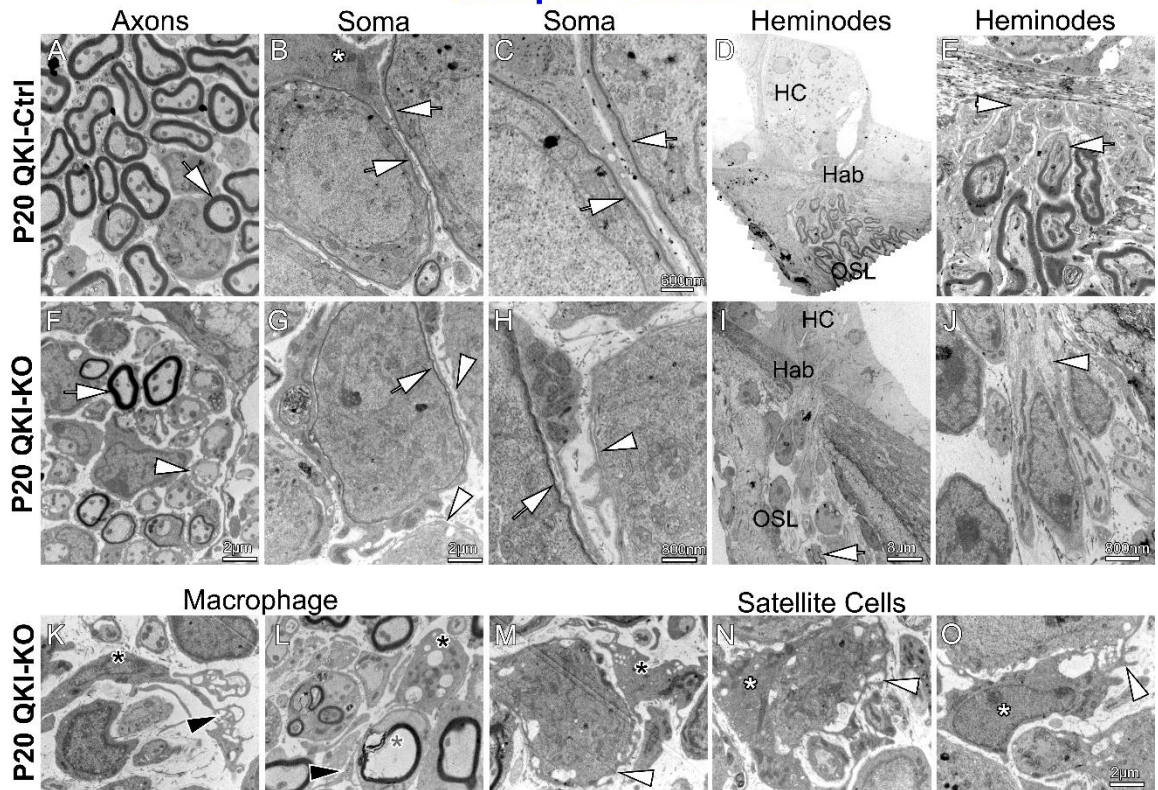


Figure 5.3.4: *qkl* KO at P5 leads to chronic hypomyelination and morphologically abnormal SCs

The majority of AN fibers and soma in Group 1 mice with *qkl* KO induced at P5 were still hypomyelinated compared at P20 (**F-J**) compared to their littermate controls (**A-E**). **A** shows a white arrow pointing to one densely myelinated AN fiber in QKI-Ctrl. This is representative of the fiber population in the QKI-Ctrls. **F** shows a white arrowhead indicates a representative hypomyelinated fiber in QKI-KO. A white arrow points to one of the few densely myelinated fibers. **B** and the enlargement **C** show a SGN somata that are enwrapped by multiple layers of SGC myelin. The white arrows point to the dark, electron-dense myelin lamellae. **G** shows multiple hypomyelinated somata in QKI-KO. The white arrowheads indicate two somata enwrapped by a few layers of cytoplasm-dense SGC processes. The white arrow points to one of the small number of somata that are ensheathed by multiple layers of myelin. The enlargement **H** highlights the two layers of SGC processes enwrapping a soma compared to the dark, electron-dense myelin lamellae enwrapping another soma. **D,E** and **I,J** show heminodes at the habenula in QKI-Ctrl (**D,E**) and QKI-KO (**I,J**) ANs. The heminodes of control AN are densely myelinated on their processes running along the OSL. The enlargement **E** further highlights thick myelination. A white arrow indicates an example heminode and its associated paranodal domain. A white arrowhead points to an example fiber that is naturally unmyelinated after the heminode in order to easily pass through the hab to synapse with the HC. Compared to control, the QKI-KO at the habenula shows many fibers that are only ensheathed by one SC process (**I**). The white arrow points to a heminode of one myelinated AN fiber. Notice how far this heminode is from the habenula compared to the heminodes in **D**. The enlargement **J** highlights the thoroughly hypomyelinated fibers (white arrowhead marks a representative fiber) which do not have heminodes, much less paranodal domains. **K,L** highlight the presence of macrophages in P20 QKI-KO. The black asterisk in **K** marks the nucleus of a macrophage with many ramification (black arrowhead). The black asterisk in **L** indicates an ameboid-shaped macrophage filled with multiple vesicles. The black arrowhead points to a macrophage process approaching an apoptosed SGN fiber (grey asterisk) that also shows signs of dysmyelination. Panels **M-O** show examples of morphologically abnormal SGCs. The white arrowheads indicates detachment of the SGC processes from the somata, which also appear to have multiple leading ends proceeding away from the somata membranes (especially highlighted in **O**). The black asterisk in **M** is an example of an ameboid-shaped macrophage next to a soma. Notice the similar morphology of this macrophage with the SGC cell bodies in **N** and **O**.

In contrast to the thickly sheathed axons of QKI-Ctrl (**Figure 5.3.4 A**), the majority of the axons of QKI-KO are still only enveloped by a cytoplasm-filled SC process (**Figure 5.3.4 F**). Although there are axons with multi-layered myelin, only a small number of them match the myelin volume seen in controls. Comparison between fiber myelination here and in P14 QKI-KO (**Figure 5.3.3 D**) may indicate that the *qkl* KO may lead to further decline in axo-glial attachment. The lone SC process surrounding the axon in P20 QKI-KO are not snugly apposed to the axolemma and spaces of separation are visible. Most of the SGN somata in QKI-KO are also shrouded by few layers of compact myelin or a few turns of SGC processes with condensed cytoplasm (**Figure 5.3.4 G, H** enlargement) compared to the dense myelination of control somata (**Figure 5.3.4 B, C** enlargement). The enlargement in **Figure 5.3.4 H** highlights one of the small number of somata enwrapped by multi-layered myelin and the prevalent state of SGC myelination seen in QKI-KO, which is shrouding of somata by non-compact SGC processes/lamellae. This can be defined as a sort of “intermediate/immature” myelination, where the SGC processes have expelled their cytoplasm in preparation for tight compaction of the layers.

We also looked at the habenular region where the heminodes reside and cluster. In normal mice and in the controls we show here (**Figure 5.3.4 D, F** enlargement), the SC most distal to the somata terminates its myelination of the axon at the heminodal paranode, which is located towards the OSL. After the heminode, the SGN is naturally un-myelinated in order to pass through the small opening of the hab to synapse with the IHC. The most distal SCs still provide

thick myelination to the axons at the end of the OSL prior to the hab opening. Clustering of heminodes at the hab reveal many excitable heminodal domains/axon initial segments and termination of the myelin lamellae at the heminodal paranode domains. We show that the P20 QKI-KO have largely hypomyelinated fibers at the hab, as no heminodal paranodes are visible at the opening (**Figure 5.3.4 I, J** enlargement). Clustering of heminodes may also be abnormal as one of the few fibers with a visible heminodal paranode is much further out into the OSL compared to QKI-Ctrl.

Ultrastructural analyses of Group 1 ANs also revealed ubiquity of cochlear macrophages (**Figure 5.3.4 K,L**). The macrophages present had different morphologies. Some were elongated and had multiple ramified processes (**Figure 5.3.4 K**). Others were ameboid-shaped and were filled with multiple clear vesicles (possibly lysosomes) and had many dark organelles (possibly mitochondria) (**Figure 5.3.4 L**). Macrophages are naturally present in the cochlea to phagocytose debris. Similar to CNS microglia, resident macrophages present among the SGNs have a ramified appearance, which are attributed to their surveying of the environment for debris¹⁷⁸⁻¹⁸⁰. These elongated, ramified macrophages are thought to be in a “resting” state. Recruitment and infiltration of macrophages can occur in the cochlea after injury, as others have found^{143,146} and as we have shown in Chapter 4. “Activated” macrophages phagocytosing debris and apoptotic cells have been characterized as having an “ameboid-shape^{178,181}.” Aside from macrophages, SCs also function to clear debris in the PNS via autophagy and phagocytosis^{182,183}. In **Figure 5.3.4 L**, we see an SC that

has phagocytosed multiple myelin whorls and diseased axons, while also functioning to shroud a healthy, large diameter axon.

Our studies also reveal that SGCs juxtaposed to the somata have abnormal morphology (**Figure 5.3.4 M-O**) compared to those seen in QKI-Ctrl. Instead of being closely conformed and attached to the somata, these SGCs take on a globular, un-healthy-looking appearance. At times it may be hard to distinguish them from activated cochlear macrophages, as evidenced in **Figure 5.3.4 M**. These SGCs are more detached from the somata and have processes spreading away from the soma membrane. These processes may simply be detaching from each other or the soma membrane due to lack of glial-glial or glial-soma adhesion molecules. Another explanation could be that they may be responding to and being attracted towards an environmental signal, similar to how macrophages respond to cytokines.

5.3.5 Eventual dysmyelination of type I SGN fibers and somata in P21 after *qki* KO at P7

In parallel with our ultrastructural studies for Group 1, we analyzed P21 QKI-KO in comparison with age-matched QKI-Ctrl. Our QKI-Ctrl had thick myelination around the axons (**Figure 5.3.5 A**), and around the soma (**Figure 5.3.5 B, C enlargement**). In contrast, we observed a range of myelination around the QKI-KO axons (**Figure 5.3.5 D**). Some maintained their dense, compact myelin, while many were shrouded by a single layer SC process. Dysmyelination of some SGNs is evidenced by visible separation within compact

myelin layers. There were also signs of SGN degeneration, as shown by a thin myelin layer surrounding a large empty space where a fiber should be. The size of the space, in comparison to the diameter of surrounding axons, as well as the roundness of the remaining myelin, imply that the space may be edematous. SGN abnormalities can also be indicated by the presence of abnormally abundant dark vacuoles/organelles within the cytoplasm, implying that axonal transport mechanisms could be compromised⁶⁴. The majority of the somata were not enwrapped by multi-layered, compact myelin compared to QKI-Ctrl. Dysmyelination of the somata (**Figure 5.3.5 E, F enlargement**) has also worsened in P21 QKI-KO compared to P14 QKI-KO (**Figure 5.3.3 J**). Separations between SGC myelin lamellae and detachment from the soma membrane are apparent.

Disruption of the axo-glial connections at the paranodal domains in P21 QKI-KO was also present (**Figure 5.3.5 G,H**). Compared to the paranodal structure seen in QKI-Ctrl (**Figure 5.3.5 A**), terminal myelin loop layers had spacious separations between each other. This further implies a possible depletion of glial-glial adhesion molecules. Other terminal myelin loops either lost or had no initial connection to the axolemma or were severely misconnected, as seen in **Figure 5.3.5 H**. This could indicate decreased expression of axo-glial connector molecules or abnormal signaling promoting myelin deposition between the glia and axons during myelin development^{184,185}.

Group 2 - P7 Induction

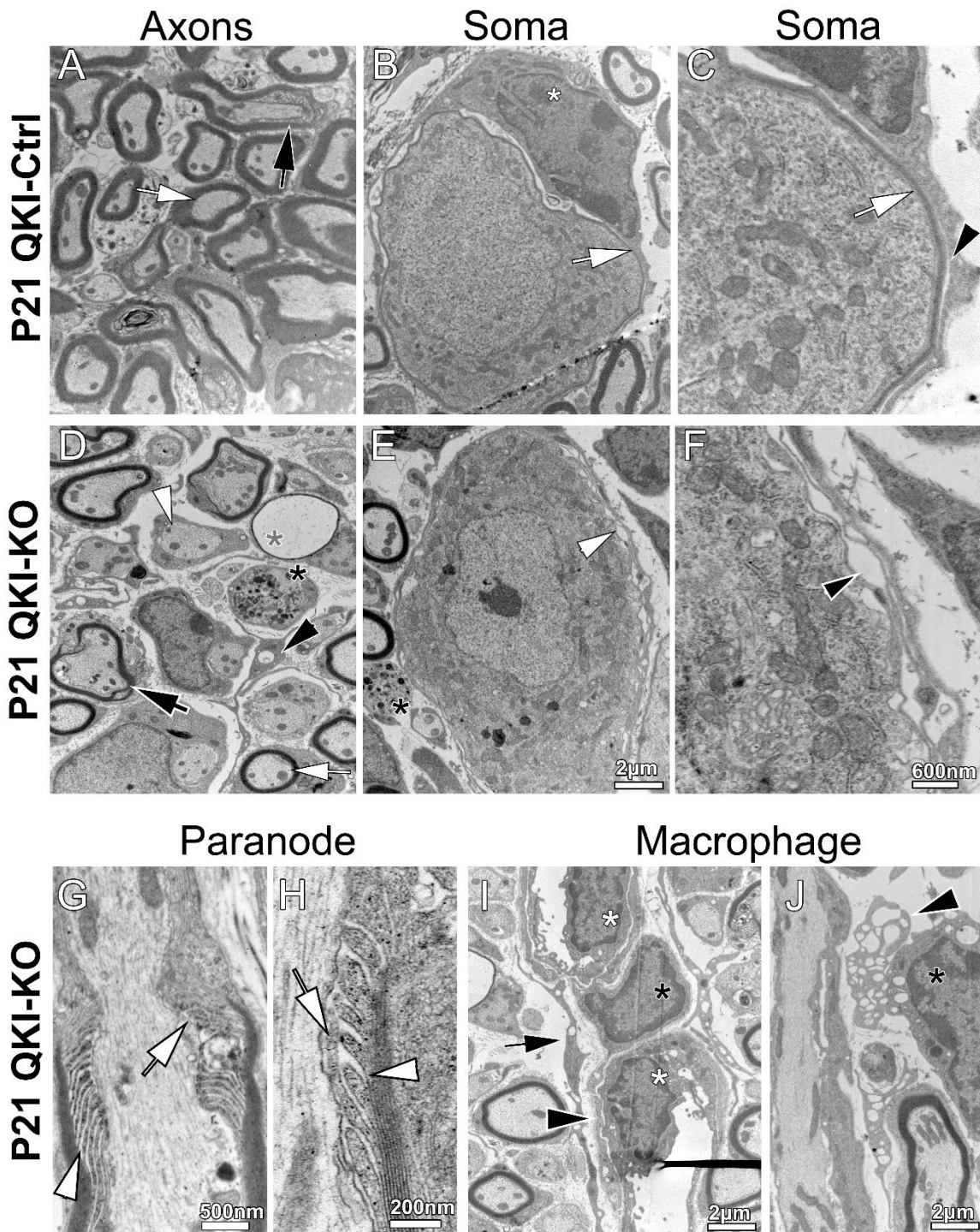


Figure 5.3.5: Eventual dysmyelination of type I SGN fibers and somata in P21 after *qkl* KO at P7

Dysmyelination of the fibers and somata are evident in the Group 2 P21 QKI-KO mice (**D-F, G-H**) compared to the densely myelinated type I SGNs in QKI-Ctrl (**A-C**). **A** is a representative image showing that the majority of the QKI-Ctrl fibers are ensheathed by multiple layers of compact myelin. The white arrow points to a representative densely myelinated fiber. A black arrow points to a paranodal domain with multiple, snugly apposed terminal myelin loops connected to the axolemma. **D** shows multiple QKI-KO AN fibers with different stages of myelination. A white arrow indicates a myelinated fiber. A white arrowhead points to a fiber ensheathed with a single layer of thick SC process. A black arrow indicates a fiber with abnormal separations within its compact myelin. A grey asterisk points to a thin myelin layer enwrapping a space where the fiber process of an apoptosed SGN resided. A black asterisk marks an example of an SGN fiber filled with small, dark, electron-dense vacuoles. **B** and the enlargement **C** shows an example of a control soma with multi-layered myelin (highlighted with white arrows) that is further surrounded by a thicker layer of SGC process (black arrowhead in **C**). (**E, F**) Compared to control, the soma of QKI-KO fibers are surrounded by fewer SGC lamellae (indicated by white arrowhead in **E**) that are also detaching from each other (indicated by black arrowhead in **F**), as well as the soma membrane. A black asterisk in **E** highlights another dark vacuole-filled SGN fiber. **G, H** show disruption of the axo-glial connections and glial-glial connections at the paranodal domain compared to the one seen in control (**A**). The white arrowheads point to the abnormal spacing in between terminal myelin loop heads. The white arrow in **G** highlights a loophead detached from the axolemma and the one in **H** points to a loop head that has unusually extended to surface with the axolemma, blocking connections of other terminal loop heads in the process. **I** shows ameboid-shaped macrophages within a blood vessel (white asterisks) and one with long processes (black arrowhead) that has crossed to the RC (black asterisk). The black arrow points to one of the many elongated macrophage processes seen in this panel. **J** shows another ameboid-shaped macrophage (black asterisk) with processes (black arrowhead) approaching an adjacent dysmyelinated fiber.

Similar to findings in P20 Group 1 QKI-KO, Group 2 QKI-KO also revealed ubiquity of cochlear macrophages (**Figure 5.3.5 D,I,J**). These macrophages, which are either ramified or amoeboid in shape, can be found among degenerative SGNs. Macrophages can also be seen coming into the cochlear RC space from the blood vessels (**Figure 5.3.5 I**), which may imply their active recruitment by either the dysfunctional glia or degenerating SGNs. Together with the ultrastructural analyses at P14, these findings show that although myelinating glial cells with *qkl* KO were capable of creating multi-layered myelin around SGNs, they were unable to maintain the myelin integrity at later endpoints.

5.3.6 MBP expression is chronically depleted and Iba⁺ cells are present in great numbers adjacent to dysmyelinated somata in either *qkl* KO group

To elucidate the dysmyelination we saw in the ultrastructure at the molecular level, we performed immunohistochemical studies to with anti-MBP and anti-Iba1. We reviewed in Chapters 1 and 3 the importance of myelin basic protein (MBP), which is one of the main structural components of myelin membranes⁹⁴ and also a marker of matured myelinating glial cells²⁷. *MBP* mRNA contains QREs and is a known target of QKI-RBPs^{56,58,130}. Besides affecting localization of *MBP* mRNA, studies have shown that exogenous QKI-6 introduced into the quaking viable mice binds to *MBP* mRNA and is associated with rescuing myelinogenesis and the maintenance of compact myelin¹³⁰. We used the Iba1 antibody in Chapter 4 to identify cochlear macrophages.

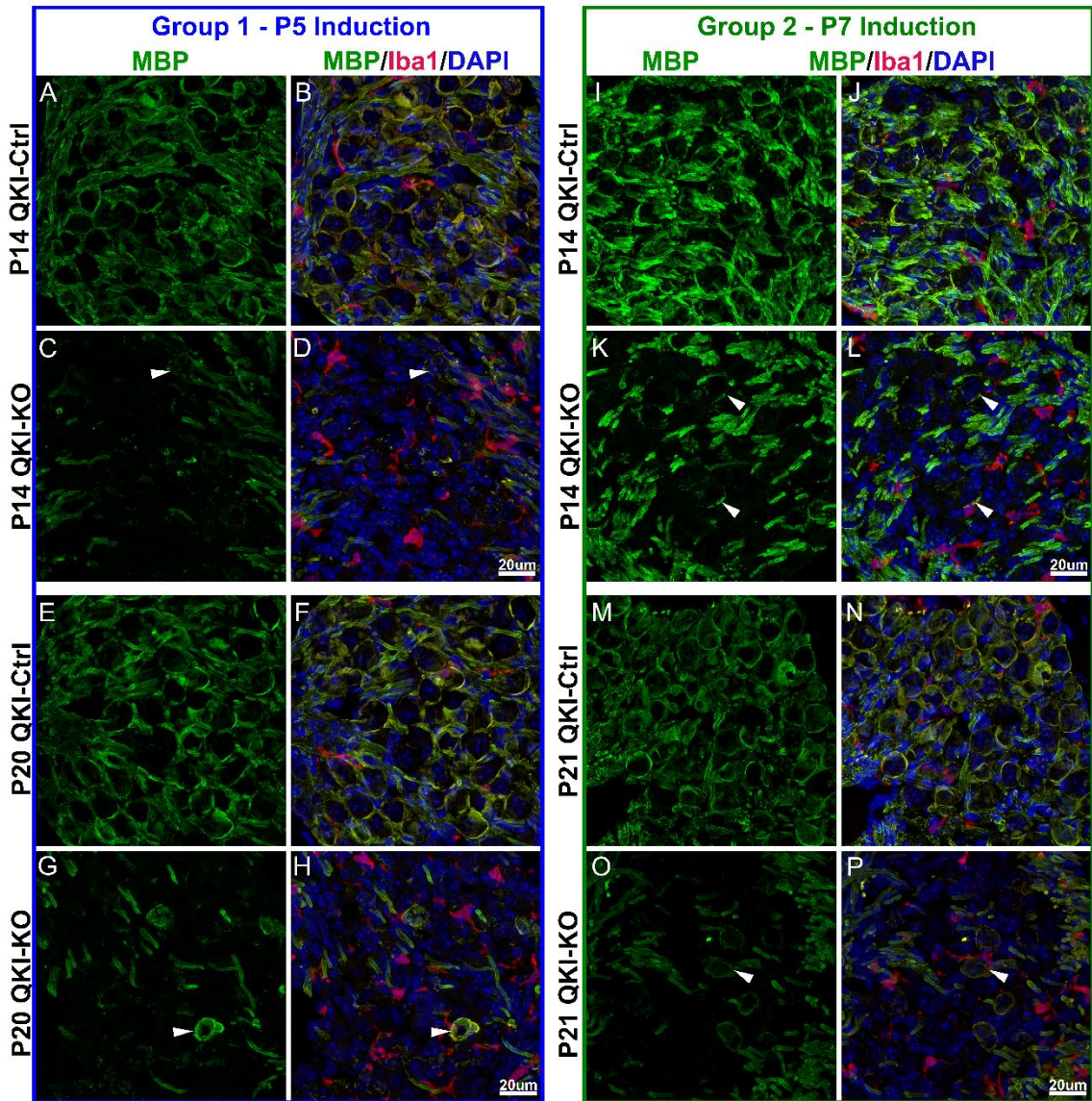


Figure 5.3.6: MBP expression is chronically depleted and Iba⁺ cells are present in great numbers adjacent to dysmyelinated somata in either *qkl* KO group

In both Group 1 and 2, QKI-Ctrls have MBP (green) expression present in both earlier (P14 **A,B; I,J**) and later (P20 **G,H; P21 O,P**) endpoints. MBP is present together with the long axonal processes and surrounding the somata. In the Group 1 P14 QKI-KO (**C,D**), there is almost no MBP surrounding the somata. In Group 2 P14 QKI-KO (**K,L**), MBP expression is a little more apparent in the RC compared to Group 1, but there are no somata surrounded by complete MBP expression. Sparse, disjointed expression of MBP around the somata are indicated by the white arrowheads in **C,D** and **K,L**. (**G,H**) In Group 1 P20 QKI-KO, there is a smaller number of axons that have MBP expression along the axons compared to the age-matched control (**E,F**), as well as to the Group 1 P14 QKI-KO. The white arrowheads in **G,H** indicate one of the few somata surrounded by MBP expression. (**O,P**) In Group 2 P21 QKI-KO, MBP expression continues to be depleted compared to the age-matched control (**M,N**). The white arrowheads in **M,N** indicate one of a small number of somata that are surrounded by MBP expression. Double-labeling with Iba1⁺ macrophages (red) show that both amoeboid and ramified macrophages are present in large quantities in the RC of the QKI-KO ANs at either endpoint for both groups (P14 **D,L; P20/21 H,P**) compared to their controls (P14 **B,J; P20/21 F,N**). The macrophages can be found adjacent to the sparse MBP expression around the somata and juxtaposed to somata not surrounded by MBP. Nuclei are counterstained with DAPI (blue).

Since myelination of axons and somata can be identified at the RC, we chose to focus on that region with our analyses. Our immunostaining experiments reveal that compared to P14 QKI-Ctrls which had MBP expression along the axons and around the somata (**Figure 5.3.6 A,B**), the Group 1 P14 QKI-KOs showed reduced MBP expression along the axons and especially around the somata (**Figure 5.3.6 C,D**). There were few, if any, SGNs that had MBP completely surrounding their somata. Although, disjointed anti-MBP immunoreactivity can be seen around the vicinity of the SGN cell bodies. Group 2 P14 QKI-KO (**Figure 5.3.6 K,L**) had similar MBP expression along their axons compared to their controls (**Figure 5.3.6 I,J**). Around the somata, however, MBP expression was visibly reduced, although not to the same extent as in Group 1.

By the later endpoint at P20/21, MBP expression for both KO groups continue to be depleted surrounding the somata (**Figure 5.3.5 G,H; O,P**) compared to their respective controls (**Figure 5.3.5 E,F; M,N**). Compared to Group 1 QKI-KO, Group 2 QKI-KO had more SGNs with immunoreactivity to anti-MBP encompassing their cell bodies. In Group 1, only a small number of SGN cell bodies that were shrouded by MBP expression. It appears that MBP expression along the axons are also further reduced. To bolster these experimental findings and to determine if *qkl* KO is affecting either *MBP* mRNA translation efficiency or its stability, we could compare levels of *MBP* mRNA in the QKI-KO AN with MBP expression. This could be done via combination of RT-qPCR and western blots or comparing intensities of fluorescent *MBP in situ* with MBP immunofluorescence.

To further our ultrastructural findings pertaining to cochlear macrophages in association with dysmyelination, we performed co-immunostaining for MBP with Iba1. Our findings show that both ramified and amoeboid macrophages are largely present surrounding the SGN cell bodies in QKI-KO at either endpoint for both groups (**Figure 5.3.6 D,H; L,P**). In the QKI-Ctrls (**Figure 5.3.6 B,F; J,N**), macrophages are also visible, but in much lesser quantities. To comment on possible activity, compared to the QKI-KOs, most of these macrophages in QKI-Ctrl have an elongated, ramified shape, which implies that they are in their “resting” state. To extend these studies, we could perform morphometric analyses on these Iba1⁺ macrophages, in which number of processes and cell shape and volume will be measured and compared between QKI-KO and QKI-Ctrl. We can also co-label Iba1 with markers of actively phagocytosing macrophages, such as CD11b and CD68^{79,186–188} to functionally differentiate the macrophages present in QKI-KO compared to QKI-Ctrl.

5.3.7 *qkl* KO caused abrogated Cntn1 expression and disruption of paranodal structures

We saw earlier in the ultrastructural studies shown in **Figures 5.3.4-5** that the integrity of nodal structures were compromised in after *qkl* KO. To further elucidate the effects of *qkl*-KO on the nodal domains and to understand which molecules may be affected, we performed immunohistochemical experiments involving nodal CAM NrCAM and paranodal axo-glial connector molecule Cntn1.

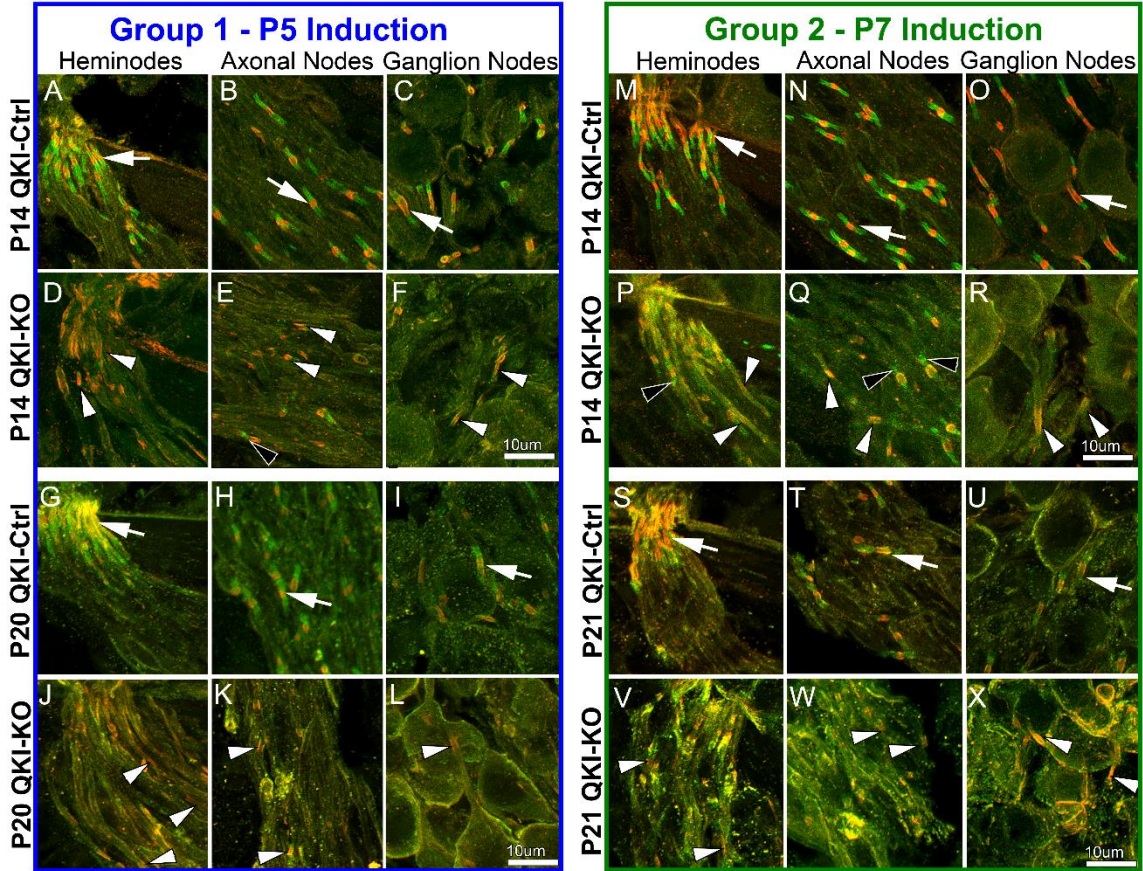


Figure 5.3.7: *qkl* KO caused abrogated Cntn1 expression and disruption of paranodal structures

Immunostaining of nodal NrCAM (red) and paranodal Cntn1 (green) in AN sections from QKI-KO induced at either P5 (**D-F**) or P7 (**P-R**) shows that disruption of paranodal structures of all 3 nodal types is apparent in both experimental groups compared to controls at P14 (**A-C**; **M-O**). The abrogated expression of Cntn1 continues into later development for both QKI-KO groups (Group 1 **J-L**; Group 2 **V-X**) compared to their controls (**G-I**; **S-U**), indicating that disruption at the paranodal domain is also chronic. Throughout this figure, white arrows mark representative, normal paranodal domains with Cntn1 expression at the single paranode of the heminodes (Group 1 **A,G**; Group 2 **M,S**), in paranodal flanks of the axonal nodes (Group 1 **B,H**; Group 2 **N,T**) and at the ganglion paranodes (Group 1 **C,I**; Group 2 **O,U**). For the Group 1 panels, white arrowheads mark representative nodal structures without Cntn1 expression at the paranodes for the P14 endpoint (**D-F**), continuing to the P20 endpoint (**J-L**). The white arrowheads marking the Cntn1⁻ heminodes in **D,J** also highlight the disorganization of heminodal clustering under the IHC, as several of the heminodes are further out into the OSL. Cntn1 expression at the paranodes in Group 2 is not completely abrogated in all paranodes of the heminodes (**P**) and axonal nodes (**Q**) at P14, but are greatly reduced compared to their control counterparts (M,N). Black arrowheads in P,Q indicate paranodes with some presence of Cntn1. For the ganglion paranodes, however, Cntn1 expression is depleted at P14 (**R**), continuing to P21 (**X**) compared to their controls (**O,U**). By P21, Cntn1 expression at the heminodes (**V**) and axonal nodes (**W**) of Group 2 ANs have greatly diminished compared to the age-matched controls (**S,T**) and Group 2 P14 QKI-KO. As with the Group 1 QKI-KO heminodes, the positioning of Group 2 heminodes (highlighted by white arrowheads) show un-clustered and scattered heminodes. Nodal NrCAM expression is intact in P14 QKI-KO for both groups, but by P20/21, their usually cylindrical appearance is harder to distinguish at the heminodes and axonal nodes.

To briefly recap previous literature^{36,189} and our findings in Chapter 3, NrCAM is associated with initiation of formation of the excitable nodal domains and is responsible for binding the scaffolding proteins responsible for VGSC clustering at the node. Axolemmal Cntn1 and Caspr1 work together to bind glial Nfasc155 present at the terminal myelin loop heads to form organized, well-connected axo-glial connections at the paranode^{41,42}. Nfasc155 is a known QRE-containing target of QKI-RBPs and KO of *qkl* has been shown to impair generation of Nfasc155⁵⁹.

To begin, we found that Cntn1 protein is expressed normally in the paranodes of the heminodes, axonal nodes, and ganglion nodes of the QKI-Ctrl at either endpoint (**Figure 5.3.7 A-C, G-I; M-O, S-U**), comparable to their immunofluorescence profiles that we determined in Chapter 3. In Group 1 QKI-KO, Cntn1 expression was completely ablated in the heminode and ganglion node paranodes, while greatly reduced expression can be detected in the paranodal flanks of the axonal node (**Figure 5.3.7 D-F**). At P20, Cntn1 is barely detectable in any paranode (**Figure 5.3.7 J-L**), implying that abrogated Cntn1 expression is chronic.

In the Group 2 P14 QKI-KO, Cntn1 expression is more detectable compared to Group 1 P14 QKI-KO, with Cntn1 present at heminodal and axonal paranodes (**Figure 5.3.7 P-R**). However, expression is still greatly reduced compared to control, and no Cntn1 can be detected at the ganglion paranodes. By P20, Group 2 QKI-KO have no observable Cntn1 in any paranodal type (**Figure 5.3.7 V-X**). Based on our compiled list, *Cntn1* is not a direct target of

QKI-RBPs. However its significant depletion after *qkl* KO strongly suggests that it is at least an indirect target of QKI-RBPs.

Additionally, while anti-NrCAM immunoreactivity is comparable to that of QKI-Ctrls in both P14 QKI-KO groups, its usual cylindrical staining profile is harder to distinguish in heminodes and axonal nodes of both P20 QKI-KO groups. This implies that continued glial dysfunction affects axonal organization or expression of this nodal CAM. Anti-NrCAM staining of the heminodes at the habenula for either group (**Figure 5.3.7 D,J; P,V**) also exemplifies disorganization of the heminodal clusters in QKI-KO compared to controls (**Figure 5.3.7 A,G; M,S**). Unlike in the QKI-Ctrls where anti-NrCAM staining is clustered at the hab, -each QKI-KO panel displays separation of anti-NrCAM immunoreactivity and marks heminodes that are further out towards the OSL. This further suggests dysregulation of NrCAM localization at in the distal portion of the axons towards the hab after *qkl* KO.

5.3.8 *qkl* KO-induced hypomyelination leads to loss of AN function

To determine if chronic hypomyelination and the associated nodal structural aberrations caused by *qkl* KO at P5 can affect AN function, we performed ABR tests to measure threshold and suprathreshold responses. Our threshold measurements at P14 (**Figure 5.3.8 A**) show that QKI-KOs have greatly reduced sensitivities to pure tone stimuli across frequencies compared to QKI-Ctrls. Most QKI-KO mice tested at P14 had no response to any stimuli, so no analyses of any suprathreshold measurements were performed.

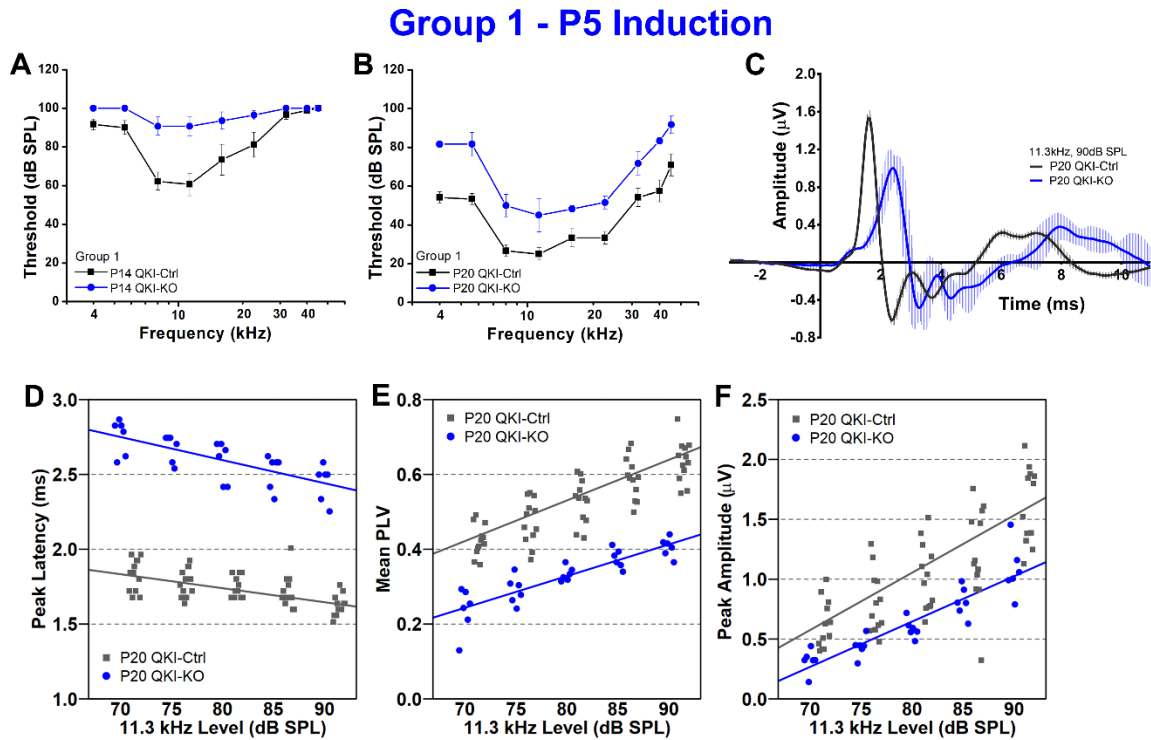


Figure 5.3.8: *qkl* KO-induced hypomyelination leads to loss of AN function

Trends of AN wave I threshold and suprathreshold measurements for the Group 1 KO mice showed increased thresholds, longer peak latencies, decreased synchrony, and diminished amplitudes compared to age-matched controls. **A** and **B** plot the thresholds of response (in dB SPL) across low to high frequency pure tone stimuli. Error bars indicating mean SEM are shown for each data point. **A** shows P14 QKI-KO animals have higher thresholds, if they responded at all compared to P14 QKI-Ctrl (n = 7 mice/7 ears for KO, n = 9 mice/9 ears for Ctrl). **B** shows that both groups at P20 had lower thresholds compared to P14, but that thresholds from QKI-KO animals were higher across all frequencies compared to QKI-Ctrl (n = 3 mice/3 ears for KO, n = 6 mice/6 ears for Ctrl). **C** shows the averaged ABR waveforms for P20 QKI-KO versus QKI-Ctrl animals stimulated at 90dB SPL intensity at 11.3kHz. Lighter vertical bars show mean SEM across data points for each group. Compared to QKI-Ctrl, the QKI-KO waveform clearly shows a lower and delayed wave I peak. Wave I is also wider for the QKI-KO compared to QKI-Ctrl. **D-F** plot the suprathreshold wave I responses from 90-70 dB SPL stimuli at 11.3kHz from P20 mice (n = 3 mice/6 ears for KO, 6 mice/12 ears for Ctrl). Regression lines are plotted for each group. **D** shows that peak latencies are longer in QKI-KO compared to control. **(C)** Synchrony of AN response as measured by mean PLV is decreased in QKI-KO animals compared to controls. **(F)** peak amplitudes measurements show that QKI-KO animals respond in lower magnitudes compared to QKI-Ctrl.

By P20, thresholds of QKI-KO mice were lower (**Figure 5.3.8 B**), indicating that they actually developed hearing sensitivity over time. However, their thresholds across all tested frequencies were higher compared to QKI-Ctrls. Looking at the averaged waveform responses at 90 dB SPL (**Figure 5.3.8 C**), we see that compared to QKI-Ctrls, the AN wave I response of QKI-KOs were lower and delayed. The width of wave I was also wider in the QKI-KOs which can indicate dyssynchrony of AN fiber firing. Our suprathreshold measurements (**Figure 5.3.8 D-E**) show that the peak latencies of QKI-KO were much longer compared to QKI-Ctrls as seen by the wide separation between the data points and regression lines. Mean PLV, our measure of AN synchrony across trials, show that AN synchrony was decreased in the QKI-KOs compared to controls. Peak amplitude measurements across levels also showed a trend towards decrease in QKI-KO compared to QKI-Ctrls. Chronic hypomyelination, coupled with un-clustered heminodes and reduced integrity of axo-glial connections at the paranodal domains are implicated in our pathophysiological findings, especially in the delayed latencies and the dyssynchrony of AN firing.

5.3.9 Eventual dysmyelination due to *qkl* KO at peak myelination may lead to functional declines in later development

In parallel with our physiological studies for Group 1, we decided to test ABRs on our Group 2 animals with the *qkl* KO at P7 during peak myelination. Our results for the suprathreshold measurements at P14 (**Figure 5.3.9 A-C**) show that peak latencies and amplitudes of AN wave I and synchrony of AN firing

were not significantly different between the QKI-Ctrl and QKI-KO animals. The similar responses between the QKI-Ctrl and QKI-KO, the contrast with our findings in Group 1 P14 may be due to our results showing that the majority of P14 QKI-KO SGNs were densely myelinated throughout their axons (**Figure 5.3.3**). We also showed that axo-glial connector protein Cntn1 was still present in the heminode and axonal paranodes in these P14 QKI-KO mice.

By P21, the responses between QKI-KO and QKI-Ctrl are more distinguishable (**Figure 5.3.9 D-F**). There is a trend towards increased wave I latencies and decreased AN firing synchrony in the QKI-KO mice compared to QKI-Ctrls. Peak amplitudes are distinguishably different. Although these results are not as striking compared to our physiological findings in P20 Group 1, eventual dysmyelination due to dysfunctional glial cells may still be implicated in AN functional declines. Together with our results shown in **Figure 5.3.8**, these findings highlight the importance of normal myelinogenesis and myelin maintenance for proper AN function. The structural and functional phenotypic differences between the QKI-KO groups also accentuates the critical time points for *qkl*'s role in myelinogenesis and regulation of myelin maintenance.

Group 2 - P7 Induction

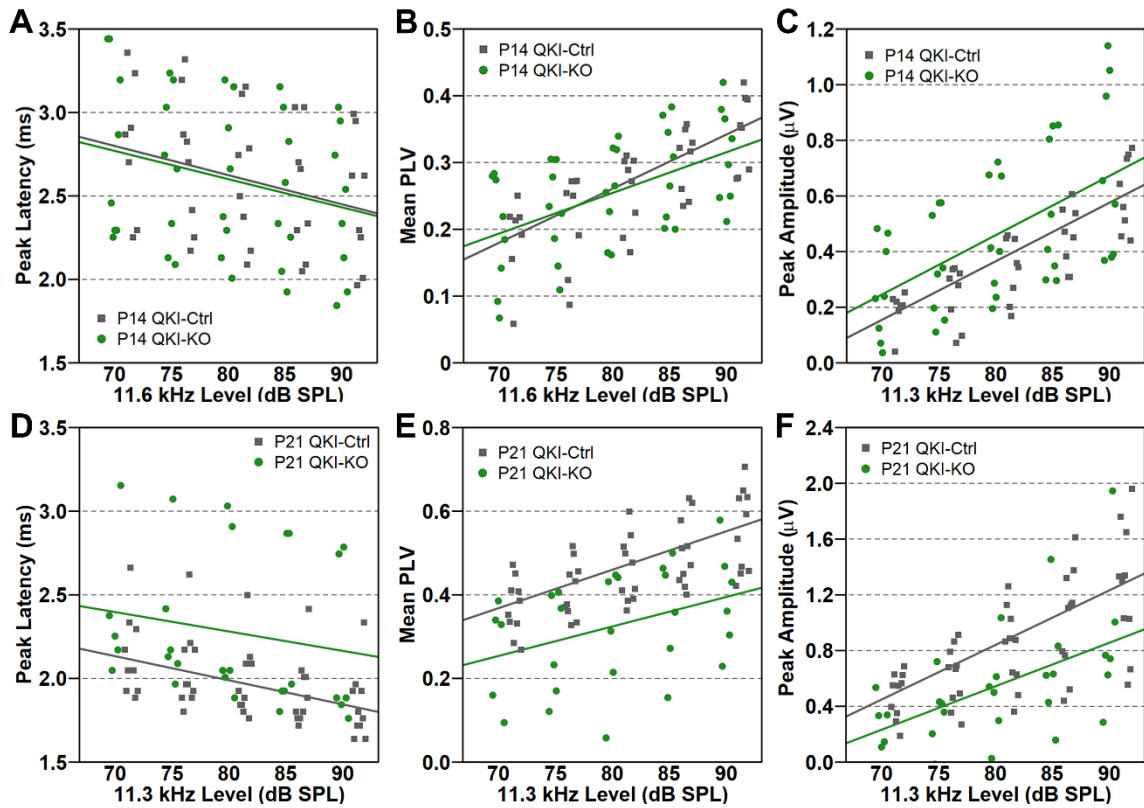


Figure 5.3.9: Eventual dysmyelination due to *qki* KO at peak myelination may lead to functional declines in later development

Suprathreshold measurements of peak latency (A), mean PLV (B), and peak amplitude (C) show no difference between P14 QKI-KO and QKI-Ctrl. ($n = 4$ mice/8 ears per group). Measurements between QKI-KO and QKI-Ctrl at P21 (D-F) shows a trend towards AN functional declines. ($n = 3$ mice/6 ears for QKI-KO, $n = 5$ mice/10 ears for QKI-Ctrl). Regression lines are shown for each group.

5.4 Discussion

Through the work done in this chapter, we showed that primary glial dysfunction due to the *qkl* KO around the critical time period of myelination caused severe AN structural abnormalities pertaining to myelination and nodal formation. All three node types were affected by the glial dysfunction. We showed that *Cntn1* was chronically ablated in all paranodes and our ultrastructural studies showing detachment of glial process/myelin from the SGN membrane or loose, non-compact myelin lamellae indicate that the axo-glial and glial-glial connections were either not present or were compromised after *qkl* knockout. Importantly, we showed that the ensuing dysmyelination and nodal structural malformation led to SNHL, as shown by slower conduction velocities and AN dyssynchrony in the mutated mice. Studies of PNS diseases, such as GBS and CMT indicate that nodal disruption⁶⁵ and demyelination^{64, 190} are associated with decreased nerve function leading to sensory loss and muscle weakness. Here, we show similar results occurring in the AN after primary glial dysfunction which greatly implies the importance of normally functioning glia.

Our studies also showed that *qkl* is essential for myelinogenesis and subsequent myelin maintenance in the developing mouse AN. Knocking out *qkl* around the onset of myelination, before peak myelination occurs was enough to cause chronic glial dysfunction that resulted in widespread inhibition of myelinogenesis, as shown by the continued enwrapment of the fibers/cell bodies only by a single layer of thick glial cell process even after the time point of

hearing maturation (P20/21). Mature myelin is characterized by multiple, thin lamellae that are compactly stacked atop each other. The glial processes exude their cytoplasm as they proceed to enwrap the axons. Myelination of the SGNs never fully initiated in the hypomyelinated fibers and the AN response were chronically impaired as shown by our physiological studies of the P20 QKI-KO mice from the Group 1 – P5 induction. Our studies also show that myelinogenesis cannot be inhibited or reversed by the knockout of *qkl* at the peak of myelination. Rather, our P7 induction group emphasizes *qkl*'s importance for continued maintenance of myelination by AN glial cells. These Group 2 – P7 induction animals had multi-layered, compact myelin at both P14 and P21. However, by P21, the eventual dysmyelination due to the dysregulation myelin maintenance is apparent by the loosening of the multi-layered myelin and detachment from the SGNs. In addition, *Cntn1* expression, which was reduced, but still slightly present in Group 2 P14 QKI-KO, is completely lost in the P21 QKI-KO paranodes. The differing phenotypic outcomes between the pre-peak and peak myelination initiation of *qkl*/QKI-RBP deficiency demonstrate that *qkl*'s regulation of myelin formation and maintenance is developmental stage-dependent.

In the mouse AN, we knocked out the QKI-RBPs specifically in the AN glial cells, as the *Plp1* promoter and the *qkl* gene were colocalized only in the AN glial cells. QKI-RBPs have more than a thousand QRE-containing putative downstream mRNA targets^{59,140}, including the *qkl* gene itself¹⁹¹. In addition to mRNAs, the QKI-RBPs were shown to bind other forms of RNA that have the

QRE sequences. They were shown to target hundreds of circular RNAs, and were implicated in playing a role in circular RNA synthesis and regulation¹⁹². They were also shown to bind and affect processing of microRNAs^{193,194}. We saw that different sets of QKI-RBPs targets were up-regulated in P3 and in P7, implying that the QKI-RBP targets in P3 are involved in myelinogenesis and the targets in P7 are involved in myelin maintenance. In order to more directly figure out what targets are being bound and affected by QKI-RBPs, in the AN, we could perform RNA-IP and sequence the resulting products. This would first give us a list of actual, present targets in the AN. We could also perform RNA-seq total RNAs from isolated samples from both Group 1 – P5 and Group 2 – P7 induction at both P14 and P20/21 to find which target genes are more or less affected by each induction group for both time points. Comparing target genes in P14 would be very valuable because it is at that time when the phenotypic differences between the two are greater, and this would indicate which genes are more involved in myelinogenesis. Comparing the target genes in P20/21 would also be good because dysmyelination is present in both QKI-KOs, indicating which genes are necessary for myelin maintenance.

Other important findings in this chapter include *qkl* KO-induced recruitment of macrophages and the pathological morphologies of the SGCs we saw, especially in the P5 *qkl* KO. Although SGN apoptosis may signal these macrophages, visual inspection of SGN numbers through our TEM and immunohistochemical studies indicate that SGN death in the QKI-KO mice were not rampant. SGN losses, at least in the middle turn where most of our studies

focused on, were not comparable to those seen in cochlea injured by ototoxic drugs^{195,196}. Perhaps dysfunction of the glial cells were enough to cause active recruitment of macrophages.

The SGCs can be thought to the more plastic AN glial cell compared to their SC counterparts as they are shown to express Sox2, which is a marker of proliferation¹⁵³, even in normal cochlea. KO of *qkl* seem to affect function and morphology of SGCs more than they do SCs, as dysmyelination around the somata were prevalent for both QKI-KO groups. We also found that Sox2 expression was decreased at either endpoints of both QKI-KO groups compared to the QKI-Ctrls (Appendix A-2). This could indicate loss in plasticity. However, our ultrastructural studies also show that SGCs in QKI-KO take on a more globular shape and appear similar to activated macrophages. Earlier in Chapter 3, we discussed the possibility of SGCs playing a role in inflammation and neuropathic pain. Here we showed that SGCs appear diseased or macrophage-like after the QKI-KO. Perhaps, SGCs in the AN are playing a role in inflammation either directly, similar to the inflammatory response seen after direct SGC mutation in the trigeminal nerve¹¹³, or by producing inflammatory factors in response to fractalkine signaling after injury¹¹⁴. It would be interesting to compare the molecular characteristics of normal and QKI-KO SGCs to cochlear macrophages to see how AN SGCs are playing a role in inflammation. This could be performed through co-immunostaining analyses of macrophage/microglial markers with SGC markers. Single cell sequencing of cochlear macrophages and SGCs could also be an option.

Taken together, our findings show that *qkl* is essential for AN structural development and maintenance and that primary glial dysfunction can lead to SNHL. Both *qkl* and the AN glial cells should be further studied as possible therapeutic targets in SNHL.

Chapter 6: Global discussion

The primary goal of these studies was to determine the importance of normal functioning AN glial cells for AN structural and functional development and maintenance. Formation and maintenance of myelin and the nodal structures, along with providing trophic support for the SGNs and clearance of debris, are the main functions of SCs and SGCs in the AN. Much of these functions require the interaction of AN glial cells with SGNs. Aside from hair cell and cochlear lateral wall abnormalities, SGN pathologies, including synaptopathy and SGN loss due to injury via noise or ototoxic drugs are thought to be the primary cause of the “neural” part of SNHL. Compared to the research dedicated to SGNs, not much work has been done to elucidate the importance of cochlear glial cells to the AN.

The best way to determine the importance of the AN glial cells was to induce their dysfunction. But first, we needed to characterize their role in AN development to elucidate their importance for AN structure and function. One indirect measure of glial function besides myelination was to study the formation and maturation of excitable nodal domains and flanking paranodal structures. Proper axo-glial connections at the paranodal domain are required for clustering of VGSCs at the nodal gap and separating those VGSCs from the VGKCs of the juxtaparanode. Excitable nodal domains along myelinated sheaths are responsible for saltatory conduction. Direct measurements of myelination and nodal formation include physiological tests determining AN conduction and neural synchrony. As we could not perform single neuron recordings, we could

not determine the direct contribution of the excitable nodal domains to neuronal function. However, ABR measurements can give us information on AN latency, which corresponds to conduction velocity through the AN fibers, and the PLV across a presented number of trials, which can indicate the synchrony of fiber firing.

With our research in Chapter 3, we were one of the first in the field to characterize the three types of AN nodal domains and the differing myelin morphologies of the SCs and SGCs. We also showed the importance of nodal structural maturation for AN functional maturation. Specifically, we determined that shortening of ganglion node lengths were associated with increases in AN wave I amplitude. We also showed that we were able to use the methods we developed/adapted and refined to study the nodal structures, and indirectly, glial function, for our subsequent studies.

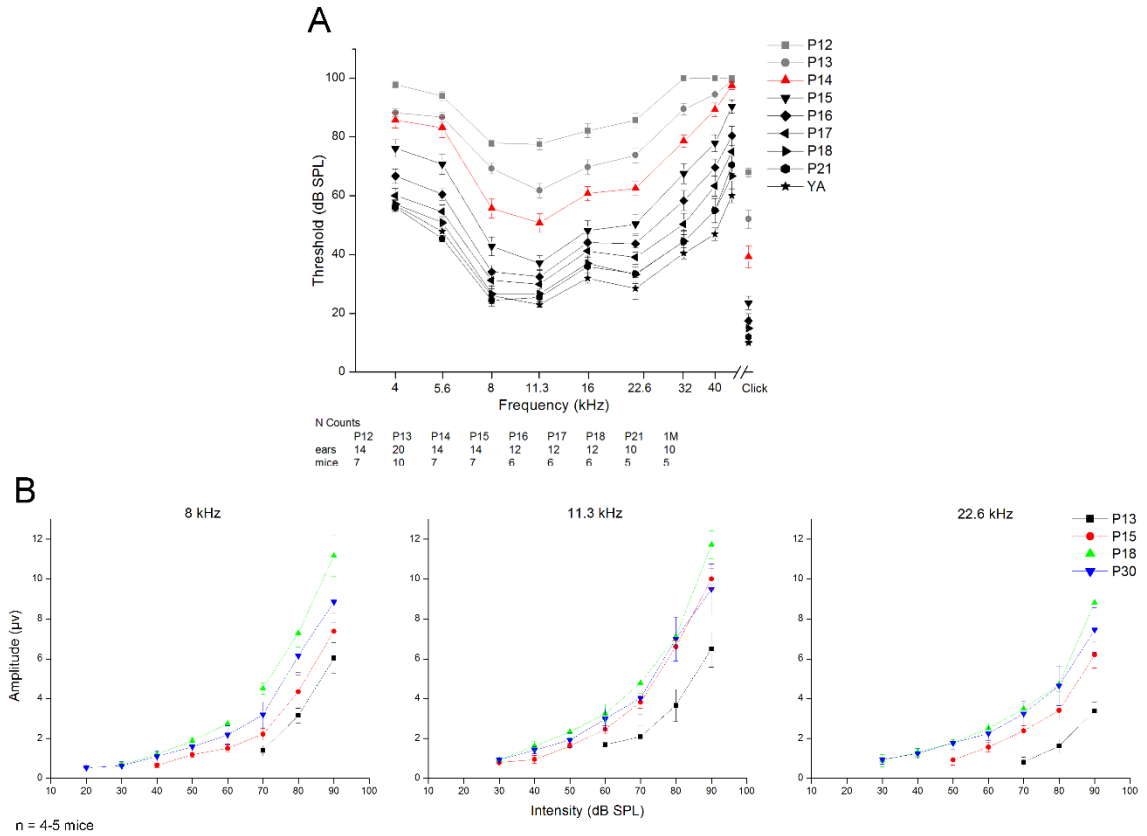
One of the easiest ways to study AN injury and recovery is through noise exposure. Through our noise injury studies, we found glial dysfunction through the dysregulation of QKI-RBPs and their targets as contributors to the inability of the AN to recover its structure and function fully after high intensity noise exposure. We also determined the importance of *qkl*, a known regulator of myelination in other PNS systems for AN myelin and nodal structural maintenance. Our research with *qkl* dysregulation in response to noise injury led us to our subsequent studies of glial dysfunction and *qkl* dysregulation in the developing AN. Through this, we developed a method to study glial dysfunction in the developing AN through the KO of *qkl* in either pre-peak or at peak

myelination. As a result, we found that primary glial dysfunction during development leads to dysmyelination and loss of hearing function.

Besides forming and maintaining proper myelination and nodal formation for rapid saltatory conduction, one main argument for studying and finding ways to manipulate AN glial cells is for cochlear implantation. Cochlear implants work by directly stimulating the AN fibers to evoke responses⁶³. If there are barely any AN fibers left, there would be nothing to stimulate. If dysmyelination is present in the remaining fibers excited by the implant, the ensuing response could be dyssynchronous or delayed, which further reduces the effect and value of that implant. There are also issues with cochlear inflammation due to trauma¹⁹⁷ or intracochlear bleeding¹⁹⁸ implantation which proceed to cause damage and fibrosis, reducing the effectiveness of the device. We discussed in Chapter 3 and 5 the possible role of SGCs as a responder in the inflammatory response. This makes the SGCs a lucrative therapeutic target not only in relation to cochlear implantation, but also in the case of other AN inflammation, such as in noise injury. The fact that deletion of *qkl* in the AN glial cells produced a large inflammatory response also implicate *qkl*/QKI-RBPs and their targets as regulators of AN inflammation. Since we show that *qkl* deletion affects myelination and inflammation, researching possible gene therapies involving *qkl*/QKI-RBPs would also be important.

Chapter 7: Appendix

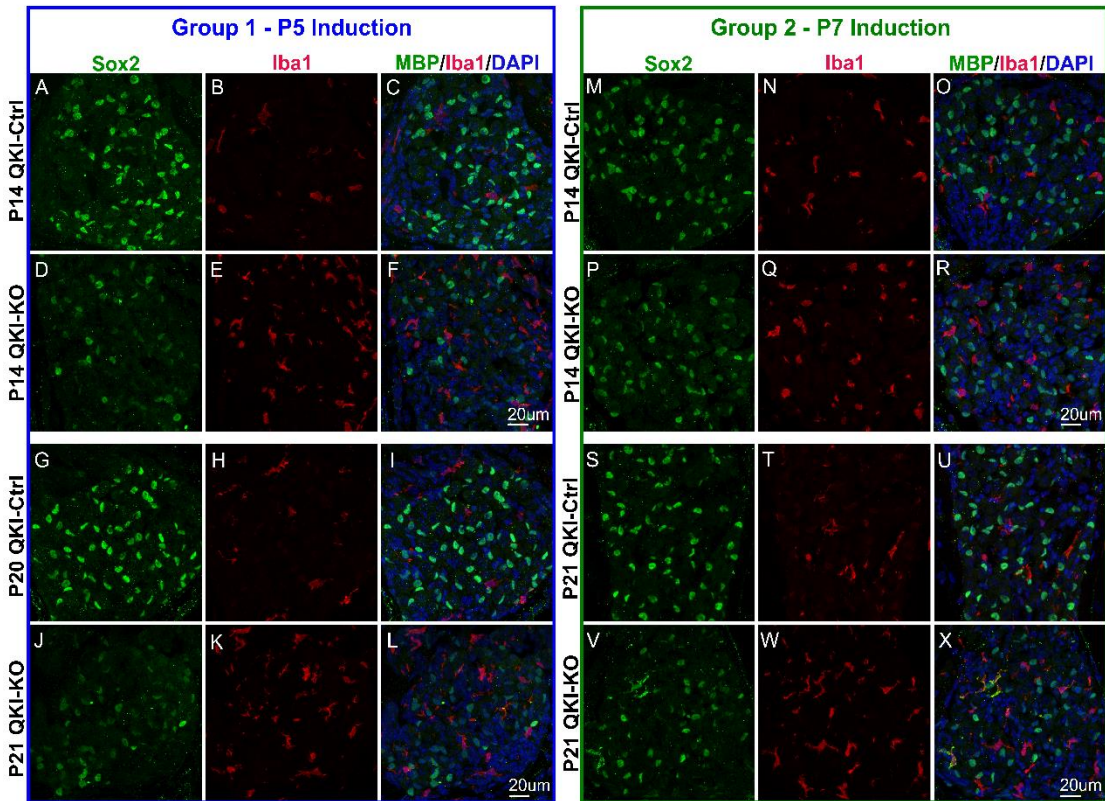
Appendix A-1



A-1: ABR measurements after hearing onset

A,B showed AN wave I threshold (A) and suprathreshold amplitude (B) measurements from the period of hearing onset (~P13) to functional maturation in young-adult

Appendix A-2



A-2: KO of *qkl* induced a chronic decrease of the Sox2 marker of plasticity in SGCs and increase of number of Iba1⁺ macrophages.

KO of *qkl* at either time point lead to decreased Sox2 expression (green), as evidenced by decreased intensity of anti-Sox2 reactivity in Group 1 P14/20 (**D,J**) and Group 2 P14/21 (**P,V**) compared to their respective controls (**A,G** and **M,S**). Morphology and location of the Sox2 staining indicate that Sox2 is localized in SGCs in the RC. The increased numbers of Iba1⁺ macrophages (red) at either endpoint for both groups (**E,K** and **Q,W**) compared to QKI-Ctrls (**B,H** and **N,T**) is also very much apparent. Representative images were taken at the RC for each group and both P14 and P20/21 endpoints are shown. Nuclei were counterstained with DAPI. Merged images are shown in for either group in **C,F,I,L** and **O,R,U,X**.

Chapter 8: References

1. Johnson, S. B., Schmitz, H. M. & Santi, P. A. TSLIM imaging and a morphometric analysis of the mouse spiral ganglion. *Hear. Res.* **278**, 34–42 (2011).
2. Nadol, J. B. Quantification of human spiral ganglion cells by serial section reconstruction and segmental density estimates. *Am. J. Otolaryngol.* **9**, 47–51 (1988).
3. Dallos, P. The active cochlea. *J. Neurosci.* **12**, 4575–4585 (1992).
4. Reid, M. A., Flores-Otero, J. & Davis, R. L. Firing Patterns of Type II Spiral Ganglion Neurons In Vitro. *J. Neurosci.* **24**, 733–742 (2004).
5. Flores, E. N. *et al.* A Non-canonical Pathway from Cochlea to Brain Signals Tissue-Damaging Noise. *Curr. Biol.* **25**, 606–612 (2015).
6. Liu, C., Glowatzki, E. & Fuchs, P. A. Unmyelinated type II afferent neurons report cochlear damage. *Proc. Natl. Acad. Sci. U. S. A.* **112**, 14723–7 (2015).
7. Liberman, M. C. Auditory-nerve response from cats raised in a low-noise chamber. *J. Acoust. Soc. Am.* **63**, 442–455 (1978).
8. Kiang, N. Discharge patterns of single fibers in the cat's auditory nerve. (1965).
9. Schmiedt, R. A. Spontaneous rates, thresholds and tuning of auditory-nerve fibers in the gerbil: Comparisons to cat data. *Hear. Res.* **42**, 23–35 (1989).
10. Liberman, M. C. Morphological differences among radial afferent fibers in the cat cochlea: an electron-microscopic study of serial sections. *Hear. Res.* **3**, 45–63 (1980).
11. Merchan-Perez, A. & Liberman, M. C. Ultrastructural differences among afferent synapses on cochlear hair cells: correlations with spontaneous discharge rate. *J. Comp. Neurol.* **371**, 208–21 (1996).
12. Schaette, R. & McAlpine, D. Tinnitus with a Normal Audiogram: Physiological Evidence for Hidden Hearing Loss and Computational Model. *J. Neurosci.* **31**, (2011).
13. Kujawa, S. & Liberman, C. Adding insult to injury: cochlear nerve degeneration after “temporary” noise-induced hearing loss. *J. Neurosci.* **29**, 14077–14085 (2009).
14. Wan, G. & Corfas, G. Transient auditory nerve demyelination as a new mechanism for hidden hearing loss. *Nat. Commun.* **8**, 14487 (2017).
15. Rutherford, M. A., Chapochnikov, N. M. & Moser, T. Spike Encoding of Neurotransmitter Release Timing by Spiral Ganglion Neurons of the Cochlea. *J. Neurosci.* **32**, 4773–4789 (2012).
16. Liu, W. *et al.* Possible role of gap junction intercellular channels and connexin 43 in satellite glial cells (SGCs) for preservation of human spiral ganglion neurons: A comparative study with clinical implications. *Cell Tissue Res.* **355**, 267–278 (2014).
17. Akil, O. *et al.* Spiral Ganglion Degeneration and Hearing Loss as a Consequence of Satellite Cell Death in Saposin B-Deficient Mice. *J. Neurosci.* **35**, 3263–3275 (2015).
18. Toesca, A. Central and peripheral myelin in the rat cochlear and vestibular

- nerves. *Neurosci. Lett.* **221**, 21–24 (1996).
19. Le Douarin, N. M. & Dupin, E. Multipotentiality of the neural crest. *Curr. Opin. Genet. Dev.* **13**, 529–36 (2003).
 20. Jessen, K. R. & Mirsky, R. The origin and development of glial cells in peripheral nerves. *Nat. Rev. Neurosci.* **6**, 671–682 (2005).
 21. Shah, N. M., Marchionni, M. A., Isaacs, I., Stroobant, P. & Anderson, D. J. Glial growth factor restricts mammalian neural crest stem cells to a glial fate. *Cell* **77**, 349–60 (1994).
 22. Morrison, S. J. *et al.* Transient Notch activation initiates an irreversible switch from neurogenesis to gliogenesis by neural crest stem cells. *Cell* **101**, 499–510 (2000).
 23. Corfas, G., Velardez, M. O., Ko, C.-P., Ratner, N. & Peles, E. Mechanisms and Roles of Axon-Schwann Cell Interactions. *J. Neurosci.* **24**, (2004).
 24. Feltri, M. L., Poitelon, Y. & Previtali, S. C. How Schwann Cells Sort Axons. *Neurosci.* **22**, 252–265 (2016).
 25. Taveggia, C. *et al.* Neuregulin-1 type III determines the ensheathment fate of axons. *Neuron* **47**, 681–94 (2005).
 26. Topilko, P. *et al.* Krox-20 controls myelination in the peripheral nervous system. *Nature* **371**, 796–799 (1994).
 27. Monk, K. R., Feltri, M. L. & Taveggia, C. New insights on schwann cell development. *Glia* 1–18 (2015). doi:10.1002/glia.22852
 28. Fernandez-Valle, C., Bunge, R. P. & Bunge, M. B. Schwann cells degrade myelin and proliferate in the absence of macrophages: evidence from in vitro studies of Wallerian degeneration. *J. Neurocytol.* **24**, 667–79 (1995).
 29. Arthur-Farraj, P. J. *et al.* c-Jun Reprograms Schwann Cells of Injured Nerves to Generate a Repair Cell Essential for Regeneration. *Neuron* **75**, 633–647 (2012).
 30. Stassart, R. M. *et al.* A role for Schwann cell-derived neuregulin-1 in remyelination. *Nat. Neurosci.* **16**, 48–54 (2012).
 31. Sherman, D. L. & Brophy, P. J. Mechanisms of axon ensheathment and myelin growth. *Nat. Rev. Neurosci.* **6**, 683–690 (2005).
 32. Whitlon, D. S., Tieu, D., Grover, M., Reilly, B. & Coulson, M. T. Spontaneous association of glial cells with regrowing neurites in mixed cultures of dissociated spiral ganglia. *Neuroscience* **161**, 227–35 (2009).
 33. Lang, H. *et al.* Sox2 up-regulation and glial cell proliferation following degeneration of spiral ganglion neurons in the adult mouse inner ear. *JARO - J. Assoc. Res. Otolaryngol.* **12**, 151–171 (2011).
 34. Wang, S. S.-H. *et al.* Functional Trade-Offs in White Matter Axonal Scaling. *J. Neurosci.* **28**, 4047–4056 (2008).
 35. Griffin, J. W. & Thompson, W. J. Biology and pathology of nonmyelinating Schwann cells. *Glia* **56**, 1518–1531 (2008).
 36. Eshed, Y. *et al.* Gliomedin mediates Schwann cell-axon interaction and the molecular assembly of the nodes of Ranvier. *Neuron* **47**, 215–229 (2005).
 37. Feinberg, K. *et al.* A Glial Signal Consisting of Gliomedin and NrCAM Clusters Axonal Na⁺ Channels during the Formation of Nodes of Ranvier. *Neuron* **65**, 490–502 (2010).

38. Amor, V. *et al.* Long-term maintenance of Na⁺ channels at nodes of Ranvier depends on glial contact mediated by gliomedin and NrCAM. *J. Neurosci.* **34**, 5089–98 (2014).
39. Custer, A. W. *et al.* The role of the ankyrin-binding protein NrCAM in node of Ranvier formation. *J. Neurosci.* **23**, 10032–10039 (2003).
40. Lacas-Gervais, S. IV 1 spectrin stabilizes the nodes of Ranvier and axon initial segments. *J. Cell Biol.* **166**, 983–990 (2004).
41. Rios, J. C. *et al.* Contactin-associated protein (Caspr) and contactin form a complex that is targeted to the paranodal junctions during myelination. *J. Neurosci.* **20**, 8354–8364 (2000).
42. Boyle, M. E. T. T. *et al.* Contactin Orchestrates Assembly of the Septate-like Junctions at the Paranode in Myelinated Peripheral Nerve. *Neuron* **30**, 385–397 (2001).
43. Pillai, A. M. *et al.* Spatiotemporal ablation of myelinating glia-specific neurofascin (NfascNF155) in mice reveals gradual loss of paranodal axoglial junctions and concomitant disorganization of axonal domains. *J. Neurosci. Res.* **87**, 1773–1793 (2009).
44. Arroyo, E. J., Sirkowski, E. E., Chitale, R. & Scherer, S. S. Acute demyelination disrupts the molecular organization of peripheral nervous system nodes. *J. Comp. Neurol.* **479**, 424–434 (2004).
45. Poliak, S. *et al.* Caspr2, a New Member of the Neurexin Superfamily, Is Localized at the Juxtaparanodes of Myelinated Axons and Associates with K⁺ Channels. *Neuron* **24**, 1037–1047 (1999).
46. Poliak, S. *et al.* Juxtaparanodal clustering of Shaker-like K⁺ channels in myelinated axons depends on Caspr2 and TAG-1. *J. Cell Biol.* **162**, 1149–60 (2003).
47. Devaux, J., Gola, M., Jacquet, G. & Crest, M. Effects of K⁺ Channel Blockers on Developing Rat Myelinated CNS Axons: Identification of Four Types of K⁺ Channels. *J. Neurophysiol.* **87**, (2002).
48. Rasband, M. N. & Trimmer, J. S. Subunit composition and novel localization of K⁺ channels in spinal cord. *J. Comp. Neurol.* **429**, 166–76 (2001).
49. Rasband, M. N. *et al.* Potassium channel distribution, clustering, and function in remyelinating rat axons. *J. Neurosci.* **18**, 36–47 (1998).
50. Kim, K. X. & Rutherford, M. A. Maturation of NaV and KV Channel Topographies in the Auditory Nerve Spike Initiator before and after Developmental Onset of Hearing Function. *J. Neurosci.* **36**, 2111–2118 (2016).
51. Tagoe, T., Barker, M., Jones, A., Allcock, N. & Hamann, M. Auditory Nerve Perinodal Dysmyelination in Noise-Induced Hearing Loss. *J. Neurosci.* **34**, 2684–2688 (2014).
52. SIDMAN, R. L., DICKIE, M. M. & APPEL, S. H. MUTANT MICE (QUAKING AND JIMPY) WITH DEFICIENT MYELINATION IN THE CENTRAL NERVOUS SYSTEM. *Science* **144**, 309–11 (1964).
53. Ebersole, T. A., Chen, Q., Justice, M. J. & Artzt, K. The quaking gene product necessary in embryogenesis and myelination combines features of RNA binding and signal transduction proteins. *Nat. Genet.* **12**, 260–5 (1996).

54. Chen, T. & Richard, S. Structure-function analysis of Qk1: a lethal point mutation in mouse quaking prevents homodimerization. *Mol. Cell. Biol.* **18**, 4863–4871 (1998).
55. Teplova, M. *et al.* Structure-function studies of STAR family Quaking proteins bound to their in vivo RNA target sites. *Genes Dev.* **27**, 928–40 (2013).
56. Larocque, D. *et al.* Nuclear Retention of MBP mRNAs in the Quaking Viable Mice. *Neuron* **36**, 815–829 (2002).
57. Wu, J. I., Reed, R. B., Grabowski, P. J. & Artzt, K. Function of quaking in myelination: Regulation of alternative splicing. *Proc. Natl. Acad. Sci.* **99**, 4233–4238 (2002).
58. Larocque, D. *et al.* The QKI-6 and QKI-7 RNA binding proteins block proliferation and promote Schwann cell myelination. *PLoS One* **4**, 1–10 (2009).
59. Darbelli, L., Vogel, G., Almazan, G. & Richard, S. Quaking Regulates Neurofascin 155 Expression for Myelin and Axoglial Junction Maintenance. *J. Neurosci.* **36**, 4106–4120 (2016).
60. Centers for Disease Control and Prevention (CDC). Identifying infants with hearing loss - United States, 1999-2007. *MMWR. Morb. Mortal. Wkly. Rep.* **59**, 220–3 (2010).
61. Olusanya, B. O., Neumann, K. J. & Saunders, J. E. The global burden of disabling hearing impairment: a call to action. *Bull. World Heal. Organ.* **92**, 367–373 (2014).
62. Hoffman, H. J., Dobie, R. A., Losonczy, Katalin, G., Themann, C. L. & Flamme, G. A. Declining Prevalence of Hearing Loss in US Adults Aged 20 to 69 Years. *JAMA Otolaryngol. - Head Neck Surg.* 1–12 (2016). doi:10.1001/jamaoto.2016.3527
63. American Speech-Language-Hearing Association. Cochlear Implants. (2017). Available at: <http://www.asha.org/public/hearing/Cochlear-Implant/>. (Accessed: 16th February 2017)
64. Rosenbluth, J. & Bobrowski-Khoury, N. Paranodal dysmyelination in peripheral nerves of Trembler mice. *J. Neurosci. Res.* **92**, 476–485 (2014).
65. Devaux, J. J., Odaka, M. & Yuki, N. Nodal proteins are target antigens in Guillain-Barré syndrome. *J. Peripher. Nerv. Syst.* **17**, 62–71 (2012).
66. Spoendlin, H. Retrograde degeneration of the cochlear nerve. *Acta Otolaryngol.* **79**, 266–75 (1975).
67. Felder, E., Kanonier, G., Scholtz, A., Rask-Andersen, H. & A Schrott-Fischer, A. Quantitative evaluation of cochlear neuronal and computer-aided three-dimensional reconstruction of spiral ganglion cells in humans with a peripheral loss of nerve fibres. *Hear. Res.* **105**, 183–190 (1997).
68. Teufert, K. B., Linthicum, F. H. & Connell, S. S. The Effect of Organ of Corti Loss on Ganglion Cell Survival in Humans. *Otol. Neurotol.* **27**, 1146–1151 (2006).
69. Ohlemiller, K. K., Dahl, A. R. & Gagnon, P. M. Divergent aging characteristics in CBA/J and CBA/CaJ mouse cochleae. *JARO - J. Assoc. Res. Otolaryngol.* **11**, 605–623 (2010).

70. Lewis, M. A. *et al.* An ENU-induced mutation of miR-96 associated with progressive hearing loss in mice. *Nat. Genet.* **41**, 614–8 (2009).
71. Kuhn, S. *et al.* miR-96 regulates the progression of differentiation in mammalian cochlear inner and outer hair cells. *Proc. Natl. Acad. Sci. U. S. A.* **108**, 2355–2360 (2011).
72. Doerflinger, N. H., Macklin, W. B. & Popko, B. Inducible site-specific recombination in myelinating cells. *Genesis* **35**, 63–72 (2003).
73. Truett, G. E. *et al.* Preparation of PCR-Quality Mouse Genomic DNA with Hot Sodium Hydroxide and Tris (HotSHOT). *Biotechniques* **29**, 52–54 (2000).
74. Lang, H. *et al.* Neural stem/progenitor cell properties of glial cells in the adult mouse auditory nerve. *Sci. Rep.* **5**, 13383 (2015).
75. Harris, K. C., Vaden, K. I., McClaskey, C. M., Dias, J. W. & Dubno, J. R. Complementary metrics of human auditory nerve function derived from compound action potentials. *J. Neurophysiol.* **119**, 1019–1028 (2018).
76. Allen, D. L. *et al.* Effects of spaceflight on murine skeletal muscle gene expression. *J. Appl. Physiol.* **106**, 582–95 (2009).
77. Irizarry, R. A. *et al.* Exploration, normalization, and summaries of high density oligonucleotide array probe level data. *Biostatistics* **4**, 249–264 (2003).
78. Livak, K. J. & Schmittgen, T. D. Analysis of Relative Gene Expression Data Using Real-Time Quantitative PCR and the 2- $\Delta\Delta$ CT Method. *Methods* **25**, 402–408 (2001).
79. Brown, L. N. *et al.* Macrophage-Mediated Glial Cell Elimination in the Postnatal Mouse Cochlea. *Front. Mol. Neurosci.* **10**, 407 (2017).
80. Zhao, S. & Fernald, R. D. Comprehensive algorithm for quantitative real-time polymerase chain reaction. *J. Comput. Biol.* **12**, 1047–64 (2005).
81. Xing, Y. *et al.* Age-related changes of myelin basic protein in mouse and human auditory nerve. *PLoS One* **7**, (2012).
82. Love, M. I., Huber, W. & Anders, S. Moderated estimation of fold change and dispersion for RNA-seq data with DESeq2. *Genome Biol.* **15**, 550 (2014).
83. Li, C. & Hung Wong, W. Model-based analysis of oligonucleotide arrays: model validation, design issues and standard error application. *Genome Biol.* **2**, RESEARCH0032 (2001).
84. R Foundation for Statistical Computing. R: The R Project for Statistical Computing. (2019). Available at: <https://www.r-project.org/>. (Accessed: 24th February 2019)
85. Carbon, S. *et al.* AmiGO: online access to ontology and annotation data. *Bioinformatics* **25**, 288–9 (2009).
86. Song, L., McGee, J. & Walsh, E. J. Frequency- and level-dependent changes in auditory brainstem responses (ABRs) in developing mice. *J. Acoust. Soc. Am.* **119**, 2242–2257 (2006).
87. van Roy, F. & Berx, G. The cell-cell adhesion molecule E-cadherin. *Cell. Mol. Life Sci.* **65**, 3756–3788 (2008).
88. Woods, D. F., Hough, C., Peel, D., Callaini, G. & Bryant, P. J. Dlg protein is required for junction structure, cell polarity, and proliferation control in

- Drosophila epithelia*. *J. Cell Biol.* **134**, 1469–82 (1996).
89. Ervasti, J. M. & Campbell, K. P. A role for the dystrophin-glycoprotein complex as a transmembrane linker between laminin and actin. *J. Cell Biol.* **122**, 809–23 (1993).
 90. Kaplan, M., Cho, M., Ullian, E. & Isom, L. Differential Control of Clustering of the Sodium Channels Na v 1.2 and Na v 1.6 at Developing CNS Nodes of Ranvier. *Neuron* **30**, 105–119 (2001).
 91. Ishibashi, T. *et al.* Tetraspanin Protein CD9 Is a Novel Paranodal Component Regulating Paranodal Junctional Formation. (2004). doi:10.1523/JNEUROSCI.1484-03.2004
 92. Orthmann-Murphy, J. L. *et al.* Hereditary spastic paraplegia is a novel phenotype for GJA12/GJC2 mutations. *Brain* **132**, 426–38 (2009).
 93. Quarles, R. H., Everly, J. L. & Brady, R. O. Evidence for the close association of a glycoprotein with myelin in rat brain. *J. Neurochem.* **21**, 1177–91 (1973).
 94. Eylar, E. H., Brostoff, S., Hashim, G., Caccam, J. & Burnett, P. Basic A1 protein of the myelin membrane. The complete amino acid sequence. *J. Biol. Chem.* **246**, 5770–84 (1971).
 95. Snipes, G. J., Suter, U., Welcher, A. A. & Shooter, E. M. Characterization of a novel peripheral nervous system myelin protein (PMP-22/SR13). *J. Cell Biol.* **117**, 225–38 (1992).
 96. Kwon, H. S. *et al.* Myocilin mediates myelination in the peripheral nervous system through ErbB2/3 signaling. *J. Biol. Chem.* **288**, 26357–71 (2013).
 97. Li, C. *et al.* Myelination in the absence of myelin-associated glycoprotein. *Nature* **369**, 747–750 (1994).
 98. Zonta, B. *et al.* Glial and neuronal isoforms of Neurofascin have distinct roles in the assembly of nodes of Ranvier in the central nervous system. *J. Cell Biol.* **181**, 1169–77 (2008).
 99. Huang, C. Y.-M., Zhang, C., Zollinger, D. R., Leterrier, C. & Rasband, M. N. An α II Spectrin-Based Cytoskeleton Protects Large-Diameter Myelinated Axons from Degeneration. *J. Neurosci.* **37**, 11323–11334 (2017).
 100. Rios, J. C. *et al.* Paranodal interactions regulate expression of sodium channel subtypes and provide a diffusion barrier for the node of Ranvier. *J. Neurosci.* **23**, 7001–7011 (2003).
 101. Poliak, S. & Peles, E. The local differentiation of myelinated axons at nodes of Ranvier. *Nat. Rev. Neurosci.* **4**, 968–980 (2003).
 102. Sadanaga, M. & Morimitsu, T. Development of endocochlear potential and its negative component in mouse cochlea. *Hear. Res.* **89**, 155–161 (1995).
 103. Safieddine, S., El-Amraoui, A. & Petit, C. The auditory hair cell ribbon synapse: from assembly to function. *Annu. Rev. Neurosci.* **35**, 509–28 (2012).
 104. Liberman, M. C. Auditory-nerve response from cats raised in a low-noise chamber. *J. Acoust. Soc. Am.* **63**, 442–55 (1978).
 105. Shrestha, B. R. *et al.* Sensory Neuron Diversity in the Inner Ear Is Shaped by Activity Article Sensory Neuron Diversity in the Inner Ear Is Shaped by Activity. *Cell* **174**, 1229–1246 (2018).
 106. Sun, S. *et al.* Hair Cell Mechanotransduction Regulates Spontaneous

- Activity and Spiral Ganglion Subtype Specification in the Auditory System. *Cell* **174**, 1247–1263.e15 (2018).
107. Petitpré, C. *et al.* Neuronal heterogeneity and stereotyped connectivity in the auditory afferent system. *Nat. Commun.* **9**, 3691 (2018).
 108. Liberman, M. C. & Oliver, M. E. Morphometry of intracellularly labeled neurons of the auditory nerve: Correlations with functional properties. *J. Comp. Neurol.* **223**, 163–176 (1984).
 109. Taberner, A. M. Response Properties of Single Auditory Nerve Fibers in the Mouse. *J. Neurophysiol.* **93**, 557–569 (2004).
 110. Zeisel, A. *et al.* Molecular Architecture of the Mouse Nervous System Resource Molecular Architecture of the Mouse Nervous System. *Cell* **174**, 999–1014 (2018).
 111. Ohara, P. T. *et al.* Gliopathic Pain: When Satellite Glial Cells Go Bad. *Neurosci.* **15**, 450–463 (2009).
 112. Hanani, M. Satellite glial cells in sensory ganglia: From form to function. *Brain Res. Rev.* **48**, 457–476 (2005).
 113. Vit, J.-P., Ohara, P. T., Bhargava, A., Kelley, K. & Jasmin, L. Silencing the Kir4.1 Potassium Channel Subunit in Satellite Glial Cells of the Rat Trigeminal Ganglion Results in Pain-Like Behavior in the Absence of Nerve Injury. *J. Neurosci.* **28**, 4161–4171 (2008).
 114. Souza, G. R. *et al.* Fractalkine mediates inflammatory pain through activation of satellite glial cells. *Proc. Natl. Acad. Sci. U. S. A.* **110**, 11193–8 (2013).
 115. Borg, E. Loss of hair cells and threshold sensitivity during prolonged noise exposure in normotensive albino rats. *Hear. Res.* **30**, 119–126 (1987).
 116. Hamernik, R. P., Patterson, J. H., Turrentine, G. A. & Ahroon, W. A. The quantitative relation between sensory cell loss and hearing thresholds. *Hear. Res.* **38**, 199–211 (1989).
 117. Chen, G.-D. & Fechter, L. D. The relationship between noise-induced hearing loss and hair cell loss in rats. *Hear. Res.* **177**, 81–90 (2003).
 118. Wang, Y., Hirose, K. & Liberman, M. C. Dynamics of Noise-Induced Cellular Injury and Repair in the Mouse Cochlea. doi:10.1007/s101620020028
 119. Hirose, K. & Liberman, M. C. Lateral wall histopathology and endocochlear potential in the noise-damaged mouse cochlea. *J. Assoc. Res. Otolaryngol.* **4**, 339–52 (2003).
 120. Liberman, M. C. & Kiang, N. Y. S. Acoustic trauma in cats. Cochlear pathology and auditory-nerve activity. *Acta Oto-Laryngologica Suppl.* 1–63 (1978). doi:10.3109/00016487809127889
 121. Spoendlin, H. Factors inducing retrograde degeneration of the cochlear nerve. *Annals of Otology, Rhinology and Laryngology* **93**, 76–82 (1984).
 122. Bao, J. & Ohlemiller, K. K. Age-related loss of spiral ganglion neurons. *Hear. Res.* **264**, 93–97 (2010).
 123. Susuki, K. Node of Ranvier disruption as a cause of neurological diseases. *ASN Neuro* **5**, 209–19 (2013).
 124. Hossain, W. A., Antic, S. D., Yang, Y., Rasband, M. N. & Morest, D. K. Where Is the Spike Generator of the Cochlear Nerve? Voltage-Gated Sodium Channels in the Mouse Cochlea. *J. Neurosci.* **25**, 6857–6868 (2005).

125. Long, P. & Corfas, G. Neuroscience. To learn is to myelinate. *Science* **346**, 298–9 (2014).
126. Rao, S. N. R. & Pearse, D. D. Regulating Axonal Responses to Injury: The Intersection between Signaling Pathways Involved in Axon Myelination and The Inhibition of Axon Regeneration. *Front. Mol. Neurosci.* **9**, 33 (2016).
127. Fu, X. D., Ares Jr., M. & Ares Jr., M. Context-dependent control of alternative splicing by RNA-binding proteins. *Nat. Rev. Genet.* **15**, 689–701 (2014).
128. Hardy, R. J. *et al.* Neural cell type-specific expression of QKI proteins is altered in quakingviable mutant mice. *J. Neurosci.* **16**, 7941–9 (1996).
129. Pilotte, J., Larocque, D. & Richard, S. Nuclear translocation controlled by alternatively spliced isoforms inactivates the QUAKING apoptotic inducer. *Genes Dev.* **15**, 845–858 (2001).
130. Zhao, L., Tian, D., Xia, M., Macklin, W. B. & Feng, Y. Rescuing qkV dysmyelination by a single isoform of the selective RNA-binding protein QKI. *J. Neurosci.* **26**, 11278–86 (2006).
131. Zhao, L., Mandler, M. D., Yi, H. & Feng, Y. Quaking I controls a unique cytoplasmic pathway that regulates alternative splicing of myelin-associated glycoprotein. *Proc. Natl. Acad. Sci. U. S. A.* **107**, 19061–6 (2010).
132. Mandler, M. D., Ku, L. & Feng, Y. A cytoplasmic quaking I isoform regulates the hnRNP F/H-dependent alternative splicing pathway in myelinating glia. *Nucleic Acids Res.* **42**, 7319–29 (2014).
133. Lu, Z. *et al.* The quakingviable mutation affects qkl mRNA expression specifically in myelin-producing cells of the nervous system. *Nucleic Acids Res.* **31**, 4616–4624 (2003).
134. Lang, H. *et al.* Nuclear factor kappaB deficiency is associated with auditory nerve degeneration and increased noise-induced hearing loss. *J. Neurosci.* **26**, 3541–3550 (2006).
135. Huang, D. W., Sherman, B. T. & Lempicki, R. A. Systematic and integrative analysis of large gene lists using DAVID bioinformatics resources. *Nat. Protoc.* **4**, 44–57 (2009).
136. Huang, D. W., Sherman, B. T. & Lempicki, R. A. Bioinformatics enrichment tools: Paths toward the comprehensive functional analysis of large gene lists. *Nucleic Acids Res.* **37**, 1–13 (2009).
137. Supek, F., Bošnjak, M., Škunca, N. & Šmuc, T. REVIGO summarizes and visualizes long lists of gene ontology terms. *PLoS One* **6**, (2011).
138. Zhang, Y. *et al.* An RNA-sequencing transcriptome and splicing database of glia, neurons, and vascular cells of the cerebral cortex. *J. Neurosci.* **34**, 11929–11947 (2014).
139. Thakurela, S. *et al.* The transcriptome of mouse central nervous system myelin. *Sci. Rep.* **6**, 25828 (2016).
140. Galarneau, A. & Richard, S. Target RNA motif and target mRNAs of the Quaking STAR protein. *Nat. Structural Mol. Biol.* **12**, 691–698 (2005).
141. Cooley, M. A. *et al.* Fibulin-1 is required for bone formation and Bmp-2-mediated induction of Osterix. *Bone* **69**, 30–8 (2014).
142. Schindelin, J. *et al.* Fiji: an open-source platform for biological-image analysis. *Nat. Methods* **9**, 676–682 (2012).

143. Hirose, K., Discolo, C. M., Keasler, J. R. & Ransohoff, R. Mononuclear phagocytes migrate into the murine cochlea after acoustic trauma. *J. Comp. Neurol.* **489**, 180–194 (2005).
144. Sautter, N. B., Shick, E. H., Ransohoff, R. M., Charo, I. F. & Hirose, K. CC chemokine receptor 2 is protective against noise-induced hair cell death: Studies in CX3CR1+/GFP mice. *JARO - J. Assoc. Res. Otolaryngol.* **7**, 361–372 (2006).
145. Lang, H. *et al.* Contributions of Mouse and Human Hematopoietic Cells to Remodeling of the Adult Auditory Nerve After Neuron Loss. *Mol. Ther.* **24**, 2000–2011 (2016).
146. Kaur, T. *et al.* Fractalkine Signaling Regulates Macrophage Recruitment into the Cochlea and Promotes the Survival of Spiral Ganglion Neurons after Selective Hair Cell Lesion. *J. Neurosci.* **35**, 15050–15061 (2015).
147. Nakamura, R. *et al.* Availability of a Microglia and Macrophage Marker, Iba-1, for Differential Diagnosis of Spontaneous Malignant Reticuloses from Astrocytomas in Rats. *J. Toxicol. Pathol.* **26**, 55–60 (2013).
148. Darbelli, L. & Richard, S. Emerging functions of the Quaking RNA-binding proteins and link to human diseases. *Wiley Interdiscip. Rev. RNA* **7**, 399–412 (2016).
149. Britsch, S. *et al.* The transcription factor Sox10 is a key regulator of peripheral glial development. *Genes Dev.* **15**, 66–78 (2001).
150. Breuskin, I. *et al.* Glial but not neuronal development in the cochleovestibular ganglion requires Sox10. *J. Neurochem.* **114**, 1827–1839 (2010).
151. Kuhlbrodt, K., Herbarth, B., Sock, E., Hermans-Borgmeyer, I. & Wegner, M. Sox10, a novel transcriptional modulator in glial cells. *J. Neurosci.* **18**, 237–50 (1998).
152. Finzsch, M. *et al.* Sox10 is required for Schwann cell identity and progression beyond the immature Schwann cell stage. *J. Cell Biol.* **189**, 701–712 (2010).
153. Graham, V., Khudyakov, J., Ellis, P. & Pevny, L. SOX2 functions to maintain neural progenitor identity. *Neuron* **39**, 749–765 (2003).
154. Ferri, A. L. M. Sox2 deficiency causes neurodegeneration and impaired neurogenesis in the adult mouse brain. *Development* **131**, 3805–3819 (2004).
155. Le, N. *et al.* Analysis of congenital hypomyelinating Egr2Lo/Lo nerves identifies Sox2 as an inhibitor of Schwann cell differentiation and myelination. *Proc. Natl. Acad. Sci. U. S. A.* **102**, 2596–2601 (2005).
156. Parrinello, S. *et al.* EphB signaling directs peripheral nerve regeneration through Sox2-dependent Schwann cell sorting. *Cell* **143**, 145–55 (2010).
157. Koike, T., Wakabayashi, T., Mori, T., Hirahara, Y. & Yamada, H. Sox2 promotes survival of satellite glial cells in vitro. *Biochem. Biophys. Res. Commun.* **464**, 269–274 (2015).
158. Dillman, R. O. *et al.* Phase II trial of dendritic cells loaded with antigens from self-renewing, proliferating autologous tumor cells as patient-specific antitumor vaccines in patients with metastatic melanoma: final report. *Cancer Biother. Radiopharm.* **24**, 311–9 (2009).
159. Kurioka, T. *et al.* Selective hair cell ablation and noise exposure lead to

- different patterns of changes in the cochlea and the cochlear nucleus. *Neuroscience* **332**, 242–257 (2016).
160. Chen, P., Piao, X. & Bonaldo, P. Role of macrophages in Wallerian degeneration and axonal regeneration after peripheral nerve injury. *Acta Neuropathologica* **130**, 605–618 (2015).
 161. Miron, V. E. & Franklin, R. J. M. Macrophages and CNS remyelination. *Journal of Neurochemistry* **130**, 165–171 (2014).
 162. Ludwin, S. K. Remyelination in the central nervous system and the peripheral nervous system. *Adv. Neurol.* **47**, 215–54 (1988).
 163. Schmiedt, R. Acoustic injury and the physiology of hearing. *J. Acoust. Soc. Am.* **76**, 1293–1317 (1984).
 164. Spoenclin, H. Histopathology of noise deafness. *J. Otolaryngol.* **14**, 282–6 (1985).
 165. Borg, E., Canlon, B. & Engström, B. Noise-induced hearing loss. Literature review and experiments in rabbits. Morphological and electrophysiological features, exposure parameters and temporal factors, variability and interactions. *Scand. Audiol. Suppl.* **40**, 1–147 (1995).
 166. Bohne, B. & Harding, G. Degeneration in the cochlea after noise damage: primary versus secondary events. *Am. J. Otol.* **21**, 505–509 (2000).
 167. Liberman, M. C. Noise-induced hearing loss: Permanent versus temporary threshold shifts and the effects of hair cell versus neuronal degeneration. in *Advances in Experimental Medicine and Biology* **875**, 1–7 (2016).
 168. Liberman, M. C. & Kujawa, S. G. Cochlear synaptopathy in acquired sensorineural hearing loss: Manifestations and mechanisms. *Hearing Research* **349**, 138–147 (2017).
 169. Dutta, R. & Trapp, B. D. Mechanisms of neuronal dysfunction and degeneration in multiple sclerosis. *Progress in Neurobiology* **93**, 1–12 (2011).
 170. Sadanaga, M. & Morimitsu, T. Development of endocochlear potential and its negative component in mouse cochlea. *Hear. Res.* **89**, 155–161 (1995).
 171. Wang, J. *et al.* Myelination of the postnatal mouse cochlear nerve at the peripheral-central nervous system transitional zone. *Front. Pediatr.* **1**, 43 (2013).
 172. Kwon, H. S. *et al.* Myocilin mediates myelination in the peripheral nervous system through ErbB2/3 signaling. *J. Biol. Chem.* **288**, 26357–71 (2013).
 173. Paasche, G. *et al.* Effects of metal ions on fibroblasts and spiral ganglion cells. *J. Neurosci. Res.* **89**, 611–617 (2011).
 174. Fields, R. D. Myelin formation and remodeling. *Cell* **156**, 15–7 (2014).
 175. Chomiak, T. & Hu, B. What Is the Optimal Value of the g-Ratio for Myelinated Fibers in the Rat CNS? A Theoretical Approach. *PLoS One* **4**, e7754 (2009).
 176. Rushton, W. A. H. A theory of the effects of fibre size in medullated nerve. *J. Physiol.* **115**, 101–122 (1951).
 177. Cercignani, M. *et al.* Characterizing axonal myelination within the healthy population: a tract-by-tract mapping of effects of age and gender on the fiber g-ratio. *Neurobiol. Aging* **49**, 109–118 (2017).
 178. Rawji, K. S. & Yong, V. W. The benefits and detriments of

- macrophages/microglia in models of multiple sclerosis. *Clin. Dev. Immunol.* **2013**, 948976 (2013).
179. Wilms, H., Hartmann, D. & Sievers, J. Ramification of microglia, monocytes and macrophages in vitro: influences of various epithelial and mesenchymal cells and their conditioned media. *Cell Tissue Res.* **287**, 447–58 (1997).
 180. Nimmerjahn, A., Kirchhoff, F. & Helmchen, F. Resting microglial cells are highly dynamic surveillants of brain parenchyma in vivo. *Science* **308**, 1314–8 (2005).
 181. McWhorter, F. Y., Wang, T., Nguyen, P., Chung, T. & Liu, W. F. Modulation of macrophage phenotype by cell shape. *Proc. Natl. Acad. Sci. U. S. A.* **110**, 17253–8 (2013).
 182. Spencer, P. S. & Thomas, P. K. Ultrastructural studies of the dying-back process II. The sequestration and removal by Schwann cells and oligodendrocytes of organelles from normal and diseased axons. *J. Neurocytol.* **3**, 763–783 (1974).
 183. Brosius Lutz, A. *et al.* Schwann cells use TAM receptor-mediated phagocytosis in addition to autophagy to clear myelin in a mouse model of nerve injury. *Proc. Natl. Acad. Sci. U. S. A.* **114**, E8072–E8080 (2017).
 184. Taveggia, C. Schwann cells–axon interaction in myelination. *Curr. Opin. Neurobiol.* **39**, 24–29 (2016).
 185. Taveggia, C., Feltri, M. L. & Wrabetz, L. Signals to promote myelin formation and repair. *Nat. Rev. Neurol.* **6**, 276–287 (2010).
 186. Barros, M. H. M., Hauck, F., Dreyer, J. H., Kempkes, B. & Niedobitek, G. Macrophage polarisation: an immunohistochemical approach for identifying M1 and M2 macrophages. *PLoS One* **8**, e80908 (2013).
 187. Hickman, S. E. *et al.* The microglial sensome revealed by direct RNA sequencing. *Nat. Neurosci.* **16**, 1896–905 (2013).
 188. Bennett, M. L. *et al.* New tools for studying microglia in the mouse and human CNS. *Proc. Natl. Acad. Sci.* **113**, E1738–E1746 (2016).
 189. Feinberg, K. *et al.* A glial signal consisting of gliomedin and NrCAM clusters axonal Na⁺ channels during the formation of nodes of Ranvier. *Neuron* **65**, 490–502 (2010).
 190. Gallardo, E., García, A., Combarros, O. & Berciano, J. Charcot-Marie-Tooth disease type 1A duplication: spectrum of clinical and magnetic resonance imaging features in leg and foot muscles Downloaded from. *Brain* **129**, 426–437 (2006).
 191. Darbelli, L., Choquet, K., Richard, S. & Kleinman, C. L. Transcriptome profiling of mouse brains with qkl-deficient oligodendrocytes reveals major alternative splicing defects including self-splicing. *Sci. Rep.* **7**, 7554 (2017).
 192. Conn, S. J. *et al.* The RNA binding protein quaking regulates formation of circRNAs. *Cell* **160**, 1125–1134 (2015).
 193. Chen, A.-J. *et al.* STAR RNA-binding protein Quaking suppresses cancer via stabilization of specific miRNA. *Genes Dev.* **26**, 1459–1472 (2012).
 194. Wang, Y., Vogel, G., Yu, Z. & Richard, S. The QKI-5 and QKI-6 RNA Binding Proteins Regulate the Expression of MicroRNA 7 in Glial Cells. *Mol. Cell. Biol.* **33**, 1233–1243 (2013).

195. Wang, J., Ding, D. & Salvi, R. J. Carboplatin-induced early cochlear lesion in chinchillas. *Hear. Res.* **181**, 65–72 (2003).
196. Lang, H., Schulte, B. A. & Schmiedt, R. A. Ouabain Induces Apoptotic Cell Death in Type I Spiral Ganglion Neurons, but not Type II Neurons. *J. Assoc. Res. Otolaryngol.* **6**, 63–74 (2005).
197. Seyyedi, M. & Nadol, J. B. Intracochlear Inflammatory Response to Cochlear Implant Electrodes in the Human. doi:10.1097/MAO.0000000000000540
198. Ryu, K. A. *et al.* Intracochlear Bleeding Enhances Cochlear Fibrosis and Ossification: An Animal Study. *PLoS One* **10**, e0136617 (2015).